Revision 3

Thermal state of the upper mantle and the origin of the Cambrian-Ordovician ophiolite pulse: constraints from ultramafic dikes of the Hayachine-Miyamori Ophiolite

TAKAFUMI KIMURA[1], KAZUHITO OZAWA[1], TAKESHI KURITANI[2], TSUYOSHI IIZUKA[1], AND MITSUHIRO NAKAGAWA[2]

1: Graduate School of Science, The University of Tokyo, Hongo 7-3-1, Bunkyo-ku, Tokyo 113-0033, Japan

2: Department of Earth and Planetary Sciences, Graduate School of Science, Hokkaido University, N10W8, Kita-ku, Sapporo 060-0810, Japan

Affiliations:

Corresponding author: Takafumi Kimura

e-mail address: kimura.t@eps.s.u-tokyo.ac.jp

phone numbers: +81-3-5841-4021

This is the peer-reviewed, final accepted version for American Mineralogist, published by the Mineralogical Society of America.
The published version is subject to change. Cite as Authors (Year) Title. American Mineralogist, in press.
DOI: https://doi.org/10.2138/am-2020-7160. http://www.minsocam.org/

ABSTRACT

Ophiolite pulses, which are periods of enhanced ophiolite generation and emplacement, are thought to have a relevance to highly active superplumes (superplume model). However, the Cambrian-Ordovician pulse has two critical geological features that cannot be explained by such a superplume model: predominance of subduction-related ophiolites and scarcity of plume-related magma activities. We addressed this issue by estimating mechanism and condition of magma generation, including mantle potential temperature (MPT), from a ~500 Ma subduction-related ophiolite, the Hayachine-Miyamori ophiolite. We developed a novel method to overcome difficulties in global MPT estimation from an arc environment by using porphyritic ultramafic dikes showing flow differentiation, which have records of the chemical composition of the primitive magma, including its water content, because of their high pressure (~0.6 GPa) intrusion and rapid solidification. The solidus conditions for the primary magmas are estimated to be ~1450 ℃, ~5.3 GPa. Geochemical data of the dikes show passive upwelling of a depleted mantle source in the garnet stability field without a strong influence of slab-derived fluids. These results combined with the extensive fluxed melting of the mantle wedge prior to the dike formation indicate sudden changes of the melting environment, its mechanism, and the mantle source from extensive fluxed melting of the mantle wedge to decompressional melting of the sub-slab mantle which has been most plausibly triggered by a slab breakoff. The estimated MPT of the sub-slab mantle is ~1350 °C, which is very close to that of the current upper mantle, and may reflect the global value of the upper mantle at ~500 Ma if small-scale convection maintained the shallow sub-slab mantle at a steady thermal state. We therefore conclude that the Cambrian-Ordovician ophiolite pulse is not attributable to high-temperature of the upper mantle. Frequent occurrence of slab breakoff, which is suggested by our geochemical compilation of Cambrian-Ordovician

ophiolites, and subduction termination, which is probably related to the assembly of the Gondwana supercontinent, may be responsible for the ophiolite pulse.

INTRODUCTION

The Earth has been releasing heat into the space, which drives internal and surface processes, such as magmatism, plate tectonics, and evolution of the surface environment (Davies, 1999). In this regard, the thermal history of the Earth is an essential part of its evolution. The major volume (~80 %) of the Earth is occupied by the mantle, which is transferring heat to the Earth's surface by thermal convection. It is, therefore, important to reveal the thermal state of the mantle and temporal changes in its thermal state in order to better understand the past and future evolution of the Earth.

A quantitative proxy of a thermal state of the mantle is the mantle potential temperature (MPT: McKenzie and Bickle, 1988). It has been estimated from the chemical compositions of magmas erupted on the Earth's surface at various tectonic settings, such as mid-ocean ridges and intraplate settings (Putirka, 2005; Lee at al., 2009; Herzberg et al., 2010) as well as volcanic arcs (Lee at al., 2009; Sakuyama et al., 2009, 2014). However, a secular change of the global thermal state of the mantle has been estimated from MPTs at restricted tectonic settings (non-arc environments, such as spreading centers; Herzberg et al., 2010). This restriction of applicable tectonic environments guarantees that the global thermal state of the Earth is sampled by decompressional melting of either upper mantle that passively upwells along divergent margins, or deep mantle that actively upwells from a deep thermal boundary layer. Arc environments were avoided for this purpose because of: (1) involvement of water input from subducting slab into the

magma generation environment and magma degassing during transportation to the surface and volcanic events which leads to technical difficulties in the estimation of MPTs, and (2) a thermal structure and flow pattern of the mantle wedge strongly affected by subduction of a slab, which could be in various thermal states depending on its age. These difficulties in application of the conventional methods to estimate a secular change of the global MPTs of the mantle from magma-related materials occurring in an arc environment must be overcome since there are several periods in the Earth's history when material records of primitive magmas are dominantly available from arc environments (Dilek and Furnes, 2011)

Ophiolites, which are defined in this paper as suites of temporally and spatially associated ultramafic, mafic, and felsic rocks representing remnants of ancient oceanic crust and upper mantle (Dilek and Furnes, 2011, 2014), were formed and exhumed at least since the Paleoproterozoic to the very recent past (Stern, 2005). Their age distributions show several confined periods with high rates of occurrence, which are called "ophiolite pulses" (Abbate et al., 1985; Ishiwatari, 1994; Yakubchuk et al., 1994). These pulses occur in late Neoproterozoic, Cambrian-Ordovician, and Jurassic-Cretaceous times (Ishiwatari, 1994; Dilek, 2003). They have been explained by connection to episodic activities of superplumes generated at the core-mantle boundary region in 300 million years cycles (Ishiwatari, 1994; Dilek, 2003; Vaughan and Scarrow, 2003). We will refer to this hypothesis for the ophiolite pulse origin as the "superplume model". It does not, however, explain two critical features of the Cambrian-Ordovician ophiolite pulse. First, the Cambrian-Ordovician ophiolite pulse is dominated by subduction-related ophiolites thought to have formed mostly in a back-arc environment, which is in contrast to the minor occurrence of subduction-related ophiolites for the Jurassic-Cretaceous pulse (Dilek and Furnes, 2011; Furnes et al., 2014). This peculiarity of the pulse in ophiolite types requires some

mechanisms to explain the high rate of subduction-related ophiolite formation during the Cambrian-Ordovician time. Second, there is almost no report of large igneous provinces (LIPs), which are believed to be closely related to mantle plume activities, during the Cambrian-Ordovician time. Ernst and Buchan (2003) compiled world LIPs since 4000Ma, which shows that LIP generation was significantly suppressed during the Cambrian-Ordovician compared to that during the Jurassic-Cretaceous. Because there are such fundamental inconsistencies between the essential features of Cambrian-Ordovician geological records and the superplume model, the origin of the Cambrian-Ordovician ophiolite pulse should be reappraised.

In order to construct a model for the Cambrian-Ordovician ophiolite pulse and to seek a general model of ophiolite pulses through the Earth's history by considering the secular change of thermal state of the mantle, it is imperative to carefully evaluate dynamics involved in the formation of each ophiolite by examining the mechanisms of magma generation in the mantle, its MPT, and the controlling tectonics. It is, however, not easy to conduct this task for the Cambrian-Ordovician ophiolite pulse because of the aforementioned difficulties in the estimation of global MPT from arc volcanic rocks. The estimated MPTs may represent the thermal state of either the global upper mantle, deep thermal boundary layers, or even arc mantle wedges. In this study, we extend the current estimation method of global MPTs, whose application has been restricted to non-arc environments, to one applicable to arc environments. The novel approach is to use intrusive rocks, from which a proper melt composition, including its water content, can be estimated.

We have developed a new procedure for the estimation of magma generation conditions and the MPTs by examining ultramafic intrusive rocks in the mantle section of an ~500 Ma arc ophiolite, the Hayachine-Miyamori Ophiolite (Ozawa et al., 2015), northern Japan.

We argue for a slab breakoff tectonic origin on the basis of the obtained magma generation conditions and the geological and petrologic data from the ophiolite. The MPTs are shown to represent the thermal state of the Cambrian-Ordovician upper mantle, which are comparable to the present day MPTs of the upper mantle. The implications of the MPTs and slab-breakoff tectonics for the origin of the Cambrian-Ordovician ophiolite pulse are discussed through compilation of geochemical data from ophiolites of this age.

PREVIOUS STUDIES

The Hayachine−Miyamori Ophiolite, located in the South Kitakami Massif, northeast Japan (Fig. 1a), is composed of two complexes separated by the Hizume-Kesennuma fault. They are the Miyamori complex distributed to the west and the Hayachine complex to the east of the fault (Fig. 1a). The two complexes consist mostly of peridotites, with lesser amounts of hornblende-rich mafic-ultramafic rocks and minor shallow intrusions and volcanic rocks. The ophiolite is divided into the Tectonite Member characterized by penetrative plastic deformation textures, and the Cumulate Member featuring cumulus textures without evidence of solid-state deformation (Fig. 1b). Their boundary is delineated within the Miyamori Complex and is an intrusive contact formed after the cessation of the main deformation of the Tectonite Member (Ozawa, 1983; 1984). The boundary strikes nearly parallel to the elongate distribution and layering of the Cumulate Member, ~N 40° W (Ozawa, 1984) (Fig. 1b). The Tectonite Member is further divided by Cr/(Cr+Al) ratio (Cr#) of spinel into the Chromite-bearing Ultramafic Suite (CRUS; Cr# > 0.4) and the Aluminous Spinel Ultramafic Suite (ASUS; Cr# < 0.4). The Hayachine complex is mostly composed of the ASUS. The Miyamori complex is mostly

132 composed of the CRUS, and the rocks of ASUS occur as patches in the CRUS with sizes of
133 several hundred meters to a kilometer (Ozawa, 1987b; Ozawa, 1988; Ozawa et al., 2015).

134 Ozawa (1984) showed that the Miyamori complex is a thrust sheet tectonically
135 transported from the northwest to the current site over Paleozoic sedimentary rocks and
136 metamorphic rocks distributed to the southwest of the Miyamori complex. The metamorphic
137 rocks also occur in a tectonic window (1 km x 600 m) in the central part of the Miyamori
138 complex, where pelitic schist, greenschist, epidote amphibolite, and amphibolite are distributed
139 from the west to the east in this order. These rocks could have been a metamorphic sole of the
140 ophiolite as reported from beneath many ophiolites (Williams and Smyth, 1973; Jamieson, 1986)
141 because of the short-distance transition of their metamorphic grade from the greenschist to
142 amphibolite facies over the spatial scale of a few hundred meters. Their relationship with the
143 ophiolite is, however, unclear due to the later tectonic disturbance.

144 The Hayachine-Miyamori Ophiolite is one of the ophiolites belonging to the Cambrian-
145 Ordovician ophiolite pulse. The exhumation and cooling of the ophiolite took place at ca. 450 Ma
146 estimated by K-Ar ages of hornblende in hornblende-bearing mafic intrusive rocks (Ozawa et al.,
147 1988; Shibata and Ozawa, 1992), and the magmatic events took place at 499 ± 65 Ma estimated
148 by Sm-Nd isochron ages of clinopyroxene separated from lherzolite of the ASUS from the
149 Hayachine complex (Yoshikawa and Ozawa, 2007; Ozawa et al., 2015). The Hizume-Kesennuma
150 fault was active at least since the Jurassic time (Ehiro and Suzuki, 2003). The ophiolite is
151 characterized by several features suggesting its formation in an arc environment, such as the
152 presence of abundant amphibole and minor phlogopite in the mantle section with arc
153 geochemical signatures, and is classified into the supra-subduction type according to Dilek and
154 Furnes (2014). The geology, petrology, and geochemistry of the ophiolite have been extensively

studied, and its tectonic history is well constrained in spite of intensive late-stage secondary processes, such as serpentinization, contact metamorphism by granite intrusions, and alteration since the Cambrian-Ordovician time (Ozawa, 1987a, 1988; Ozawa and Shimizu, 1995; Yoshikawa and Ozawa, 2007; Ozawa et al., 2015). The depth of formation of a magma body crystallizing the Cumulate Member in the already deformed Tectonite Member is estimated to be 18 ± 3 km (approx. 0.6 ± 0.1 GPa) according to the crystallization of plagioclase in equilibrium with olivine in the Cumulate Member at a high magmatic temperature and breakdown of plagioclase into orthopyroxene and spinel-pargasite symplectite along with the contact with olivine at a low temperature (< ~800 °C; Ozawa, 1986). The pressure is too high for the depth of ultramafic cumulate sequences commonly reported from ophiolites, and suggests a thickened crust, though the crustal sections are mostly missing in the Hayachine-Miyamori ophiolites owing to tectonic processes during or after the emplacement. According to the geochemical features, such as TiO_2/K_2O in amphibole in ultramafic rocks, and Rb-Sr and Sm-Nd isotope systems for clinopyroxene in mafic and ultramafic rocks, it is inferred that the ASUS of the Hayachine complex was formed by decompressional melting of a depleted mantle in a back-arc basin environment, the CRUS by flux melting of the ASUS under strong influx of fluids from the subducting slab, and the Cumulate Member by decompressional melting of a depleted mantle (Ozawa, 1988; Ozawa and Shimizu, 1995; Yoshikawa and Ozawa, 2007).

From these extensive data and geological relationships with the surrounding Silurian-Devonian geological units, such as the Motai metamorphic rocks and the Hikami granitic rocks, Ozawa et al. (2015) proposed a tectonic model for the Hayachine-Miyamori Ophiolite. The model consists of a series of events (1)-(4); (1) formation of the ASUS of the Hayachine complex by back-arc spreading in the Cambrian-Ordovician time (~500 Ma), (2) formation of the CRUS

of the Miyamori complex by extensive flux melting accompanying slab rollback, (3) formation of the Cumulate Member by decompressional melting of the mantle triggered by slab breakoff, and (4) exhumation of the ophiolite at ~450 Ma.

GEOLOGY OF ULTRAMAFIC INTRUSIVE ROCKS

The ultramafic intrusive rocks, which have a picritic composition, occur in the Cumulate Member and never crosscut younger intrusive rocks such as the hornblende-rich mafic-ultramafic rocks and the andesite-rhyolite porphyries in the Miyamori complex (Fig. 1b). The ultramafic intrusive rocks are planar in morphology, sharply defined with a thickness of 0.5 to 30 cm, and strike from N47°W to N10°E, which is mostly oblique to the layered structure of the Cumulate Member. They crosscut the layering and weak foliation of the host rock and have many branches (Figs. 2a and 2c). They are coarse-grained and porphyritic (Figs. 2b and 3a) and do not have chilled margins in terms of grain size. Phenocrysts, mostly olivine with a minor amount of clinopyroxene, are either heterogeneously or homogeneously distributed in the dikes. In the former case, phenocrysts are symmetrically concentrated in the center, and their abundance gradually decreases towards the margin (Table 1, Figs. 2a, 2b, and 2c). The phenocrysts show shape-preferred orientation exclusively in the marginal zone with elongate axes lying nearly parallel to the dike wall (Fig. 2c). In the latter case, the homogeneously distributed phenocrysts show less distinct shape-preferred orientation in the dikes.

These facts clearly show that the magmas intruded into the solid host rocks of the Cumulate Member have solidified as dikes or veins. The Cumulate Member is the latest main lithology in the evolution of the Hayachine-Miyamori ophiolite before the formation of

hornblende-bearing mafic-ultramafic intrusive rocks (Ozawa et al., 2015). The formation of the ultramafic intrusive rocks, "ultramafic dikes" hereafter, is one of the latest events in the ophiolite evolution. We found five outcrops of this type of intrusive rocks (Fig. 1b) and collected samples from four thick dikes at four outcrops, two of which are covered with river gravels of a recent flooding and only rootless blocks are available.

PETROGRAPHY

The absence of chilled margins near the contact with their hosts suggests that the intrusion took place at a fairly high temperature and possibly at high pressure, which must be clarified. Moreover, the dikes contain secondary minerals locally forming veins, which sharply cut the primary igneous textures. This indicates that the dikes may have undergone secondary processes such as metamorphism and/or alteration, which could have modified the igneous chemical and textural features. In this section, we describe petrographic features related to igneous processes first to clarify the intrusion environment, and then describe secondary features in order to evaluate the effect of secondary processes.

Igneous textures

Phenocrysts in the dikes are composed mainly of euhedral - subhedral olivine with a subordinate amount of euhedral clinopyroxene, which is absent in some dikes (Table 1). The size of phenocrysts is up to a few millimeters (Figs. 2b and 3a). Olivine is partially preserved everywhere in the dikes which show a homogeneous phenocryst distribution, though the extent of replacement with serpentine is variable (Table 1). Olivine is preserved at the margin and in the center but not at the edge of the dikes which show a central phenocryst concentration (Table 1).

There is a tendency that the matrix-dominant lithology is more susceptible to secondary processes and form hydrous phases such as serpentine and chlorite. The olivine phenocrysts locally include chrome spinel and are partially rimmed by orthopyroxene (Figs. 3a and 3b).

The matrix filling interstitial part of phenocrysts consists of anhedral amphibole and clinopyroxene with minor chrome spinel and dusty fine-grained aggregate after plagioclase (Table 1). Amphibole is the most dominant matrix phase (Table 1; Figs. 3a, 3b, 230 and 3c) and its size ranges from several tens of microns to 1 mm. It forms a polycrystalline aggregate of a few millimeters across and is in direct contact with olivine phenocrysts partially intervening thin orthopyroxene rim. The amphibole locally includes euhedral chrome spinel. The clinopyroxene forms equigranular aggregates, which show a patchy distribution in amphibole or plagioclase pseudomorph. The grain size of clinopyroxene is from several tens to hundreds of microns and tends to be smaller than that of amphibole.

All plagioclase crystals are replaced by aggregates of secondary minerals, but the aggregates can be identified as plagioclase pseudomorphs as explained below. The plagioclase pseudomorphs, up to a few millimeters across, are present only in the center of dikes (Table 1). The pseudomorphs show an anhedral outline, occur in the middle of polycrystalline amphibole, and are locally in contact with clinopyroxene, but are never in direct contact with olivine (Figs. 3a, 3b, and 3c). Such features of plagioclase occurrence are the same as those observed in plagioclase-bearing peridotites of the Cumulate Member (Ozawa, 1986). Spinel shows two different modes of occurrence, which is intimately related to the color difference under an optical microscope which reflects chemical compositions. Brownish chromite spinel is euhedral to subhedral with grain sizes up to 1 mm. It is either included in olivine or occurs in amphibole aggregates. Greenish aluminous spinel showing anhedral and locally vermicular morphology

245 occurs in amphibole surrounding plagioclase (Fig. S1). The texture is essentially the same as that
246 of a reaction zone consisting of an inner zone of aluminous spinel-pargasite symplectite and an
247 outer zone of orthopyroxene around plagioclase in plagioclase-bearing wehrlite of the Cumulate
248 member (Ozawa, 1986). The texture suggests a reaction between olivine phenocrysts and
249 fractionated interstitial melt after or during the crystallization of plagioclase from the interstitial
250 melt, which may have taken place in the last stage of solidification of the dikes at the same
251 pressure estimated for the Cumulate Member formation, ~0.6 ± 0.1 GPa (Ozawa et al., 2015).

252 Orthopyroxene exclusively occurs rimming olivine phenocrysts with thickness of a few
253 hundred μm (Figs. 3a and 3b) and is less abundant near the edge of dikes than in the dike center
254 (Table 1). The dikes have a selvage of orthopyroxene aggregates with a thickness of ~ 0.1 mm
255 along the contact with the host peridotite. The same relationship between pyroxenite dikes and
256 harzburgite host was reported from the Tectonite Member by Ozawa (1994), who attributed the
257 texture to a reaction of hydrous melt transported through fractures with the wall rock under heat
258 loss. The same textural relationship between the olivine phenocrysts with orthopyroxene rim
259 suggests a reaction between the olivine crystals and a magma flowing through fractures before its
260 complete solidification filling the fractures as dikes. The systematic spatial variation of the
261 thickness of orthopyroxene rim on olivine phenocrysts suggests a more extensive reaction in the
262 dike center than in the margin. There are no vesicles or miarolitic cavities, suggesting that no
263 vesiculation occurs during the solidification of the dikes (Figs. 2a, 2b, and 3a).

264

265 **Textures related to secondary low-temperature processes**

Igneous textures were modified in various degrees by low-temperature processes, which are defined in this paper as low-temperature (< ~700 °C) metamorphism and/or alteration with introduction of fluids to form hydrous phases such as serpentine, chlorite, and tremolite associated with crystallization of magnetite and spindle-shaped diopside. We hereafter use "alteration" to denote this process. The orthopyroxene is partially (or totally) replaced by fine-grained aggregates of tremolite and diopside while keeping the primary grain outline (orthopyroxene pseudomorph; Fig. 3a) in samples taken from outcrop (DKSH1 and DKSH2). Some rootless rocks from the dikes (RYO1 and RYO2), however, have fresh orthopyroxene (Figs. 3b and 3c). The aggregates are partly replaced by chlorite. Amphibole is less susceptible to the alteration, but is replaced by tremolite, diopside, chlorite, and serpentine particularly at the dike margin. Plagioclase pseudomorph consists of fine-grained grossular, but the original outline of plagioclase is preserved. In spite of the complete replacement, the origin of the grossular aggregate as plagioclase is supported by its trace element patterns, which are shown below. Olivine phenocrysts are replaced partially or completely by serpentine and magnetite. Such replacement is limited in fresh samples to the formation of serpentine and magnetite along minor fractures in olivine (Figs. 3a and 3b). These textures suggest multistage open-system alteration reactions after the complete solidification of the dike.

The extent of the replacement of each primary mineral by secondary phases was qualitatively evaluated under an optical microscope, and three levels of alteration were distinguished: weak, intermediate, and extensive (Table1). This information was used to classify alteration degrees of the samples into weak, intermediate, and strong (Table 1). The one sample with strong alteration is from the edge of dike DKSH1. Weakly altered samples are from the marginal and central parts of dike DKSH2, which was used to examine alteration processes in

289 detail. A more quantitative parameter for alteration is the mass loss on ignition, which is
290 described below.

291

292 **ANALYTICAL METHODS**

293 Several slabs were obtained sequentially from the center to edge of two dikes DKSH2,
294 which has a homogeneous phenocryst distribution, and DKSH1, which shows a high
295 concentration of phenocrysts in the center (Table 1; Figs. 2a and 2b). Two samples of rootless
296 blocks from locality #3 (RYO1) with a homogeneous phenocryst distribution and locality #4
297 (RYO2) with a zoned phenocryst distribution at sample scale (~15 cm) were also examined
298 (Table 1). Each slab sample (100 - 150 g) was rinsed for 15 minutes in deionized water and
299 methanol using an ultrasonic vibrator and was dried in an oven at 80 ℃ for 12 hours. The dried
300 slab samples were crushed to chips of ~5 mm diameter by a tungsten mortar. The chips were
301 crushed to powder by the rod mill: Retsch Vibratory Disc Mill RS 200 with an agate rod for
302 several minutes. The powder samples of 1.5 - 2.0 g were put in the oven and heated at 120 ℃
303 for 12 hours to outgas the absorbed water. Following this procedure, the powder samples were
304 ignited in a programable multistage heater in a Muffle Furnace of Yamato FO510 to outgas the
305 water and other volatile components in the crystal structures at several temperatures and for the
306 respective durations: 100 ℃ for 10 minutes, 500 ℃ for 30 minutes, 800 ℃ for 30 minutes, and
307 1000 ℃ for 6 hours. The mass loss including water in samples is regarded as a loss on ignition
308 (LOI in wt%). Thin section observation of the examined samples shows that only a minor
309 amount of carbonates and sulfides are present (< ~2 vol% in total). Therefore, the contribution
310 of these minerals to the LOI is negligible.

311 Major and trace element concentrations of the whole-rock samples were measured with an
312 X-ray Fluorescence Spectrometer (XRF): PANalytical Axio at the Department of Earth and
313 Planetary Science, the University of Tokyo by the glass bead method for major elements and the
314 pressed powder method for trace elements. The analytical procedures have been described by
315 Yoshida and Takahashi (1997). The glass beads were prepared as follows. The powder samples
316 and the flux of anhydrous lithium tetraborate were weighed 0.4 g (< 0.1% in error) and 4 g (<
317 0.1% in error), respectively and were mixed. The mixed powder and a drop of lithium iodide
318 were put in a platinum crucible and heated with a fuse sampler, Tokyo Kagaku TK−4100, to
319 obtain glass bead.

320 Major element concentrations in minerals were measured with an electron probe
321 microanalyzer (EPMA; JEOL JXA−8900L), at the Department of Earth and Planetary Science,
322 the University of Tokyo. The adopted analytical conditions for olivine, pyroxene, amphibole, and
323 spinel are: a focused beam, an acceleration voltage of 15 kV, a beam current of 12 nA on a
324 Faraday cup, and 30 s counting time for peak and 15 s for background on both sides of each peak.
325 The beam diameter of 50 μm is adopted for analyses of the core of plagioclase pseudomorph
326 replaced by fine-grained mineral aggregates to obtain the bulk composition. We adopted an
327 acceleration voltage of 25 kV and a beam current of 50 nA on a Faraday cup and 100 s counting
328 time for peak and 50 s for background on both sides of each peak for trace elements in olivine
329 (NiO and MnO). The correction method to obtain wt% from peak intensity after correcting
330 background is ZAF.

331 Trace elements in the whole-rock samples were measured on the glass beads prepared for
332 the XRF analyses with a Thermo Fisher Scientific iCAP Q inductively coupled plasma mass
333 spectrometer (ICP-MS) coupled with a CETAC LSX-213 G2+ Nd:YAG laser ablation (LA)

system at the Department of Earth and Planetary Science, the University of Tokyo. The analytical procedures described by Itano and Iizuka (2017) were adopted. The glass beads were cut vertically to the disks and the cut surface was polished with diamond paste (1μm size). The laser beam with a spot size of 50 μm, a shot frequency of 10 Hz, and a scan rate of 5 μm/s in line analysis were used. Analyzed elements are Ca, Cr, Mn, Ni, Sr, Y, Zr, Nb, Ba, La, Ce, Pr, Nd, Sm, Eu, Gd, Tb, Dy, Ho, Er, Tm, Yb, Lu, Hf, Ta, Pb, and U. The obtained signal intensities of trace element data were corrected for gas blank, and calibrated against NIST SRM 613 (Hollocher and Ruiz, 1995). Trace element concentrations on each sample were normalized using the Ca concentrations of the glass beads measured with XRF as an internal standard.

Trace element concentrations of amphibole and clinopyroxene in thin sections samples polished with diamond paste (1 μm size) were measured with the LA-ICP-MS. Focused-laser with a spot size of 40 μm and a shot frequency of 5 Hz were used. The integration time is 60 seconds, including 20 seconds gas blank measurement. Analyzed elements are Ca, Sr, Y, Zr, Nb, Ba, La, Ce, Pr, Nd, Sm, Eu, Gd, Tb, Dy, Ho, Er, Tm, Yb, Lu, Hf, Ta, Pb, and U. The correction procedures of obtained signal intensities are basically the same as those adopted for the whole-rock analyses described above. The Ca concentration measured by EPMA on each analysis spot was used as an internal standard.

Nd and Sr isotope ratios in the whole-rock samples and clinopyroxenes were measured with a Thermo Fisher Scientific Neptune plus multiple collector ICP−MS at the Graduate School of Science, Hokkaido University. Clinopyroxene grains were carefully handpicked from coarsely crushed samples of the ultramafic dikes under a binocular microscope. They were powdered by an agate mortar. The analytical procedures for chemical separation followed the methods used in Pin et al. (1994) and Noguchi et al. (2011) for Sr, Pin et al. (1994) and Pin and Zalduegui (1997)

for Nd. Mass fractionation factors for Sr and Nd were calculated using $^{86}Sr/^{88}Sr = 0.1194$ and $^{146}Nd/^{144}Nd = 0.7219$, respectively. Additional corrections were performed by applying a standard bracketing method using NIST987 and JNdi-1 for Sr and Nd isotopic analyses, respectively. The data were finally normalized to $^{87}Sr/^{86}Sr = 0.710214$ for NIST 987, and $^{143}Nd/^{144}Nd = 0.512117$ for JNdi-1. The isotopic ratios of the GSJ standard JB-3, measured during the course of this study, were $^{87}Sr/^{86}Sr = 0.703384 \pm 0.000024$ (n = 32, 2σ), $^{143}Nd/^{144}Nd = 0.513065 \pm 0.000011$ (n = 23, 2σ). The Rb/Sr and Sm/Nd ratios of whole-rock samples were measured by ICP-MS using a Thermo Fisher X-series at the Graduate School of Science, Hokkaido University. The analytical uncertainties are typically 0.7 % for the Rb/Sr ratios and 0.5 % for the Sm/Nd ratios.

WHOLE-ROCK CHEMISTRY

Major elements

The whole-rock major element oxide contents including the loss on ignition (LOI) of dike samples are listed in Table 1. The MgO contents of the slab samples vary from 19.4 to 32.4 wt%, Al_2O_3 from 4.2 to 8.4 wt%, Fe_2O_3* (total Fe as Fe_2O_3) 9.3 to 13.8 wt% and the LOI from 2.7 to 6.4 wt%. (Table 1, Fig. 4). The weakly altered samples from dike DKSH2 show lower values of LOI than the extensively altered samples, though they have the same igneous modal compositions (Table 1).

Rare earth and other trace elements

The whole-rock rare earth element (REE) and other trace element of dike samples are listed in Table 1. The CI-chondrite normalized trace element and REE patterns of the samples are plotted in Figs. 5a, 5b, 5c, and 5d. The dikes have essentially the same trace element patterns, which are characterized by strong positive anomalies of Ba and Sr, a strong negative anomaly of Pb, and weak negative anomalies of Hf and Zr relative to the REEs, and U, Nb, Ta lying on a smooth extension of the REE variations (Fig. 5a). The REE patterns are essentially the same for all samples and are characterized by smooth overall variations: a depletion of light rare earth elements (LREE), and a weak depletion of heavy rare earth elements (HREE) (Figs. 5c and 5d). The abundances of REE in the dikes having homogeneous phenocryst distributions are nearly constant (Fig. 5c), but those of the dikes having a central enrichment of phenocrysts are high in the edge and margin and low in the center while keeping the same variation pattern (Fig. 5d).

Isotope ratios

The whole-rock $^{87}Sr/^{86}Sr$ and $^{143}Nd/^{144}Nd$ ratios of samples from four dikes are listed in Table 2 and are plotted in Fig. 6a. The $^{143}Nd/^{144}Nd$ ratios are similar irrespective of localities and positions within each dike and range from 0.512975 to 0.513079. There is a systematic difference of Sr isotopes depending on the degree of alteration in samples from dike DKSH2, as shown in Fig. 6a. The strongly and intermediately altered samples with high LOI have higher ^{87}Sr / ^{86}Sr ratios than the less altered samples with low LOI. The lines that join samples with different degrees of alteration in the $^{87}Sr/^{86}Sr$ and $^{143}Nd/^{144}Nd$ diagram (Fig. 6a) are nearly horizontal, which indicates that secondary processes shifted $^{87}Sr/^{86}Sr$ to higher values but did not affect the Nd isotope ratios. The least altered samples of the dikes with homogeneous phenocryst distribution (DKSH2MW and DKSH2CW) have low ^{87}Sr / ^{86}Sr ratios, which are thought to

represent the primary values before the alteration. The range of the initial εNd of four dikes and the values of the initial $^{87}Sr/^{86}Sr$ of DKSH2MW and DKSH2CW are 6.0 - 7.1 and ~0.7032, respectively and plot just at the lower end of the Cambrian-Ordovician MORB field (Yoshikawa and Nakamura, 2000; εNd, 7 - 12; ^{87}Sr / ^{86}Sr, 0.7018 - 0.7027).

MINERAL CHEMISTRY

Cation ratios of minerals are abbreviated as follows: Mg# = Mg/(Mg + Fe^{2+}), Cr# = Cr/(Cr + Al). The total iron is assumed to be Fe^{2+}, except for spinel and amphibole, for which ferric iron contents were calculated from stoichiometry constraints with charge balance considerations. The procedure for amphibole is from Leake et al. (1997).

Major and trace element compositions of minerals

Olivine. Olivine in the dikes and their host peridotites is homogeneous in Mg# on a grain scale (a few millimeters). A variation in Mg# on the scale of 10 cm is, however, observed not only in the dikes but also in the host peridotites. This is well documented in dikes with a homogeneous phenocryst distribution as shown in Fig. 7 for dike DKSH2 because of the limited alteration near the contact. The Mg# decreases from 0.90 to 0.87 over the distance of 54 mm from the dunite host to the contact and from 0.87 to 0.83 over the distance of 60 mm from the contact to the dike center (Fig. 7a). Olivines in the dikes are heterogeneous in NiO content on a grain scale, which is manifested by the larger scatter in composition at a given distance than that of Mg# in Fig. 7a. It shows variation across the contact with the host dunite as in the case of Mg# (Fig. 7b), but the spatial extent of variation is narrower than that of Mg# (cf. Figs. 7a and 7b).

The average NiO content in olivine at the center of the dike is 0.21 wt% with a standard deviation of 0.01 wt% in 1σ. It is 0.35 wt% with a standard deviation of 0.01 wt% in 1σ in the host dunite.

Spinel. Spinel is present in all samples and shows diverse chemical composition, particularly in terms of tetravalent cations (Table 1; Fig. 8). It shows zoning in each grain. Euhedral spinel grains show concentric zoning with decreases in Cr# and $Fe^{3+}/(Cr+Al+Fe^{3+})$ from the core to the rim (see Figs. S2a and S2b). The Cr# and $Fe^{3+}/(Cr+Al+Fe^{3+})$ vary from 0.37 and 0.14 at the grain center to 0.13 and 0.05 at the rim, respectively. The largest euhedral spinel grain registers the highest Cr# and $Fe^{3+}/(Cr+Al+Fe^{3+})$ at the core. Subhedral and anhedral spinel grains occurring in adjacent to plagioclase pseudomorphs are rich in Al and poor in Cr and Fe^{3+}. Their Cr# range 0.00 - 0.03 and $Fe^{3+}/(Cr+Al+Fe^{3+})$ 0.01 - 0.02. The Cr# in large grains of such spinel shows an asymmetric zoning pattern, which increases from the rim closer to plagioclase to the opposite rim (see Figs. S2c and S2d). Small green spinel, locally vermicular in morphology, is particularly aluminous, and it is almost Cr-free in an extreme case (Figs. 8 and S1).

Amphibole. Amphibole is present in all the dikes but is completely replaced by secondary minerals near the contact with the host peridotites (Table 1). All the amphiboles are classified as pargasite according to Leake et al. (1997) (see Fig. S3). Amphibole in the dike center is homogeneous in Mg# on a grain scale (~1 mm). The Mg# of amphibole varies from 0.82 to 0.92 depending on the local modal abundance of olivine phenocrysts: the Mg# tends to be higher near olivine phenocrysts. A variation of Mg# across the contact with the host peridotite cannot be clarified because of the complete alteration of amphibole near the contact (Fig. 7a). The TiO_2 / K_2O weight ratios of amphibole, shown in Fig. 9, are within the range for normal mid-ocean ridge basalts (NMORB) and are similar to the values of ASUS of the Hayachine complex (Ozawa, 1988) and the Cumulate Member of the Miyamori complex (Ozawa et al., 2015). The

ratio is clearly distinct from those of CRUS in the Miyamori complex, which is comparable to the ratio of high magnesian andesite (Ozawa, 1988).

Chondrite-normalized trace element patterns of 7 amphibole grains in weakly altered samples of dike DKSH2 are plotted in Fig. 10a. The patterns have peculiar features of a substantial decline from middle rare earth elements (MREEs) to light rare earth elements (LREEs), a slight decline from MREEs to heavy rare earth elements (HREEs), positive anomalies of some of highly incompatible elements (Ba and Sr), a strong negative anomaly of Pb and weak negative anomalies of Hf and Zr relative to rare earth elements (REEs).

Orthopyroxene. Orthopyroxene survived alteration in the least altered dikes (Table1; RYO1 and RYO2) is homogeneous on a few hundred-micrometer scale and has Mg#, Cr#, Al_2O_3 and CaO wt% ranging from 0.82 to 0.84, 0.01 to 0.03, 2.1 to 3.1 wt%, 0.47 to 0.67 wt%, respectively. The spatial chemical variations of orthopyroxene on the scale of ~10cm in the dikes and their host peridotite cannot be clarified because of the extensive alteration.

Clinopyroxene. Clinopyroxene phenocrysts, that occur in some of the dikes (Table1; DKSH1, RYO1, and RYO2), have chemical zoning in terms of Mg#, Cr#, Al_2O_3, and CaO. The core tends to have higher Mg#, Cr#, and lower Al_2O_3, CaO wt% than the rim. The Mg#, Cr#, Al_2O_3, and CaO wt% vary from 0.86 to 0.88, 0.03 to 0.10, 2.9 to 5.1 wt%, 21.4 to 23.5 wt%, respectively. The $^{87}Sr/^{86}Sr$ and $^{143}Nd/^{144}Nd$ ratios of separated clinopyroxene from dike RYO1 are 0.513055 and 0.703701, respectively, which are similar to those of the whole rock (Fig. 6a).

The Mg#, Cr#, Al_2O_3 and CaO wt% of matrix clinopyroxenes show variations on a few hundred micrometers scale, ranging from 0.83 to 0.89, 0.03 to 0.08, 2.7 to 4.9 wt%, 21.1 to 23.5 wt%, respectively. The Mg# shows a wide variation from the dike center to the host dunite (Fig.

7a), though the variation is not so distinct as exhibited by olivine. This is partly due to the variability of the Mg# depending on the local modal abundance of olivine phenocrysts. Spindle-shaped clinopyroxene, which is inferred to have crystallized during alteration according to its occurrence and morphology, has the highest CaO (~24.4 wt%) and lowest Al_2O_3 (~0.4 wt%) contents and classified as diopside.

Chondrite-normalized trace element patterns of matrix clinopyroxene from weakly altered dike DKSH2 are plotted in Fig. 10a. All of 5 analyses are essentially the same except for Ba, which shows a large variation. The trace element patterns are characterized by a depletion of Ta, strong negative anomalies of Pb and Nb. The REE abundance of matrix clinopyroxene is lower than that of the matrix amphibole. Their patterns are distinct in that clinopyroxene has a more sloped CI-chondrite normalized variations of LREEs and HREEs than amphibole.

Plagioclase (pseudomorph). Trace element patterns of fine-grained aggregate which consist mostly of grossular in a weakly altered sample DKSH2CW are characterized by distinct Eu positive anomaly and depletion of HREEs, which are typical for plagioclase (Fig. 10b). This clearly supports that the aggregate is an alteration product of plagioclase (pseudomorph).

MAGMA GENERATION CONDITION AND MECHANISM

In this section, after showing that melt compositions are restorable from the dikes, we will take the following steps to estimate magma generation conditions, melting mechanisms, and mantle potential temperatures on the basis of the data presented above. (1) We first restore the original whole-rock compositions for major and trace elements by correcting for alteration modification. (2) We estimate the intruded melt compositions by correcting for subsolidus

489 modifications and olivine accumulation. (3) We estimate primary melt compositions in
490 equilibrium with the mantle by adding olivine to the intruded melts. (4) We use the primary melt
491 compositions to estimate melting mechanism, mantle source composition, melting/melt
492 segregation conditions, and solidus conditions. (5) We finally estimate mantle potential
493 temperatures. (6) Additionally, we evaluate the openness of the melting system.

494

495 **Melt compositions preserved in the dikes**

496 The examined dikes are similar in their field occurrences, petrography, whole-rock
497 chemical compositions, mineral chemical compositions, and isotopic compositions, as described
498 above, irrespective of the phenocryst distribution in each dike. This indicates that they formed in
499 a series of intrusion events from a common magma and that the phenocryst distribution was
500 controlled by intrusion and solidification processes. The high concentration of phenocrysts in the
501 dike center and shape-preferred orientation of the olivine phenocrysts in the marginal zone
502 indicate the operation of flow differentiation owing to a velocity gradient in flowing dikes, which
503 is known as "Bagnold effect" (Bagnold, 1954; Komar, 1972). The homogeneous distribution and
504 less distinct shape-preferred orientation of phenocrysts in some dikes can be explained by a
505 turbulent flow associated with a high Reynolds number. The distributions of phenocrysts in the
506 dikes suggest that the magmas were injected as crystal-laden magmas which solidified in a closed
507 system on a short time scale to maintain the distribution of phenocrysts under the gravitational
508 field irrespective of the zoned or homogeneous distribution.

509 Examination of the variation of Mg# of olivine across the contacts between the host
510 peridotite and the dike (Fig. 7a) also supports such rapid solidification. The area ratio of the Mg-

Fe profile of olivine in the dike and the host sides (Fig. 7a) is 0.69 : 0.31, which is clearly different from 1:1. The host peridotite is mainly composed of olivine (~99 wt%), whereas the dike side is composed of olivine phenocrysts (~37.0 wt%) and matrix minerals (amphibole, ~58.3 wt%; orthopyroxene, ~3.9 wt%; and clinopyroxene, ~0.1 wt%; Table 3) which are calculated from the igneous modal composition of the DKSH2EI in vol% (Table 1). Taking the igneous modal abundance of the dike side into consideration, it is shown that the mass balance of MgO is maintained in a closed system, within a uncertainty smaller than ~15% (Table 3). Therefore, the Mg-Fe profile in the homogeneous-type dike is due to subsolidus diffusional Mg-Fe exchange after the solidification of the magma on a time scale much longer than Fe-Mg exchange involving magma over 10 cm. The Mg# profile across the contact is asymmetric and characterized by a shorter tail on the host dunite side and a longer tale within the dike (Fig. 7a). This feature is attributable to Mg-Fe interdiffusion with composition dependence and the difference in igneous modal abundance. This is consistent with the much narrower variation of NiO content in olivine than that of Mg# because the Ni diffusion is slower than the Fe-Mg interdiffusion (Fig. 7b; Petry et al., 2004; Dohmen and Chakraborty, 2007). It is highly plausible that the melt composition in the dikes is preserved with limited interaction with the wall rocks by rapid solidification after the magma intrusion.

Restoration of original whole-rock compositions for major elements

Subsolidus modifications due to alteration. The presence of secondary hydrous minerals, such as serpentine, diopside, and chlorite, as described in the petrography section, indicates that the dikes suffered from alteration. In order to clarify if the formation of secondary hydrous phases modified the whole-rock compositions, we compared two pairs of samples from

534 dike DKSH2, which show a different degree of alteration (Table 1) while keeping the same
535 igneous modal abundances (Table 1). Loss on ignition (LOI) was used as a quantitative measure
536 of the degree of alteration, and the effects of alteration were examined by plotting oxide wt%
537 data against the LOI (Fig. 11). A vector defined by a pair of samples with a difference in LOI and
538 oxide contents is regarded as a trend of alteration. The obtained mean alteration vectors from the
539 two sample pairs are listed in Table S1. The initial whole-rock water contents for each sample
540 can be estimated from the water content of pargasite (~2.5 wt%) and its modal abundances
541 (Tables 1 and 4). We obtained whole-rock compositions prior to alteration for nine samples by
542 extrapolating the whole-rock data to the initial whole-rock water contents. The corrected
543 compositions are listed in Table 4.

544 **Subsolidus high-temperature modifications due to elemental exchange with the host.**
545 The variation of the Mg# of olivine observed near the contact of dike DKSH2 and the host (Fig.
546 7) shows that the whole-rock MgO and FeO concentrations in the dike were modified by
547 subsolidus diffusion at high temperatures as discussed above. Figure 7 shows that the
548 modification is limited to within 4 cm from the contact with the host. Most of the samples
549 including the rootless blocks with more than 10 cm size were, therefore, not affected by the
550 diffusional exchange. However, the whole-rock chemical compositions of the samples near the
551 contact (DKSH1ES and DKSH2EI; Table 1) were shifted from the values that these rocks had
552 soon after the dike solidification. The whole-rock composition of sample DKSH2EI before the
553 subsolidus high-temperature modification was restored by using the initial olivine Mg# in the
554 center (~0.83, Fig. 7a), which was not modified by this modification, and the igneous modal
555 abundance (Table 4). The same procedure cannot be applied to DKSH1ES because of its
556 extensive alteration. The restored composition for DKSH2EI is lower in MgO and higher in FeO

This is the peer-reviewed, final accepted version for American Mineralogist, published by the Mineralogical Society of America.
The published version is subject to change. Cite as Authors (Year) Title. American Mineralogist, in press.
DOI: https://doi.org/10.2138/am-2020-7160. http://www.minsocam.org/

(Table 4). The whole-rock major element compositions corrected for the alteration and diffusional elemental exchange with the host are plotted in Fig. 12 excepting sample DKSH1ES.

Estimation of intruded melt compositions for major elements and igneous olivine compositions.

The liquid composition of magmas intruded into fractures and frozen as ultramafic dikes is not simply the whole-rock compositions after the corrections made above. This is because the dikes contain a large number of phenocrysts. The liquid parts of the magmas including phenocrysts at the time of intrusions are called "intruded melt", hereafter. The MgO concentrations of whole rocks corrected for alteration and elemental exchange with the host vary from 14.6 to 27.7 wt% and are negatively and linearly correlated with Al_2O_3 at nearly constant FeO concentrations (Fig. 12; Table 4) as in the case of Hawaiian basalts (e.g., Rhodes and Vollinger, 2004; Putirka, 2005). The correlation of the whole-rock composition and phenocryst abundance suggests that the linear relationships among oxide wt% are explained by a binary mixing of the phenocrysts and intruded melt for each dike. We need to know the accurate abundance and composition of the phenocrysts to properly estimate the intruded melt compositions. Although we can obtain the average amount of crystals loaded in the intruded magma by integrating the heterogeneously distributed phenocrysts over the dike width if necessary, we cannot easily estimate the chemical composition of the phenocrysts. The measured Mg# of olivine (~0.83, Fig 7a), the lowest value in the dikes, does not represent an igneous composition. This is because the current compositions of olivine phenocrysts are not those in equilibrium with the intruded melt owing to the modification through elemental exchange with the interstitial melt and further with the other constituent minerals at subsolidus by diffusion over

the grain scale. The scale of diffusional exchange between olivine phenocrysts and the surrounding melt in the dikes after the cessation of magma transportation is smaller than the sample scale. On the basis of this limitation of olivine-melt interaction, we can estimate the olivine and host melt composition at high temperature from the measured whole-rock composition listed in Table 4 and the olivine phenocryst-matrix ratio listed in Table 1 by taking the following steps.

Step1: We assume a Mg#, NiO and MnO content for olivine in equilibrium with a hypothetical intruded melt, starting with the measured $Mg\#_X$, NiO_X, and MnO_X for example. Step2: We subtract the observed amount of all olivine phenocrysts with the assumed $Mg\#_X$, NiO_X, and MnO_X contents from a whole-rock composition (Tables 1 and 4). After subtracting phenocrysts, we obtain a hypothetical intruded melt as a residue of the subtraction. This is called $melt_Z$. Step3: We calculate a Mg#, NiO, and MnO content for an olivine in equilibrium with the $melt_Z$ using the partition coefficients of Mg, Fe, Ni, and Mn between olivine and melt (Beattie et al., 1991; Kinzler et al.,1990). The calculated contents are called $Mg\#_Y$, NiO_Y, and MnO_Y. Step4: We check if the values of $Mg\#_X$, NiO_X, and MnO_X, and those of $Mg\#_Y$, NiO_Y, and MnO_Y, are respectively the same. If we assumed appropriate values of Mg#, NiO, and MnO of olivine in Step1, these values of X and Y should be the same. However, this is usually not the case. Step5: When the values of Y are different from those of X, then we go back to Step 1 and assume slightly different values of X, and go to Step 2. By repeating Step1 to Step5 until the X and Y sets of olivine compositions coincide, we obtain the intruded melt composition and the Mg#, NiO, and MnO contents of olivine in equilibrium with the intruded melt. The ratios of Fe^{3+}/ total Fe of the intruded melts are assumed to be ~0.13, which was estimated by applying the olivine-orthopyroxene-spinel oxygen geobarometry to our samples (Ballhaus et al., 1991; Sack et al.,

603 1980; O'Neill, 1987). The results are listed in Table 5. The estimated Mg#, NiO, and MnO
604 contents of olivine vary from 0.85 to 0.89, 0.08 to 0.21, and 0.17 to 0.32, respectively.

605 The examined dikes show no features suggesting vesiculation during solidification, as
606 mentioned above. This observation and the estimated emplacement pressure of the host Cumulate
607 Member (~0.6 GPa; Ozawa, 1986) suggest that the intruded melts were undersaturated with
608 water, which was retained in hydrous phases without degassing. Since the initial hydrous mineral
609 in the dikes is pargasite with ~2.5 wt% water (Table 1), we estimated the initial water content for
610 each dike by using the modal abundance of pargasite (Table 5). The estimated water contents in
611 the intruded melt vary from 0.6 to 2.3 wt%. Even for the maximum estimate (2.3 H_2O wt%), the
612 saturation pressure of the intruded melt is < ~0.1 GPa according to VOLATILECALC (Newman
613 and Lowenstern, 2002), which is distinctively lower than the pressure of solidification of the
614 dikes.

615

616 **Estimation of intruded melt compositions for trace elements**

617 The rare earth element (REE) concentrations of the measured samples do not show any
618 systematic relationships with the degree of alteration or LOI (Fig. 5c). Therefore, we infer that
619 the REE in dike samples were not modified by secondary processes, and we calculated the REE
620 of the intruded melts from the raw whole-rock data by subtracting the contribution of the
621 phenocrysts (Table 5).

622 We also estimated most of the trace elements of the intruded melts in the same way as the
623 REEs (Table 5). However, some trace elements, particularly fluid-mobile incompatible elements,
624 which are prone to secondary open processes such as alteration, show variations controlled by the

625 degree of alteration or LOI. Our samples contain secondary minerals replacing primary minerals
626 and occurring in veinlets cross-cutting the primary textures. These indicate some corrections
627 must be made for these elements. We calculated the whole-rock compositions of intruded melt
628 from the trace element and the igneous modal abundances of matrix minerals for the least altered
629 dike, DKSH2, whose matrix is composed mostly of amphibole and clinopyroxene (> 97 %; Table
630 1). The results are listed in Table 6 and plotted in Fig. S4. The calculated trace element patterns
631 of the intruded melt are smooth, and several positive anomalies of, Ba, U, and Sr noted in the
632 whole-rock data are subdued.

633

634 **Estimation of primary melt compositions**

635 It is very plausible that a magma frozen in the form of the ultramafic dike underwent
636 fractional crystallization during its ascent from the melting/melt segregation depth in the deeper
637 mantle to the intrusion site. We have to evaluate this process in order to estimate the composition
638 of a primary melt generated in the mantle. Because fractionation of olivine, the most plausible
639 fractionated mineral, strongly affects Mg#, MnO, and NiO of olivine in equilibrium with the
640 melt, these parameters are used as proxies for the extent of fractionation. We have to know the
641 mantle composition in order to adopt the proxies. The ranges of Mg#, NiO and MnO of olivine in
642 the upper mantle are known as the olivine mantle array estimated from compiled data of mantle
643 xenoliths (Takahashi et al., 1987) (see Fig. S5). The NiO contents of olivine for a given value of
644 Mg# varies by ~0.08 wt%, which corresponds to the width of the array. We adopt the lowest edge
645 of the array data field (e.g., NiO wt% = 0.36 at Mg#, 0.90). This is because olivine in the mantle
646 xenoliths analyzed by Takahashi et al. (1987) underwent various degrees of subsolidus Ni
647 exchange with pyroxenes and spinel, which increases NiO in olivine depending on the subsolidus

thermal history. The amount of fractionated olivine and the primary melt compositions for each dike are estimated by repeatedly adding olivine phenocrysts with a chemical composition in equilibrium with the melt in 0.1 wt% step until the olivine composition reaches the olivine mantle array. We used Beattie et al. (1991) and Kinzler et al. (1990) for olivine-melt partition relationships for Mg-Fe, Ni, and Mn. Starting melt compositions are the above estimated intruded melt compositions (Table 5). The estimated amounts of fractionated olivine for the four dikes are listed in Table 7. The major element compositions of the estimated primary melts are also listed in Table 7. Even if we adopt the half width of the olivine mantle array as the uncertainty of the mantle NiO (~0.04 NiO wt%), the error in the MgO of the primary melt is < 1.0 wt%.

The water and rare earth and trace element concentrations in the primary melts are also corrected for olivine addition. The results are listed in Table 7 and plotted in Fig. 13. The chondrite-normalized ratios of Dy and Yb ((Dy/Yb)n) of the primary melt of the four dikes are 1.22 - 1.40 and larger than the range of the compiled literature data of the present-day NMORB and normal back-arc basin basalts (NBAB) (0.95 - 1.20) (see below for discussion on (Dy/Yb)n).

Estimation of melting mechanisms and mantle source compositions

The estimated primary melt compositions from the ultramafic dikes reflect the melting/melt segregation conditions: pressure, temperature, degree of melting/melt segregation, and mantle source compositions. Melt segregation processes could also affect the composition. We constrained the mantle source composition and the segregation processes on the basis of the REE compositions of the primary melts estimated from the four dikes (DKSH1, DKSH2, RYO1, and RYO2). They are modeled with a one-dimensional steady-state decompressional melting

model (Ozawa, 2001) using published partition coefficients (Table S2) (Fig. 14). The modeling conditions are summarized in Table 8, and their complete lists are available in Table S3 - S6. Careful examination of the accumulated melt compositions in the near fractional melting models without any fluid influx for the four dikes show the followings. (1) Melting must have taken place in the garnet stability field irrespective of whether the mantle source is the primitive mantle (PM) or MORB mantle source (MM) in order to reproduce the weak decline of heavy rare earth elements (HREE). The extent of melting in the garnet stability field ranges from 75 to 100% of the total melting, if a near fractional melting model with complete melt accumulation is assumed (Table 8). (2) A depleted mantle source, such as a MORB mantle source (MM), is required in order to better fit the pattern of the middle rare earth elements. (3) There are two possible models to better reproduce light rare earth elements (LREE): instantaneous melt formed by near fractional melting of the MORB mantle source or accumulated melt formed by fractional melting of a slightly more depleted mantle source, such as the depleted MORB mantle source (DMM). The modeling results are essentially the same for the four examined dikes (Fig. 14 and Table 8).

The CRUS of the Tectonite Member of the Miyamori complex was inferred to have formed by fluxed fractional melting of the mantle wedge under extensive influx of a slab-derived fluid from the subducting slab strongly enriched in LREE and with anomalies of several trace elements (Ozawa and Shimizu, 1995; Yoshikawa and Ozawa, 2007). On the other hand, the REE and trace element patterns of the ultramafic dikes, as well as rocks of the Cumulate Member, do not indicate any involvement of such fluids at all. The K_2O/TiO_2 ratios of pargasite (Fig. 6), REE modeling results (Fig. 14), initial Nd and Sr isotope ratios of the whole-rock and separated clinopyroxene of the ultramafic dikes and the Cumulate Member (Yoshikawa and Ozawa, 2007) consistently show that they were derived from a depleted mantle, such as the MORB mantle

source, with insignificant involvement of any types of H_2O/CO_2-rich fluids or exotic melts. The most plausible melting mechanism is, therefore, adiabatic decompressional melting, if the wide occurrence of such MORB-type mantle material in the uppermost mantle (Cipriani et al., 2004; Workman and Hart, 2005) is taken into consideration.

Estimation of melt segregation and solidus conditions and mantle potential temperatures

We estimated the melting/melt segregation pressure by plotting the estimated primary melt compositions in the Ne'-Ol'-Qtz' ternary norm diagram (Ne'= nepheline + 0.6 albite, Ol'= olivine + 0.75 orthopyroxene and Qtz'= Quartz + 0.4 albite + 0.25 orthopyroxene) according to the method of Irvine and Barager (1971) (Fig.15). The major elements compositions are strongly controlled by pressure and temperature conditions but relatively weakly dependent on the source composition, which is close to the depleted mantle in our case as discussed above from the geochemical data. We extended the pressure isopleths constructed by Sakuyama et al. (2009) for pressures < 3 GPa to higher pressures > 3 GPa on the basis of melting experiments made at 3 and 6 GPa (Walter, 1998; see Fig. S6). The normative values of the primary melt compositions of the dikes are listed in Table 7, and the estimated melting pressures are listed in Table 9.

There are barometers based on Si-activity models (Putirka, 2008; Lee et al., 2009). We applied the model of Putirka (2008) to melt compositions produced in experiments at 6 GPa by Walter (1998) and found that the barometers give lower pressure (4.1 - 4.9 GPa). Moreover, there is a negative correlation between the difference of experimental and calculated pressures (ΔP) and temperatures (e.g., ΔP = +1.1 GPa at 1800 °C and +1.9 GPa at 1710 °C). Therefore, these barometers may not be applicable to pressures close to 6.0 GPa particularly for temperatures

715 lower than ~1700 ℃, the condition of which can be realized by the decline of solidus owing to
716 the presence of water. We, therefore, use Fig. S6 to estimate melt segregation pressures.

717 Melting/melt segregation temperature is firstly estimated for the dry case by applying
718 thermometer based on MgO content in the primary melt (Sakuyama et al., 2014):

719 $$T = 1080.7 + 54.75(-0.27074P^2 + 2.21634P - 0.99731) + 15.08MgO \quad (1),$$

720 where T is the temperature in ℃, P is the pressure in GPa, and MgO is MgO content of the melt
721 in wt%. The estimates for the dry case are listed in Table 9. The presence of amphibole in the
722 dikes, however, indicates an involvement of water in the melting. The water contents of primary
723 melts constrained above are used to correct the effect of water on melting pressures according to
724 Sakuyama et al. (2009) by the following formula after Tatsumi et al. (1983):

725 $$P^{wet} = P^{dry} + H_2O^{primary} \times \frac{0.5}{3.0} \quad (2),$$

726 where P^{wet} and P^{dry} are melting pressures in the wet and dry cases, respectively, in GPa and
727 $H_2O^{primary}$ is the H_2O content in the melt in wt%, and the effect on temperature according to
728 Medard and Grove (2008):

729 $$T^{dry} - T^{wet} = 40.4C_{H2O}^{melt} - 2.97\left(C_{H2O}^{melt}\right)^2 + 0.0761\left(C_{H2O}^{melt}\right)^3 \quad (3),$$

730 where T^{wet} and T^{dry} are melting temperatures in the wet and dry cases, respectively, in ℃, and
731 $C^{melt}{}_{H2O}$ is the H_2O content in the melt in wt%. The melt segregation temperatures and pressures
732 corrected for the water effects are 1416 - 1424 ℃ and 4.9 - 5.0 GPa, respectively, and are listed
733 in Table 9. Degrees of melting were estimated for the four dikes by two methods. One is based on
734 the dependence of Ne' on melting degree, which is constrained from melting experiments on
735 depleted mantle compositions (0.28 - 0.30 Na_2O wt%) with reports of melt fractions (Hirose and

Kushiro (1993) with the correction made by Hirschmann (2000); Walter,1998; Laporte et al., 2004; Fig. 16). This method gives 7.1 - 8.7 ± 3.5 % of degree of melting for the four dikes (DKSH1, DKSH2, RYO1, and RYO2) (Fig. 16 and Table 9). The other is based on the relationships between (Nd/Sm)n and (Dy/Yb)n using the open-system fractional melting model (Ozawa, 2001; Tables S3-S6) and the partition coefficients listed in Table S2, and yields a degree of melting of 13.7 – 20.0 ± 3.8 % (Table 9). The water concentrations in the mantle source thus range from 0.04 ± 0.02 to 0.18 ± 0.07 wt% for a 7.1 - 8.7 % degree of melting, and from 0.11 ± 0.02 to 0.31 ± 0.08 wt% for a 13.7 - 20.0 % degree of melting. It is expected that such amounts of water present in the mantle source at ~5 GPa is mostly partitioned into the melt once the solidus is reached because of the extremely high solubility of the melt at such high pressure (e.g., ~27 H_2Owt% at 3 GPa, Hodges (1974)), and that the melting degree does not increase much with further decompression. The plausible ranges of the degree of melting and water content in the source will be constrained below by comparing the solidus conditions with the water-preset solidi.

From the melting/melt segregation conditions, we further estimated solidus conditions by assuming adiabatic (decompressional) melting, which is the plausible melting mechanism, as discussed above. We extrapolate the melt segregation conditions to the solidus by the melting degrees obtained above by the two methods and the latent heat of melting according to the following equation after Asimow et al. (1997):

$$\left(\frac{\partial T}{\partial P}\right)_S = \frac{T\{\alpha^s V^s + F(\alpha^{lq} V^{lq} - \alpha^s V^s)\} + \Delta H \left(\frac{\partial F}{\partial T}\right)_P \left(\frac{\partial T}{\partial P}\right)_F}{C_p^s + F\Delta C_p + \Delta H \left(\frac{\partial F}{\partial T}\right)_P} \qquad (4),$$

where T is the temperature in K, P is the pressure in GPa, F is the melting degree, ΔH is the enthalpy change in J/Mol, α^s, and α^{lq} are the thermal expansions for solid and melt, respectively,

in 1/K, V^s, and V^{lq} are the partial volumes for solid and melt, respectively, in J/GPa, and Cp^s and Cp^{lq} are the isobaric heat capacities for solid and melt, respectively, in J/Mol/K. We used expressions for thermal expansion, molar volume, heat capacity, and enthalpy of fusion according to Lange and Carmichael (1987), Fei (1995), Berman and Brown (1985), Berman (1998), Stebbins et al. (1984), Kojitani and Akaogi (1997). The calculated adiabatic gradients and parameters used in the estimation procedures are listed in Table S7 after King (1957), Krupka et al. (1985a), Robie et al. (1982a, 1982b), Haselton and Westrum (1980).

All the solidus conditions calculated by using the degrees of melting estimated by the two methods are plotted between the water-present solidi for 0.05 and 0.1 H_2O wt% after Katz et al. (2003) (~0.08 wt%; Fig. S7). This range of water content is, however, more consistent with that based on the degree of melting estimated from the Ne' norm (0.04 ± 0.02 - 0.18 ± 0.07 wt% H_2O in the source) than that estimated from the REE contents (0.11 ± 0.02 - 0.31 ± 0.08 wt% H_2O). The higher melting degree based on the REE modeling may be attributed to a slightly more depleted source or more effective melt separation. We thus accepted the former estimates for the solidus conditions more plausible, which range from 1440 -1460 ± 30 °C and 5.3 - 5.4 ± 1.0 GPa (Table 9). The errors are estimated by propagating the largest uncertainty in the estimation of the melting pressures and temperatures. The solidus temperatures are higher than those of melt segregation by 20 to 25 °C according to Takahashi et al. (1993) (Table S7). The estimated solidus pressure indicates that the melting initiated deeper than ~170 km. These deep melting conditions are consistent with the conditions of high-pressure melting inferred from the REE patterns of primary melts (> 75 % of the total melting in the garnet stability field > ~2.5 GPa).

The estimated mantle potential temperatures (MPTs) range 1340 -1360 ± 40 °C (Table 9) by extrapolating the solidus condition to the surface along the adiabatic slope of the solid mantle,

781 18 °C/GPa (Katsura et al., 2009). The errors are estimated by propagating the uncertainty in the
782 estimation of the solidus temperature and pressure.

783

784 **Evaluation of openness of the melting systems**

785 We successfully reproduced the REE pattern of the estimated primary melt of dike
786 DKSH2 by the near fractional melting model with the DMM source and without material influx
787 (Fig. 14). However, highly incompatible trace elements cannot be fitted reasonably well. The
788 estimated water contents of the mantle source (0.04 - 0.18 wt%), which are notably higher than
789 the MORB mantle source (~0.02 wt%: Dixon et al., 1998), indicate the presence of water as
790 hydrous phase before melting or the influx of a H_2O-bearing agent during melting. Therefore, it
791 is quite plausible that a water-bearing agent enriched in highly incompatible elements was added
792 before or during melting processes. We estimated the ratios of the highly incompatible elements
793 (Ba, Sr, Nb, and Ta) of the influxed agent required to reproduce those of the primary melt of dike
794 DKSH2 by an open-system near fractional melting model (Ozawa, 2001) with the same model
795 parameters adopted to reproduce less incompatible trace elements above except for assuming
796 material influx before or during decompressional melting. The required chondrite-normalized
797 ratios ((Ba/Nb)n, (Ba/Ta)n, (Sr/Nb)n, and (Sr/Ta)n) of the agent fall within a narrow range (2.1 -
798 4.5) irrespective of influx timing. The ratios of partition coefficients between solid mantle and
799 water-rich fluids at low temperature (< 900 °C), for pairs of Ba-Nb, Ba-Ta, Sr-Nb, and Sr-Ta, are
800 12 - 110, 24 - 350, 5.0 - 6.1 and 12 - 19, respectively, and are much higher than for those of a
801 hydrous silicate melt or a supercritical fluid (0.9 - 2.1, 1.3 - 2.9, 0.7 - 1.6 and 1.0 - 2.2,
802 respectively, at 1200 °C) (Kessel et al., 2005). This implies that the water-rich agent should be a

hydrous silicate melt or a supercritical fluid. The latter is stable at a pressure higher than ~4 GPa (Mibe et al., 2007), which is consistent with the estimated melting depth > ~130 km.

DISCUSSION

Tectonic model in the Cambrian-Ordovician northeast Japan

The tectonic environment of the decompressional melting of the depleted mantle from ~170 km depth involving a minor influx of supercritical fluid is not realized in a mantle wedge at steady-state subduction because of the geochemical characteristics of the ultramafic dikes are distinct from those of arc magmas. Neither back-arc basin spreading nor ridge subduction setting are plausible because the their depths of melting are as shallow as 30 - 70 km (e.g., McKenzie and Bickle, 1988; McKenzie and O'Nions, 1991; Kinzler and Grove, 1992; Forsyth, 1993; Hirschmann and Stolper, 1996; Yamashita and Tatsumi, 1994). The flux melting of the mantle wedge forming the CRUS of the Tectonite Member had occurred in the Cambrian-Ordovician northeast Japan just before decompressional melting of the depleted mantle forming the Cumulate Member and the ultramafic dikes. Such sudden change of the melting regime to adiabatic decompressional melting of the depleted mantle at the depth of ~170 km is best explained by a slab breakoff model.

A slab breakoff model invokes a detachment of a subducting oceanic plate which induces upwelling of asthenosphere materials from above or beneath the subducting plate (Davies and von Blanckenburg, 1995). In the former case, distinct geochemical features of the mantle wedge must be inscribed in the primary melt, but it is not the case for the Cumulate Member and the ultramafic dikes as discussed above. Therefore, mantle upwelling must be dominated from the

825 bottom side of the plate. This is consistent with a result of geodynamic modeling of slab breakoff
826 (Gerya et al., 2004), where a substantial upwelling takes place from beneath the subducting plate.

827 Ozawa et al. (2015) proposed a model that the Cumulate Member was crystallized from
828 melts formed by decompressional melting of a sub-slab mantle triggered by a slab breakoff
829 during the Cambrian-Ordovician time in northeast Japan Arc. The slab breakoff model
830 constrained in our study is not in conflict with this model. Figure 17 shows a tectonic model
831 based on Ozawa et al. (2015) with our proposition of generation and transportation of the primary
832 magma frozen as the ultramafic dikes in the Cumulate Member.

833

834 **Thermal state of the Cambrian-Ordovician upper mantle**

835 The present-day MPT varies from 1370 ± 49 ℃ for mid-ocean ridges to 1620 ± 55 ℃ for
836 ocean island basalt (Putirka, 2005). The former magma generation is induced by passive
837 upwelling, and the latter by active upwelling. Thus, the wide variation of the present-day MPT
838 implies the diversity in the depths of mantle upwelling. It should be noted that the estimated
839 MPTs are within the range of 1350 - 1450 ℃ if the magma generation mechanism is restricted to
840 passive upwelling regardless of whether it occurs beneath mid-ocean ridges or back-arc basins
841 (Wiens et al., 2006). This implies that the upper mantle is globally in a fairly homogeneous
842 thermal state, which might be maintained by small-scale convection underneath the plates
843 (Richter and Parsons, 1975; van Hunen and Čadek, 2009; Takeo et al., 2018).

844 We have estimated the Cambrian-Ordovician MPT of ~1350 ± 40 ℃ in the northeast
845 Japan arc from ultramafic dikes with the specification of melting mechanism as decompression
846 melting of MORB mantle source from the sub-slab mantle. Therefore, the estimated MPT reflects

847 the global thermal state of the upper mantle because the thermal state of sub-slab mantle is
848 similar to the mantle beneath mid-ocean ridges provided that small-scale convection is
849 maintained beneath the oceanic lithosphere. We conclude that the thermal state of the upper
850 mantle in Cambrian-Ordovician time was globally similar to that of the present-day upper mantle.

851

852 **IMPLICATIONS: ORIGIN OF THE CAMBRIAN-ORDOVICIAN OPHIOLITE PULSE**

853 Cambrian-Ordovician ophiolites classified as subduction-related according to the Th/Yb-
854 Nb/Yb discrimination diagram of Pearce (2008) have high Nb/Yb ratios above the MORB-OIB
855 array (Dilek and Furnes, 2011; Furnes et al., 2014). These ophiolites, however, plot mostly in the
856 MORB field in the V-Ti discrimination diagram of Shervais (1982) (Dilek and Furnes, 2011;
857 Furnes et al., 2014). This implies that primary magmas for such ophiolites formed mostly by
858 decompressional melting of a MORB mantle source under negligible influence of slab-derived
859 fluids. The plausible mechanisms to reproduce such features have been thought to be either back-
860 arc spreading (Dilek and Furnes, 2011; Furnes et al., 2014) or ridge subduction (Shervais, 2001).

861 We compiled data of volcanic or shallow-intrusive basaltic rocks from the Cambrian-
862 Ordovician subduction-related ophiolites and examined the relationship between the chondrite-
863 normalized ratio of Dy and Yb ((Dy/Yb)n) and that of Nd and Sm ((Nd/Sm)n). They are
864 compared with primary melts formed by steady-state decompressional melting (Ozawa, 2001) of
865 a MORB mantle source that ascent from various depths with a variable extent of melting in the
866 garnet peridotite field, which is represented by percentages of melting in the garnet stability field
867 in the total melting degree (PMGF) (Figs. 18a and 18b). The data from the subduction-related
868 Cambrian-Ordovician ophiolites have a similar range of (Nd/Sm)n as that of the present-day

NMORB and NBABB, and a wide range of (Dy/Yb)n (0.97 - 1.39) with many data higher than (Dy/Yb)n of the present-day NMORB and NBABB (1.22 - 1.40; Figs. 18a and 18b). The predominance of magmas that have (Nd/Sm)n and (Dy/Yb)n ratios within the range of the present-day NMORB and NBABB suggests that the thermal state of the Cambrian-Ordovician upper mantle was not distinct from that of the present-day upper mantle. This is consistent with our estimation of MPT from the ultramafic dikes. We further infer that these NMORB or NBABB-like magmas were generated from the MORB mantle source at depths similar to the present-day spreading center (30 - 70 km, Kinzler and Grove (1992)), though the generation depths are not estimated for these ophiolites.

The (Dy/Yb)n from some of the ophiolites are as high as that of the magmas filling ultramafic dikes in the Hayachine-Miyamori ophiolite (Dy/Yb)n (> 1.2) with (Nd/Sm)n < 1.0 (Fig. 18a). Such ophiolites are: Bymarka, Norway (Slagstad, 2003); Solund-Stavfijord, Norway (Furnes et al., 2012); Star Lake, Canada (Lissenberg et al., 2005); Cabo Oltegal Complex, Spain (Sánchez-Martínez et al., 2007); Kudi, China (Fang, 1998; Jiang et al., 1992; Wang et al., 2002). The presence of magmas characterized by the high (Dy/Yb)n (> 1.2) in these ophiolites indicates partial melting of MORB mantle source at depth as deep as ~160 km. It is speculated that these magmas were generated by adiabatic decompression of sub-slab mantle caused by slab breakoff, though other magmas were generated at depths as shallow as those of MORB either through back-arc spreading or ridge subduction. This might have an implication on the Cambrian-Ordovician ophiolite pulse.

An appropriate geodynamic model for the ophiolite pulse must explain the following geological and petrological features in the Cambrian-Ordovician time. First, the MPT of the Cambrian-Ordovician upper mantle is similar to that of the present-day upper mantle. Second,

LIPs and subduction-unrelated ophiolites are scarce in contrast with the Jurassic-Cretaceous ophiolite pulse (Ernst and Buchan, 2003). Third, U-Pb zircon ages that represent ages of acidic magmatic activity have a peak at 490-530 Ma (Hawkesworth et al., 2009). The first feature suggests that the thermal effect on the surface tectonics was the same as those of the present-day plate tectonics. The second feature cannot be explained by superplume models (Ishiwatari, 1994; Dilek, 2003; Vaughan and Scarrow, 2003). The third feature suggests that the Cambrian-Ordovician ophiolite pulse corresponds to the period of the assembly of the Gondwana supercontinent (Hawkesworth et al., 2009).

A subduction termination is accompanied by a slab breakoff and ophiolite exhumation and is highly expected during arc-continent collision which induces passive upwelling of the sub-slab mantle from at least ~200 km depth (Davies and von Blanckenburg, 1995; Gerya et al., 2004). We propose a new model for the origin of the Cambrian-Ordovician ophiolite pulse, which may provide one of the alternative mechanisms for termination of one cycle of subduction as proposed by Shervais (2001) by invoking ridge subduction. The frequent occurrence of subduction termination followed by slab breakoff was the principal cause of the ophiolite pulse, which led to the formation of the Gondwana supercontinent. The slab breakoff induced the decompressional melting of the sub-slab mantle and subsequent obduction of the ophiolites. The mantle potential temperatures of Cambrian-Ordovician ophiolites are similar to the present-day value, but magmas were generated under a similar degree of melting by passive upwelling at various depths from similar to the present-day mid-ocean ridge and back-arc basin environments to the depth ~170 km (Figs. 18a and 18b). This implies that the water content of the shallow Cambrian-Ordovician upper mantle was similar to the present-day value, but that the water content at depth ~170 km or deeper beneath the subducting slab was as high as 0.04 - 0.18 wt%.

915

916 ## ACKNOWLEDGEMENTS

917 We are grateful to H. Yoshida for the analytical support and S. Sasaki for kind help in the
918 field survey. We thank J. Wakabayashi and K. Putirka for their thoughtful and constructive
919 reviews and S. Straub for her editorial efforts. This work was supported by Grant-in-Aid for JSPS
920 Research Fellow (Grant Number 17J06812) and JSPS KAKENHI (Grant Number 17H02982).

921

922 ## REFERENCES CITED

923 Abbate, E., Bortolotti, V., Passerini, P., and Principi, G. (1985) The rhythm of Phanerozoic
924 ophiolites. Ofioliti, 10, 109-138.

925 Arevalo Jr., R. and McDonough, W.F. (2008) Tungsten geochemistry and implications for
926 understanding the Earth's interior. Earth and Planetary Science Letters, 272, 656-665.

927 Arevalo Jr., R., McDonough, W.F., and Luong, M. (2009) The K/U ratio of the silicate Earth:
928 insights into mantle composition, structure and thermal evolution. Earth and Planetary
929 Science Letters, 278, 361-369.

930 Asimow, P.D., Hirschmann, M.M., and Stolper, E.M. (1997) An analysis of variations in
931 isentropic melt productivity. Philosophical Transactions of the Royal Society of London.
932 Series A: Mathematical, Physical and Engineering Sciences, 355, 255-281.

933 Bagnold, R.A. (1954) Experiments on a gravity-free dispersion of large solid spheres in a
934 Newtonian fluid under shear. Proceedings of the Royal Society of London. Series A, 225,
935 49-63.

936 Ballhaus, C., Berry, R.F., and Green, D.H. (1991) High pressure experimental calibration of the
937 olivine-orthopyroxene-spinel oxygen geobarometer: implications for the oxidation state of
938 the upper mantle. Contributions to Mineralogy and Petrology, 107, 27-40.

939 Beattie, P., Ford, C., and Russell, D. (1991) Partition coefficients for olivine-melt and
940 orthopyroxene-melt systems. Contributions to Mineralogy and Petrology, 109, 212-224.

941 Berman, R.G. (1988) Internally-consistent thermodynamic data for minerals in the system Na_2O-
942 K_2O-CaO-MgO-FeO-Fe_2O_3-Al_2O_3-SiO_2-TiO_2-H_2O-CO_2. Journal of Petrology, 29, 445-522.

943 Berman, R.G., and Brown, T.H. (1985) Heat capacity of minerals in the system Na_2O-K_2O-CaO-
944 MgO-FeO-Fe_2O_3-Al_2O_3-SiO_2-TiO_2-H_2O-CO_2: representation, estimation, and high
945 temperature extrapolation. Contributions to Mineralogy and Petrology, 89, 168-183.

946 Cipriani, A., Brueckner, H.K., Bonatti, E., and Brunelli, D. (2004) Oceanic crust generated by
947 elusive parents: Sr and Nd isotopes in basalt-peridotite pairs from the Mid-Atlantic Ridge.
948 Geology, 32, 657-660.

949 Davis, A.S., Clague, D.A., Cousens, B.L., Keaten, R., and Paduan, J.B. (2008) Geochemistry of
950 basalt from the North Gorda segment of the Gorda Ridge: evolution toward ultraslow
951 spreading ridge lavas due to decreasing magma supply. Geochemistry, Geophysics,
952 Geosystems, 9, doi:10.1029/2007GC001775.

953 Davies, G.F. (1999) Dynamic Earth: Plates, plumes and mantle convection, 458 p. Cambridge
954 University Press, UK.

955 Davies, J.H., and von Blanckenburg, F. (1995) Slab breakoff: a model of lithosphere detachment
956 and its test in the magmatism and deformation of collisional orogens. Earth and Planetary
957 Science Letters, 129, 85-102.

Dilek, Y. (2003) Ophiolite pulses, mantle plumes and orogeny. Geological Society, London, Special Publications, 218, 9-19.

Dilek, Y., and Furnes, H. (2011) Ophiolite genesis and global tectonics: geochemical and tectonic fingerprinting of ancient oceanic lithosphere. Geological Society of America Bulletin, 123, 387-411.

Dilek, Y., and Furnes, H. (2014) Ophiolites and their origins. Elements, 10, 93-100.

Dixon, J.E., Stolper, E., and Delaney, J.R. (1988) Infrared spectroscopic measurements of CO_2 and H_2O in Juan de Fuca Ridge basaltic glasses. Earth and Planetary Science Letters, 90, 87-104.

Dohmen, R., and Chakraborty, S. (2007) Fe–Mg diffusion in olivine II: point defect chemistry, change of diffusion mechanisms and a model for calculation of diffusion coefficients in natural olivine. Physics and Chemistry of Minerals, 34, 409-430.

Ehiro, M., and Suzuki, N. (2003) Re-definition of the Hayachine Tectonic Belt of Northeast Japan and a proposal of a new tectonic unit, the Nedamo Belt. Journal of Structural Geology, 47, 13-21 (in Japanese with English abstract).

Ernst, R.E., and Buchan, K.L. (2003) Recognizing mantle plumes in the geological record. Annual Review of Earth and Planetary Sciences, 31, 469-523.

Fang, A.M. (1998) The sedimentology and tectonic evolution of a fore-arc basin flysch in the Kudi ophiolite, west Kunlun, Xinjiang, China. Ph. D. thesis, Institute of Geology, Academia Sinica, Beijing (in Chinese with English abstract).

978 Fei, Y. (1995) Thermal expansion. Mineral physics and crystallography: a handbook of physical
979 constants, 2, 29-44.

980 Forsyth, D.W. (1993) Crustal thickness and the average depth and degree of melting in fractional
981 melting models of passive flow beneath mid-ocean ridges. Journal of Geophysical Research,
982 98, 16073-16079.

983 Furnes, H., Dilek, Y., and Pedersen, R.B. (2012) Structure, geochemistry, and tectonic evolution
984 of trench-distal backarc oceanic crust in the western Norwegian Caledonides, Solund-
985 Stavfjord ophiolite (Norway). Geological Society of America Bulletin, 124, 1027-1047.

986 Furnes, H., De Wit, M., and Dilek, Y. (2014) Four billion years of ophiolites reveal secular trends
987 in oceanic crust formation. Geoscience Frontiers, 5, 571-603.

988 Gerya, T.V., Yuen, D.A., and Maresch, W.V. (2004) Thermomechanical modelling of slab
989 detachment. Earth and Planetary Science Letters, 226, 101-116.

990 Hall, L.S., Mahoney, J.J., Sinton, J.M., and Duncan, R.A. (2006) Spatial and temporal
991 distribution of a C-like asthenospheric component in the Rano Rahi Seamount Field, East
992 Pacific Rise, 15°-19°S. Geochemistry, Geophysics, Geosystems, 7.

993 Haselton, H.T., and Westrum, E.F. (1980) Low-temperature heat capacities of synthetic pyrope,
994 grossular, and pyrope 60 grossular 40. Geochimica et Cosmochimica Acta, 44, 701-709.

995 Hawkesworth, C., Cawood, P., Kemp, T., Storey, C., and Dhuime, B. (2009) A matter of
996 preservation. Science, 323, 49-50.

997 Herzberg, C., Condie, K., and Korenaga, J. (2010) Thermal history of the Earth and its
998 petrological expression. Earth and Planetary Science Letters, 292, 79-88.

Hirose, K., and Kushiro, I. (1993) Partial melting of dry peridotites at high pressures: determination of compositions of melts segregated from peridotite using aggregates of diamond. Earth and Planetary Science Letters, 114, 477-489.

Hirschmann, M.M. (2000) Mantle solidus: Experimental constraints and the effects of peridotite composition. Geochemistry, Geophysics, Geosystems, 1, doi:10.1029/2000GC000070.

Hirschmann, M.M., and Stolper, E.M. (1996) A possible role for garnet pyroxenite in the origin of the "garnet signature" in MORB. Contributions to Mineralogy and Petrology, 124, 185-208.

Hodges, F.N. (1974) The solubility of H_2O in silicate melts. Carnegie Institution Washington Year book. 73, 251-255.

Irvine, T.N.J., and Baragar, W.R.A.F. (1971) A guide to the chemical classification of the common volcanic rocks. Canadian Journal of Earth Science, 8, 523-548.

Ishiwatari, A. (1994) Circum-Pacific Phanerozoic multiple ophiolite belts. In Circum-Pacific Ophiolites. In A. Ishiwatari, J. Malpas, H. Ishizuka, Eds., Proceedings of the 29th International Geological Congress Part D, p. 7-28. Kyoto.

Itano, K., and Iizuka, T. (2017) Unraveling the mechanism and impact of oxide production in LA-ICP-MS by comprehensive analysis of REE-Th-U phosphates. Journal of Analytical Atomic Spectrometry, 32, 2003-2010.

Jamieson, R.A. (1986) PT paths from high temperature shear zones beneath ophiolites. Journal of Metamorphic Geology, 4, 3-22

Jiang, C.F., Yang, J.S., Feng, B.G., Zhu, Z.Z., Zhao, M., Chai, Y.C., Shi, X.D., Wang, H.D., and Hu, J.Q. (1992) Opening–closing tectonics of the Kunlun mountains. Geological memoirs, 5, 12. Geological Publishing House, Beijing (in Chinese with English abstract).

Katsura, T., Shatskiy, A., Manthilake, M.G.M., Zhai, S., Fukui, H., Yamazaki, D., Matsuzaki, T, Yoneda, A., Ito, E., Kuwata, A., and others. (2009) Thermal expansion of forsterite at high pressures determined by in situ X-ray diffraction: The adiabatic geotherm in the upper mantle. Physics of the Earth and Planetary Interiors, 174, 86-92.

Katz, R.F., Spiegelman, M., and Langmuir, C.H. (2003) A new parameterization of hydrous mantle melting. Geochemistry, Geophysics, Geosystems, 4, doi:10.1029/2002GC000433.

Kawamura, T., Uchino, T., Kawamura, M., Yoshida, K., Nakamura, M., and Nnagata, H. (2013) Geology of the Hayachine San district. Quadrangle Series scale 1:50,000, Akita (6) no. 24, Geological Survey of Japan AIST 13-G00976 (in Japanese with English abstract).

Kessel, R., Schmidt, M.W., Ulmer, P., and Pettke, T. (2005) Trace element signature of subduction-zone fluids, melts and supercritical liquids at 120-170 km depth. Nature, 437, 724.

King, E.G. (1957) Low Temperature Heat Capacities and Entropies at 298.15° K. of Some Crystalline Silicates Containing Calcium. Journal of the American Chemical Society, 79, 5437-5438.

Kinzler, R.J., and Grove, T.L. (1992) Primary magmas of mid-ocean ridge basalts: 2. Applications. Journal of Geophysical Research, 97, 6885-6906.

1039 Kinzler, R.J., Grove, T.L., and Recca, S.I. (1990) An experimental study on the effect of
1040 temperature and melt composition on the partitioning of nickel between olivine and silicate
1041 melt. Geochimica et Cosmochimica Acta, 54, 1255-1265.

1042 Kojitani, H. and Akaogi, M. (1997) Melting enthalpies of mantle peridotite: calorimetric
1043 determinations in the system CaO-MgO-Al_2O_3-SiO_2 and application to magma generation.
1044 Earth and Planetary Science Letters, 153, 209-222.

1045 Komar, P.D. (1972) Flow differentiation in igneous dikes and sills: profiles of velocity and
1046 phenocryst concentration. Geological Society of America Bulletin, 83, 3443-3448.

1047 Krupka, K.M., Hemingway, B.S., Robie, R. A., and Kerrick, D.M. (1985) High-temperature heat
1048 capacities and derived thermodynamic properties of anthophyllite, diopside, dolomite,
1049 enstatite, bronzite, talc, tremolite and wollastonite. American Mineralogist, 70, 261-271.

1050 Kurth, M., Sassen, A., and Galer, S.J. (2004) Geochemical and isotopic heterogeneities along an
1051 island arc-spreading ridge intersection: Evidence from the Lewis Hills, Bay of Islands
1052 Ophiolite, Newfoundland. Journal of Petrology, 45, 635-668.

1053 Lange, R.A., and Carmichael, I.S. (1987) Densities of Na_2O-K_2O-CaO-MgO-FeO-Fe_2O_3-Al_2O_3-
1054 TiO_2-SiO_2 liquids: new measurements and derived partial molar properties. Geochimica et
1055 Cosmochimica Acta, 51, 2931-2946.

1056 Laporte, D., Toplis, M.J., Seyler, M., and Devidal, J.L. (2004) A new experimental technique for
1057 extracting liquids from peridotite at very low degrees of melting: application to partial
1058 melting of depleted peridotite. Contributions to Mineralogy and Petrology, 146, 463-484.

1059 Leake, B., Woolley, A.R., Arps, C.E.S., Birch, W.D., Gilbert, M.C., Grice, J.D., Hawthorne,
1060 F.C., Kato, A., Kisch, H.J., Krivovichev, V.G., and others. (1997) Nomenclature of

amphiboles: re- port of the subcommittee on amphiboles of the International Mineralogical Association, Commission on New Minerals and Mineral Names. European Journal of Mineralogy, 9, 623-651.

Lee, C.T.A., Luffi, P., Plank, T., Dalton, H., and Leeman, W.P. (2009) Constraints on the depths and temperatures of basaltic magma generation on Earth and other terrestrial planets using new thermobarometers for mafic magmas. Earth and Planetary Science Letters, 279, 20-33.

Lissenberg, C.J., Van Staal, C.R., Bédard, J.H., and Zagorevski, A. (2005) Geochemical constraints on the origin of the Annieopsquotch ophiolite belt, Newfoundland Appalachians. Geological Society of America Bulletin, 117, 1413-1426.

Maekawa, H. (1981) Geology of the Motai Group in the southwestern part of the Kitakami Mountains. Journal of the Geological Society of Japan, 87, 543-554.

Mahoney, J.J., Graham, D.W., Christie, D.M., Johnson, K.T.M., Hall, L.S., and Vonderhaar, D.L. (2002) Between a hotspot and a cold spot: isotopic variation in the Southeast Indian Ridge asthenosphere, 86°E-118°E. Journal of Petrology, 43, 1155-1176.

McDonough, W.F., and Sun, S.S. (1995) The composition of the Earth. Chemical geology, 120, 223-253.

McKenzie, D., and Bickle, M.J. (1988) The volume and composition of melt generated by extension of the lithosphere. Journal of Petrology, 29, 625-679.

McKenzie, D. and O'Nions, R. K. (1991) Partial melt distributions from inversion of rare earth element concentrations. Journal of Petrology, 32, 1021-1091.

1081 Médard, E., and Grove, T.L. (2008) The effect of H_2O on the olivine liquidus of basaltic melts:
1082 experiments and thermodynamic models. Contributions to Mineralogy and Petrology, 155,
1083 417-432.

1084 Mibe, K., Kanzaki, M., Kawamoto, T., Matsukage, K.N., Fei, Y., and Ono, S. (2007) Second
1085 critical endpoint in the peridotite-H_2O system. Journal of Geophysical Research, 112

1086 Nauret, F., Abouchami, W., Galer, S.J.G., Hofmann, A.W., Hemond, C., Chauvel, C., and
1087 Dyment, J. (2006) Correlated trace element-Pb isotope enrichments in Indian MORB along
1088 18-20°S, Central Indian Ridge. Earth and Planetary Science Letters, 245, 137-152.

1089 Newman, S., and Lowenstern, J.B. (2002) VolatileCalc: a silicate melt-H_2O-CO_2 solution model
1090 written in Visual Basic for Excel. Computers and Geosciences, 28, 597-604.

1091 Noguchi, T., Shinjo, R., Michihiro, I.T.O., Takada, J., and Oomori, T. (2011) Barite
1092 geochemistry from hydrothermal chimneys of the Okinawa Trough: insight into chimney
1093 formation and fluid/sediment interaction. Journal of Mineralogical and Petrological
1094 Sciences, 106, 26-35.

1095 O'Neill, H.S. (1987) Quartz-fayalite-iron and quartz-fayalite-magnetite equilibria and the free
1096 energy of formation of fayalite (Fe_2SiO_4) and magnetite (Fe_3O_4). American Mineralogist,
1097 72, 67-75.

1098 Ozawa, K. (1983) Relationships between tectonite and cumulate in ophiolites: the Miyamori
1099 ultramafic complex, Kitakami Mountains, northeast Japan. Lithos, 16, 1-16.

1100 Ozawa, K. (1984) Geology of the Miyamori ultramafic complex in the Kitakami Mountains,
1101 northeast Japan. Journal of the Geological Society of Japan, 90, 697-716.

Ozawa, K. (1986) Partitioning of elements between constituent minerals in peridotites from the Miyamori ultramafic complex, Kitakami Mountains, Northeast Japan: estimation of P− T condition and igneous composition of minerals. Journal of the Faculty of Science the University of Tokyo Section II, 21, 116-137.

Ozawa, K. (1987a) Origin of the Miyamori ophiolitic complex, northeast Japan: TiO_2/K_2O of amphibole and TiO_2/Na_2O of clinopyroxene as discriminants for the tectonic setting of ophiolites. In Malpas, J., Moores, E., Panayiotou, A., Xenophontos, C, Eds., Proceedings of the Ophiolite Conference, p. 485-495. Cyprus.

Ozawa K., (1987b) Petrology of aluminous spinel peridotites and pyroxenites of the Miyamori ultramafic complex, northeast Japan. Journal of the Faculty of Science, University of Tokyo. Section II, 21, 309-32.

Ozawa, K. (1988) Ultramafic tectonite of the Miyamori ophiolitic complex in the Kitakami Mountains, Northeast Japan: hydrous upper mantle in an island arc. Contributions to Mineralogy and Petrology, 99, 159-175.

Ozawa, K. (1994) Melting and melt segregation in the mantle wedge above a subduction zone: evidence from the chromite-bearing peridotites of the Miyamori ophiolite complex, northeastern Japan. Journal of Petrology, 35, 647-678.

Ozawa, K. (2001) Mass balance equations for open magmatic systems: Trace element behavior and its application to open system melting in the upper mantle. Journal of Geophysical Research, 106, 13407-13434.

Ozawa, K., and Shimizu, N. (1995) Open-system melting in the upper mantle: Constraints from the Hayachine-Miyamori ophiolite, northeastern Japan. Journal of Geophysical Research, 100, 22315-22335.

Ozawa, K., Shibata, K., and Uchiumi, S. (1988) K-Ar ages of hornblende in gabbroic rocks from the Miyamori ultramafic complex of the Kitakami Mountains. Journal of Mineralogy, Petrology and Economic Geology, 83, 150-159 (in Japanese with English abstract).

Ozawa, K., Maekawa, H., and Ishiwatari A. (2013) Reconstruction of the structure of Ordovician-Devonian arc system and its evolution processes: Hayachine-Miyamori ophiolite and Motai high-pressure metamorphic rocks in Iwate Prefecture. Journal of the Geological Society of Japan, 119, 134-53 (in Japanese with English abstract).

Ozawa, K., Maekawa, H., Shibata, K., Asahara, Y., and Yoshikawa, M. (2015) Evolution processes of Ordovician-Devonian arc system in the South-Kitakami Massif and its relevance to the Ordovician ophiolite pulse. Island Arc, 24, 73-118.

Pearce, J.A. (2008) Geochemical fingerprinting of oceanic basalts with applications to ophiolite classification and the search for Archean oceanic crust. Lithos, 100, 14-48.

Pearce, J.A., Ernewein, M., Bloomer, S.H., Parson, L.M., Murton, B.J., and Johnson, L.E. (1994) Geochemistry of Lau Basin volcanic rocks: influence of ridge segmentation and arc proximity. Geological Society, London, Special Publications, 81, 53-75.

Pearce, J.A., Stern, R.J., Bloomer, S.H., and Fryer, P. (2005) Geochemical mapping of the Mariana arc-basin system: Implications for the nature and distribution of subduction components. Geochemistry, Geophysics, Geosystems, 6, doi:10.1029/2004GC000895.

1143 Petry, C., Chakraborty, S., and Palme, H. (2004) Experimental determination of Ni diffusion
1144 coefficients in olivine and their dependence on temperature, composition, oxygen fugacity,
1145 and crystallographic orientation. Geochimica et Cosmochimica Acta, 68, 4179-4188.

1146 Pin, C., and Zalduegui, J.S. (1997) Sequential separation of light rare-earth elements, thorium and
1147 uranium by miniaturized extraction chromatography: application to isotopic analyses of
1148 silicate rocks. Analytica Chimica Acta, 339, 79-89.

1149 Pin, C., Briot, D., Bassin, C., and Poitrasson, F. (1994) Concomitant separation of strontium and
1150 samarium-neodymium for isotopic analysis in silicate samples, based on specific extraction
1151 chromatography. Analytica Chimica Acta, 298, 209-217.

1152 Putirka, K.D. (2005) Mantle potential temperatures at Hawaii, Iceland, and the mid‐ocean ridge
1153 system, as inferred from olivine phenocrysts: Evidence for thermally driven mantle plumes.
1154 Geochemistry, Geophysics, Geosystems, 6, doi:10.1029/2005GC000915.

1155 Putirka, K.D. (2008) Thermometers and barometers for volcanic systems. Reviews in mineralogy
1156 and geochemistry, 69, 61-120.

1157 Rhodes, J.M., and Vollinger, M.J. (2004) Composition of basaltic lavas sampled by phase‐2 of
1158 the Hawaii Scientific Drilling Project: Geochemical stratigraphy and magma types.
1159 Geochemistry, Geophysics, Geosystems, 5, doi:10.1029/2002GC000434.

1160 Richter, F.M., and Parsons, B. (1975) On the interaction of two scales of convection in the
1161 mantle. Journal of Geophysical Research, 80, 2529-2541.

1162 Robie, R.A., Hemingway, B.S., and Takei, H. (1982a) Heat capacities and entropies of Mg_2SiO_4,
1163 Mn_2SiO_4, and Co_2SiO_4 between 5 and 380 K. American Mineralogist, 67, 470-482.

1164 Robie, R.A., Finch, C.B., and Hemingway, B.S. (1982b) Heat capacity and entropy of fayalite
1165 (Fe_2SiO_4) between 5.1 and 383 K: comparison of calorimetric and equilibrium values for the
1166 QFM buffer reaction. American Mineralogist, 67, 463-469.

1167 Sack, R.O., Carmichael, I.S.E., Rivers, M.L., and Ghiorso, M.S. (1980) Ferric-ferrous equilibria
1168 in natural silicate liquids at 1 bar. Contributions to Mineralogy and Petrology, 75, 369-376.

1169 Sakuyama, T., Ozawa, K., Sumino, H., and Nagao, K. (2009) Progressive melt extraction from
1170 upwelling mantle constrained by the Kita-Matsuura basalts in NW Kyushu, SW Japan.
1171 Journal of Petrology, 50, 725-779.

1172 Sakuyama, T., Nakai, S.I., Yoshikawa, M., Shibata, T., and Ozawa, K. (2014) Progressive
1173 Interaction between Dry and Wet Mantle during High-temperature Diapiric Upwelling:
1174 Constraints from Cenozoic Kita-Matsuura Intraplate Basalt Province, Northwestern Kyushu,
1175 Japan. Journal of Petrology, 55, 1083-1128.

1176 Sánchez-Martínez, S., Arenas, R., Andonaegui, P., Catalán, J.R.M., and Pearce, J.A. (2007)
1177 Geochemistry of two associated ophiolites from the Cabo Ortegal Complex (Variscan belt of
1178 NW Spain). Geological Society of America Memoirs, 200, 445-467.

1179 Shervais, J.W. (1982) Ti-V plots and the petrogenesis of modern and ophiolitic lavas. Earth and
1180 planetary science letters, 59, 101-118.

1181 Shervais, J.W. (2001) Birth, death, and resurrection: The life cycle of suprasubduction zone
1182 ophiolites. Geochemistry, Geophysics, Geosystems, 2, doi:10.1029/2000GC000080.

1183 Shibata, K., and Ozawa, K. (1992) Ordovician arc ophiolite, the Hayachine and Miyamori
1184 complexes, Kitakami Mountains, Northeast Japan: isotopic ages and geochemistry.
1185 Geochemical Journal, 26, 85-97.

1186 Sims, K.W.W., Goldstein, S.J., Blichert-Toft, J., Perfit, M.R., Kelemen, P., Fornari, D.J.,
1187 Michael, P., Murrell, M.T., Hart, S.R., DePaolo, D.J., and others. (2002) Chemical and
1188 isotopic constraints on the generation and transport of magma beneath the East Pacific Rise.
1189 Geochimica et Cosmochimica Acta, 66, 3481-3504.

1190 Slagstad, T. (2003) Geochemistry of trondhjemites and mafic rocks in the Bymarka ophiolite
1191 fragment, Trondheim, Norway: petrogenesis and tectonic implications. Norwegian Journal
1192 of Geology, 83, 167-185.

1193 Stebbins, J.F., Carmichael, I.S.E., and Moret, L.K. (1984) Heat capacities and entropies of
1194 silicate liquids and glasses. Contributions to Mineralogy and Petrology, 86, 131-148.

1195 Stern, R.J. (2005) Evidence from ophiolites, blueschists, and ultrahigh-pressure metamorphic
1196 terranes that the modern episode of subduction tectonics began in Neoproterozoic time.
1197 Geology, 33, 557-560.

1198 Sun, S.S., and McDonough, W.S. (1989) Chemical and isotopic systematics of oceanic basalts:
1199 implications for mantle composition and processes. Geol. Soc. London, Special
1200 Publications, 42, 313-345.

1201 Sun, W.D., Bennett, V.C., Eggins, S.M., Arculus, R.J., and Perfit, M.R. (2003) Rhenium
1202 systematics in submarine MORB and back-arc basin glasses: laser ablation ICP- MS results.
1203 Chemical Geology, 196, 259-281.

1204 Sun, W.D., Hu, Y.H., Kamenetsky, V.S., Eggins, S.M., Chen, M., and Arculus, R.J. (2008)
1205 Constancy of Nb/U in the mantle revisited. Geochimica et Cosmochimica Acta, 72, 3542-
1206 3549.

1207 Takahashi, E. (1986) Melting of a dry peridotite KLB-1 up to 14 GPa: Implications on the origin
1208 of peridotitic upper mantle. Journal of Geophysical Research: Solid Earth, 91, 9367-9382.

1209 Takahashi, E., Uto, K., and Schilling, J.G. (1987) Primary magma compositions and Mg/Fe ratios
1210 of their mantle residues along Mid Atlantic Ridge 29° N to 73° N. Technical Report of ISEI
1211 Okayama University. Series A, 9, 1-4.

1212 Takahashi, E., Shimazaki, T., Tsuzaki, Y., and Yoshida, H. (1993) Melting study of a peridotite
1213 KLB-1 to 6.5 GPa, and the origin of basaltic magmas. Transactions of the Royal Society of
1214 London. Series A, 342, 105-120.

1215 Takeo, A., Kawakatsu, H., Isse, T., Nishida, K., Shiobara, H., Sugioka, H., Ito, A., and Utada, H.
1216 (2018). In Situ Characterization of the Lithosphere-Asthenosphere System beneath NW
1217 Pacific Ocean Via Broadband Dispersion Survey With Two OBS Arrays. Geochemistry,
1218 Geophysics, Geosystems, 19, 3529-3539.

1219 Tatsumi, Y. Sakuyama, M., Fukuyama, H., and Kushiro, I. (1983) Generation of arc basalt
1220 magmas and thermal structure of the mantle wedge in subduction zones. Journal of
1221 Geophysical Research, 88, 5815-5825.

1222 van Hunen, J., and Čadek, O. (2009) Reduced oceanic seismic anisotropy by small-scale
1223 convection. Earth and Planetary Science Letters, 284, 622-629.

1224 Vaughan, A.P., and Scarrow, J.H. (2003) Ophiolite obduction pulses as a proxy indicator of
1225 superplume events? Earth and Planetary Science Letters, 213, 407-416.

1226 Walter, M.J. (1998) Melting of garnet peridotite and the origin of komatiite and depleted
1227 lithosphere. Journal of Petrology, 39, 29-60.

Wang, Z., Sun, S., Li, J., and Hou, Q. (2002) Petrogenesis of tholeiite associations in Kudi ophiolite (western Kunlun Mountains, northwestern China): implications for the evolution of back-arc basins. Contributions to Mineralogy and Petrology, 143, 471-483.

Wiens, D.A., Kelley, K.A., and Plank, T. (2006) Mantle temperature variations beneath back-arc spreading centers inferred from seismology, petrology, and bathymetry. Earth and Planetary Science Letters, 248, 30-42.

Williams, H., and Smyth, R. (1973) Metamorphic aureoles beneath ophiolite suites and Alpine peridotites: Tectonic implications with west Newfoundland examples. American Journal of Science, 273, 594-621.

Workman, R.K., and Hart, S.R. (2005) Major and trace element composition of the depleted MORB mantle (DMM). Earth and Planetary Science Letters, 231, 53-72.

Xia, X., and Song, S. (2010) Forming age and tectono-petrogenises of the Jiugequan ophiolite in the North Qilian Mountain, NW China. Chinese Science Bulletin, 55, 1899-1907.

Yakubchuk, A.S., Nikishin, A.M., and Ishiwatari, A. (1994) A late Proterozoic ophiolite pulse. In A. Ishiwatari, J. Malpas, H. Ishizuka, Eds., Proceedings of the 29th International Geological Congress Part D, p. 273-286. Kyoto.

Yamashita, S., and Tatsumi, Y. (1994) Thermal and geochemical evolution of the mantle wedge in the northeast Japan arc: 2. Contribution from geochemistry. Journal of Geophysical Research, 99, 22285-22293.

Yoshida, H., and Takahashi, N. (1997) Chemical behavior of major and trace elements in the Horoman mantle diapir, Hidaka belt Hokkaido, japan. Journal of Mineralogy, Petrology and Economic Geology, 92, 391-409 (in Japanese with English abstract).

Yoshikawa, M., and Nakamura, E. (2000) Geochemical evolution of the Horoman peridotite complex: Implications for melt extraction, metasomatism, and compositional layering in the mantle. Journal of Geophysical Research, 105, 2879-2901.

Yoshikawa, M., and Ozawa, K. (2007) Rb-Sr and Sm-Nd isotopic systematics of the Hayachine-Miyamori ophiolitic complex: Melt generation process in the mantle wedge beneath an Ordovician island arc. Gondwana Research, 11, 234-246.

Figure Captions

Fig. 1: (a): Simplified geological map of the northwestern part of southern Kitakami Mountains showing distributions of the Miyamori and Hayachine ultramafic-mafic complexes in the Hayachine−Miyamori (HM) Ophiolite, Ordovician-Devonian strata, and Silurian-Devonian granitic rocks (after Ehiro and Suzuki, 2003; Kawamura at al., 2013; Ozawa, 1984; Maekawa, 1981). Gray rectangle in (a) represents the plot region of (b). (b): Geological map of the southern part of the Miyamori ultramafic-mafic complex located to the east of the Hizume-Kesennuma fault (modified after Ozawa et al., 2013). Localities of examined ultramafic dikes are shown by filled stars with locality numbers in (b). The dikes occur in the Cumulate Member near the contact with the Tectonite Member.

Fig. 2: (a) Field occurrence of the ultramafic dike (DK) in the host dunite (HD) at locality #1 in Fig. 1b. The inset in the upper left corner shows an outline of the dike. This dike shows porphyritic texture with olivine (dark spots) and minor clinopyroxene phenocrysts set in the matrix. It shows zoning in phenocryst modes; olivine phenocrysts are abundant in the central

1272 darker zone and fewer in the brighter marginal zones. The dike has short branches, indicated with
1273 arrows. (b): A view of a polished slab taken from the central part of the dike (a rectangle marked
1274 with b in (a)) showing abundant olivine phenocrysts (~ 50 vol%; Table 1) with euhedral-
1275 subhedral morphology. (c): A view of a polished slab in the marginal part of the dike (a rectangle
1276 marked with c in (a)) showing a smaller amount of phenocrysts (~20 vol%; Table 1) and their
1277 shape-preferred orientation (outlined with white dashed lines) elongate parallel to the contact. A
1278 few millimeter-thick branch, shown with a white arrow, is present.

1279

1280 Fig. 3: Photomicrograph of thin sections made from ultramafic dikes (DKSH2 and RYO1): (a)
1281 Wide view of the center of DKSH2 in an open nicol, (b) magnified view of the area between an
1282 olivine phenocryst and a plagioclase pseudomorph in RYO1 under open nicol, and (c) that under
1283 crossed nicols. In (a), olivine (ol) phenocrysts are euhedral to subhedral and set in the matrix
1284 consisting mostly of polycrystalline amphibole (amph). Orthopyroxene (opx), partially (or
1285 totally) altered into darker fine-grained aggregate, occur rimming olivine, and plagioclase
1286 pseudomorph (pl) occur in the middle of the amphibole matrix. Euhedral-subhedral chromian
1287 spinel (sp) grains are included in olivine or amphibole. In (b) and (c), orthopyroxene is mostly
1288 unaltered and occur rimming the olivine phenocryst.

1289

1290 Fig. 4: Whole-rock Al_2O_3 and Fe_2O_3 contents in wt% of examined samples of dikes plotted
1291 against MgO wt%. Triangle, circle, square, and diamond indicate examined dikes: DKSH1,
1292 DKSH2, RYO1, and RYO2, respectively (Fig. 1b; Table 1). Symbols with a dot, vertical line,
1293 plus, and cross denote samples from the edge, margin, and center of dikes, and rootless block

without information on sample position in the dike, respectively. Large symbols indicate weakly altered, and small symbols indicate samples showing intermediate or strong alteration. The solid lines connect two pairs of samples with different degrees of alteration, but the other features, such as sampling location in the dike and igneous modal abundance, are the same.

Fig. 5: CI-chondrite normalized whole-rock trace element and rare earth element (REE) patterns of 10 samples from 4 dikes (localities, #1, #2, #3, and #4; Fig. 1b, Table 1). Six samples are from dikes with homogeneous phenocryst distribution, shown in (a) and (c), and four samples from dikes zoned in terms of phenocryst abundance, shown in (b) and (d). The CI-chondrite composition is after McDonough and Sun (1995). Symbols are the same as in Fig. 4. Shaded symbols with a dashed line indicate samples with a weak alteration.

Fig. 6: Present-day values of $^{87}Sr/^{86}Sr$ and $^{143}Nd/^{144}Nd$ of whole-rocks and separated clinopyroxene phenocrysts for examined 4 ultramafic dikes (a) and other mafic and ultramafic rocks in the Hayachine-Miyamori ophiolite from the literature (b). Symbols and paring lines in (a) are the same as those used in Fig. 4 except for star in the square, which denotes clinopyroxene separated from a sample indicated by arrows. Plotted in (b) are literature data for pyroxenes separated from the chromite-bearing Ultramafic Suite (CRUS) (solid inverted triangle), aluminous spinel-bearing Ultramafic Suite (ASUS) (open inverted triangle) (Yoshikawa and Ozawa, 2007), the Cumulate Member of the Miyamori complex (thick cross) (Ozawa et al., 2015) and the hornblende-rich mafic-ultramafic rocks (cross) (Shibata and Ozawa, 1992). The

rectangle in (b) represents the plot region of (a). The area for mid-ocean ridge basalt (MORB) in (b) is according to the compilation by Yoshikawa and Nakamura (2000).

Fig. 7: Spatial variations of Mg# of minerals (a) and NiO wt% in olivine (b) crossing the contact between ultramafic dikes and host dunite for DKSH2 (locality #2; Fig. 1b). The distance is measured from the boundary taken positive towards the center of the dike and negative towards the dunite host. Vertical lines indicate the positions of the dike-host boundary, where the igneous modal abundance abruptly changes. Horizontal lines indicate the lowest grain-averaged values of the central homogeneous part of DKSH2, which are 0.833 in Mg# and 0.20 wt% in NiO.

Fig. 8: Chemical compositions of spinel plotted in the triangular diagram of Cr, Al, and Fe^{3+} in examined four ultramafic dikes. Circle, square, triangle, and diamond are the same as those used in Fig. 4. Open and solid symbols indicate euhedral-subhedral grain included in olivine/amphibole and anhedral grain occurring near plagioclase, respectively. Cross indicates spinel in the host dunite.

Fig. 9: K_2O/TiO_2 ratio of amphibole in wt% forming the matrix of examined ultramafic dikes. The data fields for amphibole from the aluminous Spinel Ultramafic Suite (ASUS), the Chromite-bearing Ultramafic Suite (CRUS), and the Cumulate Member (Cumulate) of the Hayachine-Miyamori ophiolite (Ozawa, 1988) are also shown. The ranges of magma compositions from various tectonic settings are after Ozawa (1988). Circle and diamond are the same as those used in Fig. 4. The data of amphibole in the ultramafic dikes are plotted in the field of normal mid-

ocean ridge basalt. Abbreviations: NMORB, normal mid-ocean ridge basalt; OIPB, oceanic intra-plate basalt; BABB, back-arc basin basalt; EMORB, enriched mid-ocean ridge basalt; IAB, island arc basalt; CFB, continental flood basalt; CRB, continental rift basalt; CAB, continental alkali basalt; KIMB, kimberlite; HMA, high magnesian andesite; LAMP, lamproite.

Fig. 10: CI-chondrite normalized trace element patterns of clinopyroxene and amphibole (a) and rare earth element (REE) pattern of plagioclase pseudomorph (fine-grained aggregate mostly consisting of grossular) (b) in weakly altered dike DKSH2. These minerals consist of the matrix of olivine and clinopyroxene phenocrysts. The ranges of 7 analyses of amphibole from 2 samples (DKSH2MW and DKSH2CW), 5 analyses of clinopyroxene from 2 samples (DKSH2MW, DKSH2CW), and 4 analyses of plagioclase pseudomorph from 1 sample (DKSH2CW) are shown by filled or shaded areas. The REE pattern of plagioclase pseudomorph in (b) has a remarkable positive Eu anomaly and depletion in heavy REEs, which confirms the plagioclase origin of the aggregate. The CI-chondrite composition is after McDonough and Sun (1995).

Fig. 11: Whole-rock Al_2O_3 (a), MgO (b), and Fe_2O_3 (c) contents of two pairs of samples from dike DKSH2 plotted against their loss on ignition (LOI). Each pair, connected by a solid line, was sampled within ~4 cm distant in the same dike and has the same igneous modal composition and texture but a difference in alteration degree (Table 1). Symbols with a vertical line and a cross indicate margin and center of the dike, respectively. Data with large symbols are from less altered, and those with small symbols are from more altered samples. The gray vertical bands indicate the range of initial water content (1.31 - 1.36 wt%) estimated from the water contents of

amphibole and the igneous modal abundances of each sample. Correction of alteration was made by linearly extrapolating the tie lines to the expected initial water content as shown by the dashed lines. The restored original major elements contents (open circles) and the mean slopes of the tie lines are listed in Tables 4 and S1, respectively.

Fig. 12: Alteration-corrected whole-rock Al_2O_3 (a) and Fe_2O_3 (b) contents plotted against MgO for nine samples of the examined four dikes. Symbols are the same as those used in Fig. 3. The restored compositions form linear trends.

Fig. 13: Chondrite-normalized trace element patterns in primary melts being in equilibrium with mantle peridotite estimated for the four dikes (a), and the range of chondrite-normalized rare earth element (REE) pattern (b). The REE patterns of mid-ocean ridge basalts and ocean island basalts after Sun and McDonough (1989) are shown in (b) for comparison. Symbols in (a) are the same as those used in Fig. 4. All trace element and REE data are after correction of the influence of secondary modifications.

Fig. 14: Comparison of the chondrite-normalized rare earth element (REE) patterns of modeled and observed (solid lines with symbols; see Fig. 4) of the primary melts in equilibrium with mantle peridotite for four dikes (DKSH2, (a); DKSH1, (b); RYO1, (c); and RYO2, (d)). The adopted models are based on a one-dimensional steady-state decompressional melting model of Ozawa (2001) with adjustment of model parameters to best reproduce the observation. Effects of two of the most critical model parameters, mantle source composition and strength of melt

separation, are shown for accumulated melt and primitive mantle, thick solid line; accumulated melt and MORB mantle source, solid line; accumulated and depleted MORB mantle source, dotted line; and instantaneous melt and MORB mantle source, dashed line (Table 8). The complete lists of optimized model parameters are listed in Tables S3, S4, S5, and S6 for the examined four dikes. The REE abundances in the primitive mantle are after McDonough and Sun (1995), and those of the mantle source of mid-ocean ridge basalt (MORB) and depleted MORB are after Workman and Hart (2005). The CI-chondrite composition is after McDonough and Sun (1995).

Fig. 15: Normative composition of the primary melts estimated from 4 dikes (Table 7; DKSH1, open triangles; DKSH2, open circles; RYO1, open squares; and RYO2, open diamonds) plotted in the ternary diagram of Ne'- Qtz'- Ol'. Pressure isopleths defining the compositions of partial melts of the anhydrous system are after Sakuyama et al. (2009) for the low-pressure region (< 3.0 GPa). For high-pressure above 3.0 GPa, the isopleths are based on data of the high-pressure melting experiment of Walter (1998) (see Fig. S6). The projection scheme is after Irvine and Barager (1971): Ne'= Nepheline + 0.6Albite; Qtz'= Quartz + 0.4 Albite + 0.25 Orthopyroxene; Ol'= Olivine + 0.75 Orthopyroxene.

Fig. 16: Relationship between normative values of Ne' of primary melt (C_m) and degree of melting (f) for a given Na_2O content of mantle source (C_s) at two pressure ranges (1 - 3 GPa, dashed lines, and 4 - 6 GPa, dotted lines). The dashed lines ($C_m = aC_s/(0.04+0.96f,\ a=11)$ are based on the experiments at 1 - 3 GPa (Laporte et al, (2004); Hirose and Kushiro (1993)

1403 recalculated according to Hirschmann (2000)) and the dotted lines ($C_m = aC_s /(0.1 + 0.9f,\ a = 11$)
1404 are based on experiments at 4 - 6 GPa (Walter, 1998), The gray region represents the range for
1405 the MORB mantle source (0.28 - 0.3 Na_2O wt%: Workman and Hart, 2005; Takahashi, 1986) at 3
1406 - 6 GPa. Open and solid symbols connected with each other represent Na_2O content of the
1407 primary melts and estimated degrees of melting for four dikes (DKSH1, triangle; DKSH2, circle;
1408 RYO1, square; and RYO2, diamond).

1409

1410 Fig. 17: Slab breakoff model in the latest stage of the Hayachine-Miyamori ophiolite evolution
1411 during the Cambrian-Ordovician time constrained by melt generation depths, mantle source
1412 compositions, and melting mechanism for the primary melt, the composition of which was
1413 estimated from the four ultramafic dikes in this study. Passive upwelling (thick arrow) of the sub-
1414 slab mantle from >170 km depth is assumed to have been triggered by slab breakoff (Ozawa et
1415 al., 2015). Thin gray arrow shows melt transport through a fast path. Abbreviations: E, east; W,
1416 west.

1417

1418 Fig.18: Relationship between chondrite normalized ratio of Nd and Sm ((Nd/Sm)n) and that of
1419 Dy/Yb ((Dy/Yb)n) for the ultramafic dikes (Table 5) of the Hayachine-Miyamori ophiolite as
1420 stars with errors and the other Cambrian-Ordovician subduction-related ophiolites, which are (a)
1421 Bymarka (Slagstad, 2003); Solund-Stavfijord (Furnes et al., 2012); Kudi (Fang, 1998; Wang et
1422 al., 2002); Cabo Oltegal Complex (Sánchez-Martínez et al., 2007); Star Lake (Lissenberg et al.,
1423 2005), and (b) Bay of Islands (Kurth et al., 2005); Jiugequan (Xia and Song, 2010);
1424 Annieopsquotch (Lissenberg et al., 2005). Also shown are trends of accumulated partial melts

produced by fractional melting of the MORB mantle source (Workman and Hart, 2005). The melting model assumed steady-state decompressional melting with continuous melt separation starting from various depths of the garnet stability field (Ozawa, 2001). The adopted melt separation rates (γ) are 0.99, 0.96, 1.00, and 1.00 for the reaction extents (t) of 0.001, 0.02, 0.15 and 0.2, respectively. Solid curves represent the weight percentage of the degree of melting in the garnet stability field in the total melting (PMGF), and the dashed curves represent the degree of melting in weight fraction (F). Compiled literature data of the normal mid-ocean ridge basalts (NMORB) (Arevalo Jr. and McDonough, 2008; Arevalo Jr. et al., 2009; Davis et al., 2008; Hall et al., 2006; Mahoney et al., 2002; Nauret et al., 2006; Sims et al., 2002; Sun et al., 2003; Sun et al., 2008) and those of normal back-arc basin basalts (NBABB) (Arevalo Jr. and McDonough, 2008; Pearce et al., 2005; Pearce et al., 1994) are also shown for comparison. The CI-chondrite composition is after McDonough and Sun (1995).

Table 1: Whole-rock chemical compositions, igneous modal compositions, alteration degrees of examined ultramafic dikes.

Dike	DKSH1			DKSH2					RYO1	RYO2
Locality no.	#1			#2					#3	#4
Phenocryst distribution	zoned [1]			homogeneous					homogeneous	zoned [1]
Position	edge	margin	center	edge	margin		center		rootless rock	rootless rock
Sample	DKSH1ES	DKSH1MI	DKSH1CI	DKSH2EI	DKSH2MI	DKSH2MW	DKSH2CI	DKSH2CW	RYO1I	RYO2I
(wt%)										
SiO_2	40.14	41.63	42.59	42.86	42.76	42.62	42.81	42.53	43.41	41.22
TiO_2	1.07	0.44	0.45	0.68	0.69	0.66	0.76	0.62	0.56	0.56
Al_2O_3	6.55	5.90	4.32	4.24	5.27	7.50	4.64	7.39	7.43	8.42
Fe_2O_3	13.82	12.24	11.83	11.23	11.17	11.50	11.38	11.43	9.98	9.32
MnO	0.15	0.19	0.23	0.19	0.18	0.17	0.19	0.18	0.18	0.21
MgO	25.24	29.75	31.67	32.38	30.31	27.99	30.97	28.13	22.25	19.38
CaO	13.01	9.64	8.86	8.39	9.43	8.61	9.15	8.79	15.94	20.86
Na_2O	0.01	0.16	0.03	0.00	0.14	0.83	0.06	0.81	0.23	0.00
K_2O	0.01	0.03	0.02	0.02	0.03	0.11	0.03	0.11	0.01	0.00
P_2O_5	0.01	0.01	0.01	0.01	0.01	0.01	0.01	0.01	0.03	0.03
Total	100.00	100.00	100.00	100.00	100.00	100.00	100.00	100.00	100.00	100.00
Loss on ignition	6.26	5.22	5.40	6.35	5.43	2.72	6.10	3.02	4.39	5.87
(ppm)										
Ni	599	927	983	943	919	836	931	780	498	379
Cr	1406	1588	1729	1570	1457	1376	1534	1277	1529	1371
Ba	96	110	101	98	119	112	104	133	94	93
U	0.04	0.01	0.08	0.02	0.04	0.13	0.04	0.08	0.02	0.01
Nb	1.22	0.48	0.63	0.89	1.09	1.35	1.30	1.11	0.60	0.73
Ta	0.07	0.03	0.04	0.06	0.07	0.07	0.09	0.07	0.06	0.05
La	1.68	1.44	1.48	0.93	1.07	1.07	1.40	1.06	1.05	0.74
Ce	4.08	3.17	3.11	2.90	3.25	3.15	4.05	3.08	2.78	2.59
Pr	0.81	0.52	0.48	0.58	0.61	0.62	0.76	0.59	0.53	0.48
Pb	0.34	0.30	0.32	0.61	0.86	0.86	1.04	0.79	1.85	0.87
Sr	309	146	146	175	195	198	164	223	87	70
Nd	4.90	2.61	2.53	3.66	3.97	4.00	4.40	3.58	3.37	3.18
Hf	0.91	0.47	0.49	0.63	0.68	0.68	0.76	0.62	0.68	0.58
Zr	20.45	13.20	13.73	14.99	16.45	17.20	20.13	16.44	16.89	14.47
Sm	1.83	0.82	0.87	1.26	1.41	1.30	1.46	1.19	1.20	1.27
Eu	0.71	0.36	0.42	0.40	0.50	0.52	0.63	0.48	0.44	0.50
Gd	2.58	1.27	1.26	1.71	1.84	1.77	2.07	1.69	1.72	1.69
Tb	0.45	0.21	0.20	0.28	0.31	0.30	0.34	0.27	0.28	0.30
Dy	3.03	1.48	1.54	1.97	2.07	2.01	2.42	1.87	1.92	2.09
Y	15.09	7.86	8.12	9.99	10.69	10.33	12.31	9.63	10.57	9.94
Ho	0.62	0.31	0.31	0.40	0.42	0.40	0.48	0.39	0.40	0.44
Er	1.73	0.88	0.90	1.13	1.20	1.15	1.38	1.06	1.17	1.17
Tm	0.24	0.12	0.13	0.15	0.17	0.16	0.19	0.15	0.15	0.15
Yb	1.55	0.83	0.83	1.01	1.12	1.08	1.27	0.97	0.98	1.00
Lu	0.22	0.12	0.12	0.15	0.16	0.16	0.18	0.15	0.14	0.15
Modal composition (vol%)										
Phenocrysts										
olivine	14.00	25.67	31.19	34.83	25.31		27.18		14.20	7.65
orthpyroxene	3.50	14.01	11.76	2.52	13.07		10.95		9.03	12.24
clinopyroxene	2.46	1.38	2.75	-					7.53	4.12
Total	19.96	41.06	45.70	37.35	38.38		38.13		30.76	24.01
Matrix										
amphibole	36.77	41.49	41.14	60.66	56.50		54.52		29.79	18.82
clinopyroxene	36.01	14.20	7.61	0.13	1.87		2.34		15.71	24.41
orthpyroxene	-			1.32	-		-		3.91	7.17
plagioclase	-	1.72	2.69	-	2.02		2.40		18.41	25.29
spinel	7.26	1.52	2.87	0.53	1.23		2.61		1.42	0.29
Total	80.04	58.94	54.30	62.65	61.62		61.87		69.24	75.99
Extent of replacement by secondary low-temperature minerals [3]										
Overall	strong	intermediate	intermediate	intermediate	intermediate	weak	intermediate	weak	intermediate	intermediate
Phenocrysts										
olivine	×	○	○	○	○	○	○	○	△	△
orthpyroxene	×	×	×	×	×	△	×	△	○	○
clinopyroxene	△	○	○	-	-	-	-	-	○	○
Matrix										
amphibole	×	×	×	×	×	○	×	○	△	△
clinopyroxene	△	○	○	○	○	○	○	○	○	○
plagioclase	-	×	×	×	×	×	×	×	×	×
spinel	△	○	○	○	○	○	○	○	○	○

[1] Phenocrysts are concentrated in the dike center.

[2] Orthopyroxene always occurs rimming olivine phenocrysts.

[3] ○, weak (< 20 %); △, intermediate (20 - 60 %); ×, extensive (60 - 100 %).

Table 2: Sm–Nd and Rb–Sr isotopic compositions of selected samples from four ultramafic dikes (see Table 1).

Dike	Sample	$^{87}Rb/^{86}Sr$	$^{147}Sm/^{144}Nd$	$^{143}Nd/^{144}Nd$		$^{87}Sr/^{86}Sr$		Sr_I [1]	εNd_I [1]
					2σ (10^{-6})		2σ (10^{-6})		
Whole rock									
DKSH1	DKSH1ES	0.0023	0.224	0.513031	4.7	0.703511	9.8	0.703495	6.0
	DKSH1MI	0.0063	0.199	0.512975	7.9	0.703432	12.8	0.703387	6.4
	DKSH1CI	0.0026	0.200	0.512986	9.1	0.703458	12.4	0.703440	6.6
DKSH2	DKSH2EI	0.0013	0.202	0.513020	5.8	0.703498	12.0	0.703489	7.1
	DKSH2MI	0.0019	0.204	0.513021	5.9	0.703432	14.1	0.703419	7.0
	DKSH2MW	0.0070	0.212	0.513021	5.3	0.703219	9.0	0.703169	6.5
	DKSH2CI	0.0027	0.204	0.513009	5.7	0.703456	8.8	0.703437	6.8
	DKSH2CW	0.0091	0.211	0.513013	5.8	0.703234	10.8	0.703169	6.4
RYO1	RYO1I	0.0121	0.215	0.513047	6.6	0.703693	9.9	0.703607	6.8
RYO2	RYO2I	0.0177	0.225	0.513079	7.6	0.703955	15.6	0.703829	6.8
Separated clinopyroxene									
RYO1	CPXRYO1I	0.0075	0.228	0.513055	6.8	0.703701	12.4	0.703648	6.1

[1] Sr_I and Nd_I are initial $^{87}Sr/^{86}Sr$ and initial $^{143}Nd/^{144}Nd$, respectively at 499Ma (Ozawa et al., 2015).

Table 3: Results of examination of mass balance of MgO between the dike (DKSH2) and its host dunite from the Mg# profile crossing their contact shown in Fig. 7. The mass of MgO lost from the host with the initial Mg# = 0.9, which is the homogeneous Mg# of olivine in the host away from the contact, and the mass gained by the dike with assumed initial Mg# = 0.83, which is the mean Mg# at the dike center, are calculated. If the former is given as unity, the latter is calculated to be 1.15, which implies that the diffusional Mg-Fe exchange between the dike and the host took place almost in a closed system under subsolidus condition.

	host dunite	dike (DKSH2)
Observed zoning profile		
variation width (mm)	50	54
area ratio of the profile	0.31	0.69
Mg#		
mean of all analyses	0.90	0.84
mean at a flat segment far away from the contact	0.90	0.83
Modal abundance (wt%)		
olivine	99.9	37.0
amphibole	-	58.3
clinopyroxene	-	0.1
orthopyroxene	-	3.9
MgO mass balance		
olivine	1.00	0.75
amphibole	-	0.36
clinopyroxene	-	0.00
orthopyroxene	-	0.04
Total	1.00	1.15

Table 4: Major element contents of the examined four dike samples after the correction of alteration (ALT) and after the correction of high-temperature diffusional modification (High-T). The latter correction is necessary for DKSH1ES and DKSH2EI sampled taken from the dike edges, but the DKSH1ES is too altered to make the reliable correction as done for DKSH2EI.

Dike	DKSH1			DKSH2						RYO1	RYO2
Sample	DKSH1ES	DKSH1MI	DKSH1CI	DKSH2EI		DKSH2MI	DKSH2MW	DKSH2CI	DKSH2CW	RYO1I	RYO2I
Correction	ALT	ALT	ALT	ALT	ALT & High-T	ALT	ALT	ALT	ALT	ALT	ALT
(wt%)											
SiO_2	39.73	41.28	42.22	42.46	42.13	42.42	42.47	42.42	42.36	43.11	40.81
TiO_2	0.92	0.31	0.32	0.54	0.53	0.58	0.62	0.62	0.57	0.45	0.41
Al_2O_3	11.06	9.53	8.11	8.42	8.40	8.75	8.66	8.75	8.84	10.62	13.05
Fe_2O_3	14.17	12.51	12.12	11.55	13.04	11.44	11.58	11.70	11.53	10.23	9.69
MnO	0.13	0.18	0.22	0.18	0.18	0.17	0.17	0.18	0.18	0.17	0.20
MgO	20.54	25.96	27.69	28.00	26.89	26.66	26.75	26.68	26.58	18.92	14.57
CaO	11.89	8.73	7.91	7.35	7.33	8.56	8.31	8.13	8.41	15.14	19.71
Na_2O	1.32	1.21	1.13	1.22	1.22	1.16	1.17	1.25	1.24	1.16	1.35
K_2O	0.16	0.15	0.15	0.16	0.16	0.14	0.14	0.16	0.16	0.12	0.15
P_2O_5	0.01	0.01	0.01	0.01	0.01	0.01	0.01	0.01	0.01	0.03	0.03
NiO	0.05	0.10	0.10	0.10	0.09	0.10	0.10	0.09	0.09	0.04	0.02
Cr_2O_3	0.02	0.02	0.02	0.02	0.02	0.02	0.02	0.02	0.02	0.02	0.02
Total	100.00	100.00	100.00	100.00	100.00	100.00	100.00	100.00	100.00	100.00	100.00
Amphibole abundance (wt%)	39.32	39.39	38.95	58.29	-	54.41	54.41	52.32	52.32	31.55	19.34
H_2O (wt%) [1]	0.98	0.98	0.97	1.46	-	1.36	1.36	1.31	1.31	0.79	0.48

[1] Whole-lock water content calculated from the water content of amphibole (2.5wt%) and its modal abundance.
Major element oxides are recalculated to 100 wt % volatile free.

Table 5: Major and trace element contents and normative compositions of intruded melts and chemical composition of olivine phenocrysts in equilibrium with the melts estimated for each examined dike. For two dikes (DKSH2 and DKSH1) mean values and their standard errors (±1SE) are listed.

Dike	DKSH1		DKSH2		RYO1	RYO2
		1SE [1]		1SE [1]		
Intruded melt						
Major oxides (wt%)						
SiO_2	43.52	0.64	44.19	0.05	44.58	41.46
TiO_2	0.56	0.02	0.98	0.02	0.62	0.53
Al_2O_3	15.78	0.51	14.64	0.08	14.64	16.89
FeO	9.57	0.09	9.57	0.26	7.38	6.40
MnO	0.20	0.01	0.18	0.00	0.15	0.17
MgO	11.43	0.10	12.76	0.12	8.72	5.98
CaO	14.89	0.15	13.73	0.31	20.86	25.50
Na_2O	2.10	0.00	2.03	0.03	1.59	1.74
K_2O	0.27	0.00	0.26	0.01	0.16	0.20
P_2O_5	0.02	0.00	0.02	0.00	0.04	0.04
Fe_2O_3	1.60	0.02	1.59	0.04	1.23	1.07
NiO	0.02	0.00	0.02	0.00	0.01	0.00
Cr_2O_3	0.03	0.00	0.03	0.00	0.02	0.02
Total	100.00		100.00		100.00	100.00
H_2O	1.74	0.04	2.27	0.05	1.08	0.62
Trace elements (ppm)						
Ba	187	1	189	9	128	120
U	0.08	0.04	0.10	0.03	0.03	0.02
Nb	0.99	0.12	1.91	0.12	0.82	0.94
Ta	0.06	0.01	0.12	0.01	0.08	0.06
La	2.59	0.08	1.85	0.11	1.43	0.95
Ce	5.58	0.10	5.49	0.29	3.79	3.33
Pr	0.89	0.00	1.05	0.05	0.72	0.61
Pb	0.55	0.03	1.39	0.10	2.53	1.12
Sr	259	6	319	15	119	89
Nd	4.56	0.07	6.54	0.29	4.60	4.08
Hf	0.85	0.03	1.13	0.04	0.92	0.75
Zr	23.9	0.9	28.4	1.2	23.1	18.6
Sm	1.50	0.06	2.21	0.11	1.64	1.64
Eu	0.69	0.05	0.85	0.05	0.61	0.64
Gd	2.25	0.05	3.03	0.10	2.35	2.17
Tb	0.37	0.01	0.50	0.02	0.38	0.39
Dy	2.69	0.10	3.46	0.14	2.63	2.68
Y	14.2	0.5	17.7	0.7	14.4	12.8
Ho	0.55	0.02	0.70	0.03	0.55	0.56
Er	1.59	0.05	1.97	0.08	1.59	1.50
Tm	0.22	0.01	0.27	0.01	0.21	0.20
Yb	1.47	0.04	1.82	0.08	1.34	1.28
Lu	0.22	0.01	0.27	0.01	0.19	0.19
Olivine in equilibrium with intruded melt						
Mg#	0.88	0.00	0.89	0.00	0.88	0.85
NiO (wt%)	0.21	0.00	0.21	0.01	0.14	0.08
MnO (wt%)	0.20	0.02	0.17	0.00	0.21	0.32
Abundance (wt%)	43.6	2.0	40.1	0.3	26.8	22.2

Major element oxides are recalculated to 100 wt % volatile free.

[1] standard error of the mean

Table 6: Concentrations of highly incompatible trace elements in amphibole and clinopyroxene consisting the matrix of DKSH2. The trace element concentrations of the matrix estimated from the weight fraction and chemical compositions of the amphibole and clinopyroxene listed in the first and second columns, respectively, are shown in the last column.

	Amphibole		Clinopyroxene		estimated matrix	
	Average	1SE [1]	Average	1SE [1]		1SE [1]
(ppm)						
Ba	38.4	3.0	5.4	2.7	37.1	2.9
U	0.11	0.01	0.04	0.00	0.10	0.01
Nb	2.57	0.18	0.07	0.01	2.47	0.17
Ta	0.17	0.02	0.01	0.00	0.17	0.02
Pb	0.44	0.03	0.06	0.01	0.42	0.03
Sr	243	11	36	5	235	10
Hf	0.94	0.04	1.01	0.04	0.94	0.04
Zr	31.1	1.3	33.2	0.5	31.2	1.3

[1] standard error of the mean

Table 7: Major and trace element concentrations and normative composition of the primary melts in equilibrium with the residual peridotites estimated for each examined dike. The chemical compositions of olivine in the residual peridotites are also listed. The mean values and their ±1SE are shown for two dikes (DKSH2 and DKSH1) with multiple samples (Table 1).

Dike	DKSH1		DKSH2		RYO1	RYO2
		1SE [1]		1SE [1]		
Primary melt						
Major oxides (wt%)						
SiO_2	43.28	0.58	43.85	0.06	44.15	41.36
TiO_2	0.51	0.01	0.88	0.02	0.55	0.46
Al_2O_3	14.37	0.50	13.13	0.10	12.94	14.66
FeO	9.64	0.10	9.54	0.25	7.64	6.98
MnO	0.20	0.01	0.18	0.00	0.16	0.18
MgO	14.74	0.18	16.52	0.19	13.37	11.54
CaO	13.56	0.17	12.31	0.30	18.45	22.13
Na_2O	1.92	0.00	1.82	0.02	1.41	1.51
K_2O	0.24	0.00	0.23	0.00	0.14	0.17
P_2O_5	0.02	0.00	0.02	0.00	0.04	0.04
Fe_2O_3	1.45	0.02	1.43	0.04	1.09	0.93
NiO	0.04	0.00	0.05	0.00	0.04	0.03
Cr_2O_3	0.03	0.00	0.02	0.00	0.02	0.02
Total	100.00		100.00		100.00	100.00
H_2O	1.59	0.03	2.05	0.04	0.96	0.54
Trace elements (ppm)						
Ba	171	2	33	3	114	105
U	0.07	0.04	0.09	0.01	0.03	0.02
Nb	0.91	0.11	2.23	0.15	0.73	0.82
Ta	0.06	0.01	0.15	0.01	0.07	0.05
La	2.37	0.07	1.67	0.10	1.28	0.83
Ce	5.10	0.08	4.95	0.26	3.38	2.91
Pr	0.81	0.01	0.95	0.04	0.64	0.54
Pb	0.51	0.03	0.38	0.03	2.25	0.98
Sr	236	5	212	9	106	78
Nd	4.17	0.05	5.90	0.21	4.10	3.57
Hf	0.78	0.03	0.85	0.04	0.82	0.65
Zr	21.88	0.80	28.14	1.14	20.56	16.28
Sm	1.37	0.05	1.99	0.10	1.46	1.43
Eu	0.63	0.05	0.76	0.05	0.54	0.56
Gd	2.05	0.04	2.73	0.09	2.09	1.90
Tb	0.33	0.01	0.45	0.02	0.34	0.34
Dy	2.46	0.09	3.12	0.12	2.34	2.35
Y	12.98	0.44	15.93	0.62	12.86	11.18
Ho	0.50	0.01	0.63	0.02	0.49	0.49
Er	1.45	0.05	1.78	0.07	1.42	1.31
Tm	0.20	0.01	0.25	0.01	0.18	0.17
Yb	1.35	0.03	1.64	0.07	1.20	1.12
Lu	0.20	0.00	0.24	0.01	0.17	0.17
Norm components[2]						
Ne'	23.3	0.5	20.9	0.4	23.3	22.7
Qtz'	0.3	0.2	2.1	0.4	0.0	0.0
Ol'	76.4	0.7	77.0	0.3	76.7	77.3
Olivine in equilibrium with primary melt						
Mg#	0.90	0.00	0.91	0.00	0.91	0.91
NiO (wt%)	0.37	0.00	0.38	0.00	0.38	0.38
MnO (wt%)	0.16	0.01	0.13	0.00	0.14	0.19
Added mass (wt%)	9.4	0.2	10.9	0.4	12.3	14.2

[1] standard error of the mean

[2] C. I. P. W norm mineral components calculated from primary melt (Ne'= nepheline + 0.6albite, Ol'= olivine + 0.75olthopyroxene and Qtz'= Quartz + 0.4albite + 0.25olthopyroxene)

Major element oxides of the estimated primary melts are recalculated to 100 wt % volatile free.

Table 8: Percentage of melting in the garnet stability field (PMGF) in the total melting degree that reproduces the rare earth element pattern of primary melt for each dike (Fig. 14) by a steady-state one-dimensional decompressional melting model (Ozawa, 2001). The PMGFs are optimized for several sets of two of the model parameters: strength of melt separation shown in the first column and mantle source shown in the second column.

Dike	Strength of melt separation	Mantle source [1]	PMGF (%)
DKSH1	accumulated	PM	95.7
		MS	88.7
		DMS	87.3
	instantaneous	MS	99.9
DKSH2	accumulated	PM	89.2
		MS	76.6
		DMS	75.5
	instantaneous	MS	99.9
RYO1	accumulated	PM	97.2
		MS	90.1
		DMS	93.0
	instantaneous	MS	99.9
RYO2	accumulated	PM	98.0
		MS	93.9
		DMS	93.9
	instantaneous	MS	99.9

[1] PM, primitive mantle; MS, MORB mantle source; DMS, depleted MORB mantle source.

Table 9: Segregation conditions (pressures, temperatures, and degrees of melting) of estimated primary melts for the examined four dikes and their solidus conditions (pressures and temperatures) and mantle potential temperatures. The solidus conditions were estimated by assuming an adiabatic decompressional melting. The standard errors listed in the last column (1SE) were estimated by propagating the uncertainty in the pressure and temperature estimation, which overwhelms the other uncertainties.

Dike	DKSH1	DKSH2	RYO1	RYO2	1SE
Segregation conditions before H_2O correction					
T (℃)	1490	1510	1470	1440	30
P (GPa)	4.7	4.7	4.8	4.9	1.0
after H_2O correction					
T (℃)	1430	1430	1430	1420	30
P (GPa)	5.0	5.0	4.9	5.0	1.0
degree of melting [1] (wt%)					
Ne' norm	7.1	8.7	7.1	7.5	3.5
REE ratios	18.5	16.8	19.7	16.3	3.8
Solidus condition					
T (℃)	1440	1460	1450	1440	30
P (GPa)	5.3	5.4	5.3	5.3	1.0
Mantle potential temperature (℃)	1350	1360	1350	1340	40

[1] The degree of melting was estimated by two methods. One is based on the dependence of Ne' normative composition on melting degree (Ne' norm) and the other is based on the relationships between REE ratios (REE ratios). We adopted the melting degree based on the Ne' norm to calculate solidus conditions and potential temperatures. See the main text for the reasons and more details.

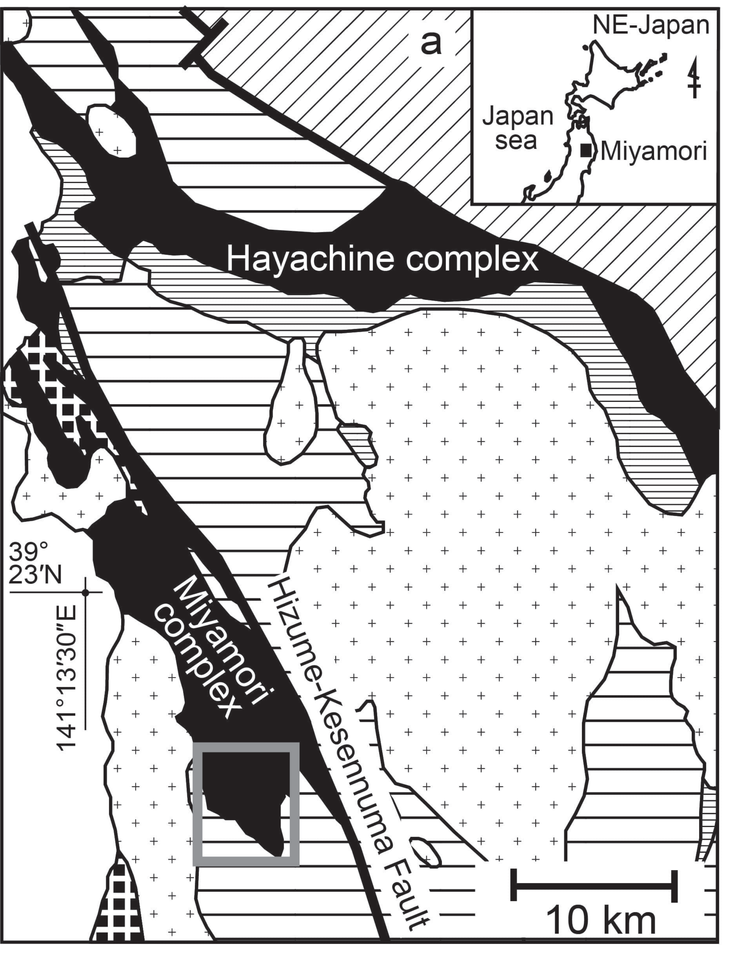

Post-Devonian strata
Silurian and Devonian strata
Motai metamorphic rocks
Hayachine-Miyamori Complex
fault
Tertiary and Quatenary strata
Cretaceous granitic rock
Jurassic accretionary complex

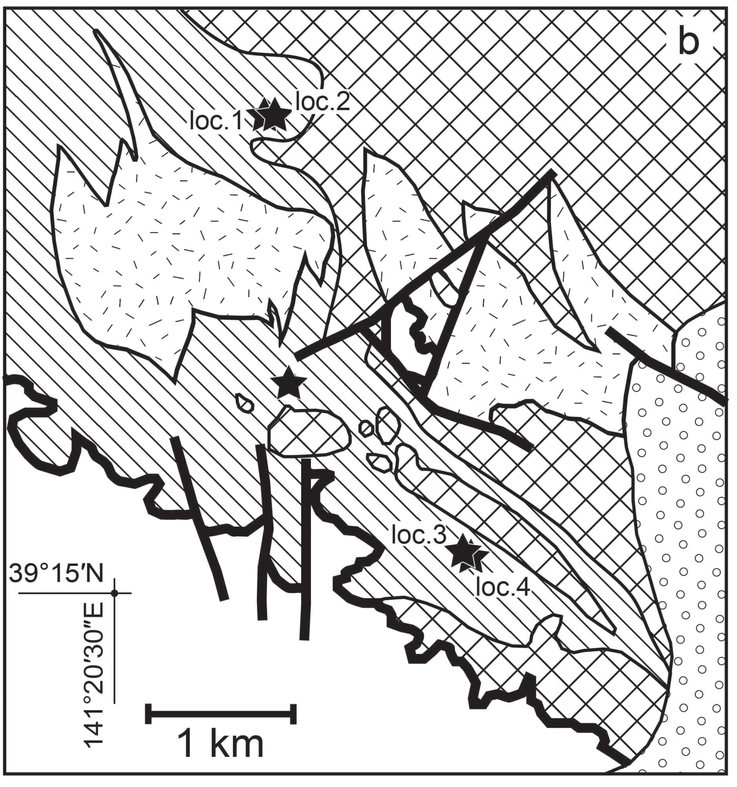

Miyamori complex
hornblende-rich mafic-ultramafic intrusion
ultramafic dike
Cumulate member
Tectonite member
fault
Cretaceous strata
Paleozoic strata

Fig.1

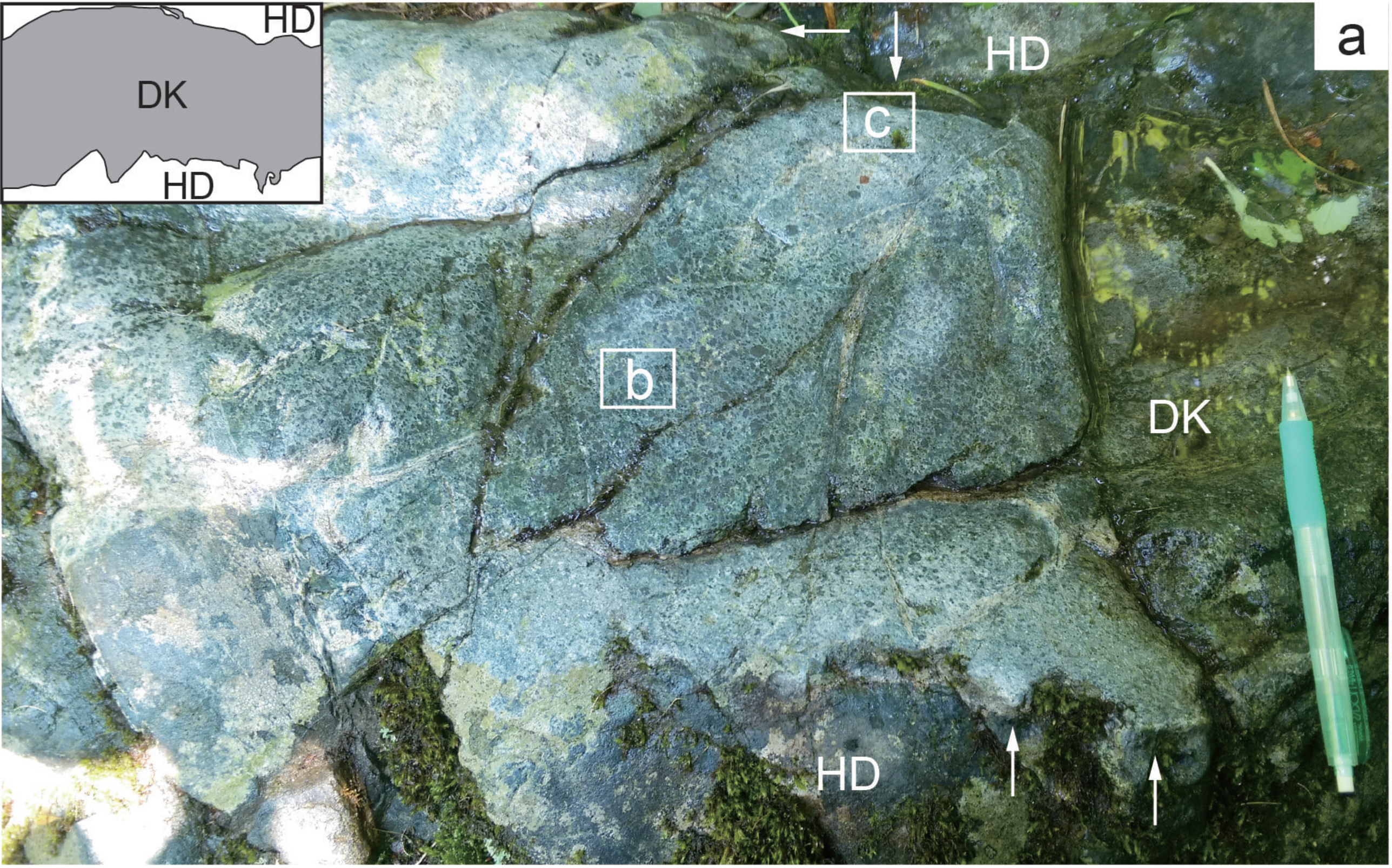

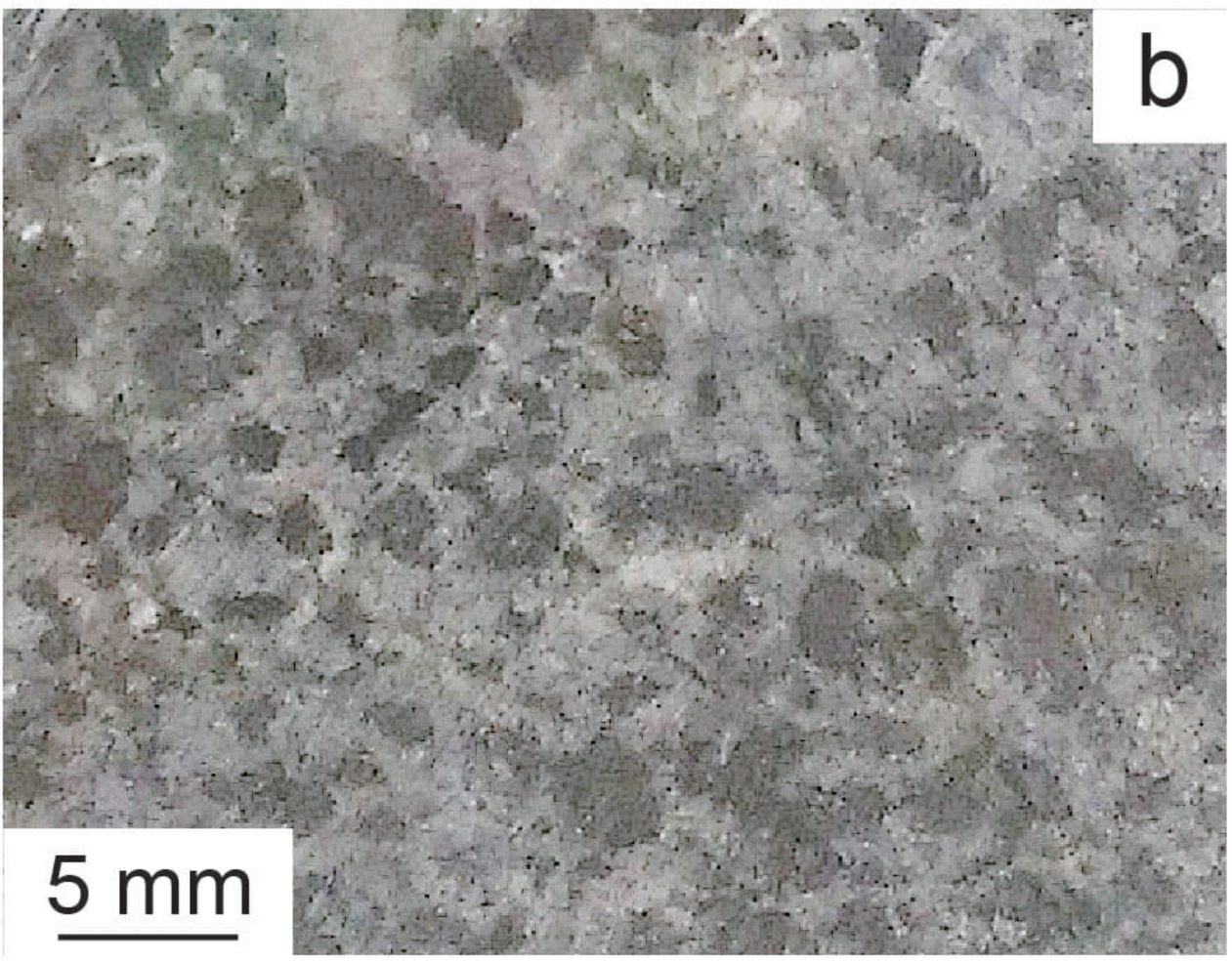

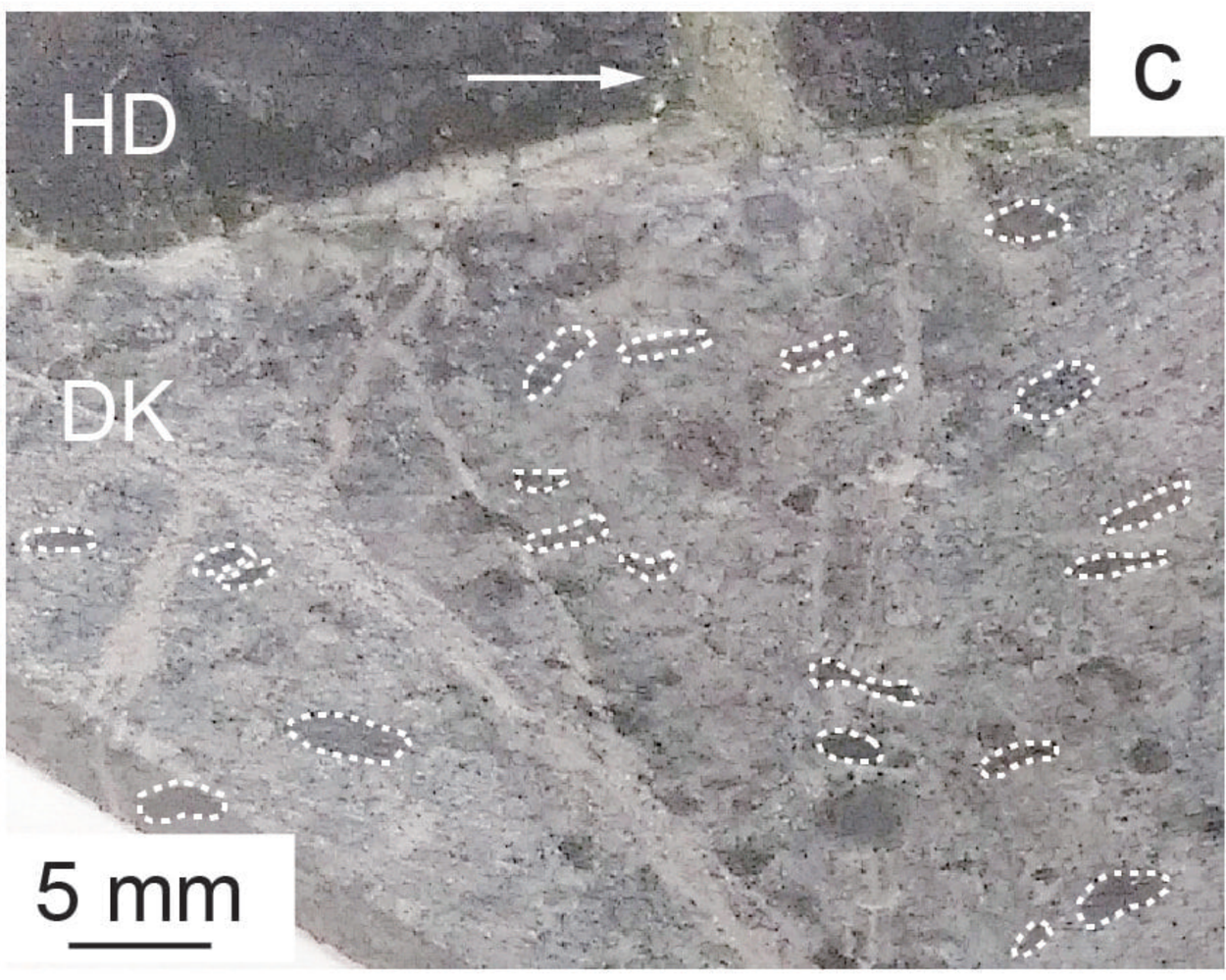

Fig.2

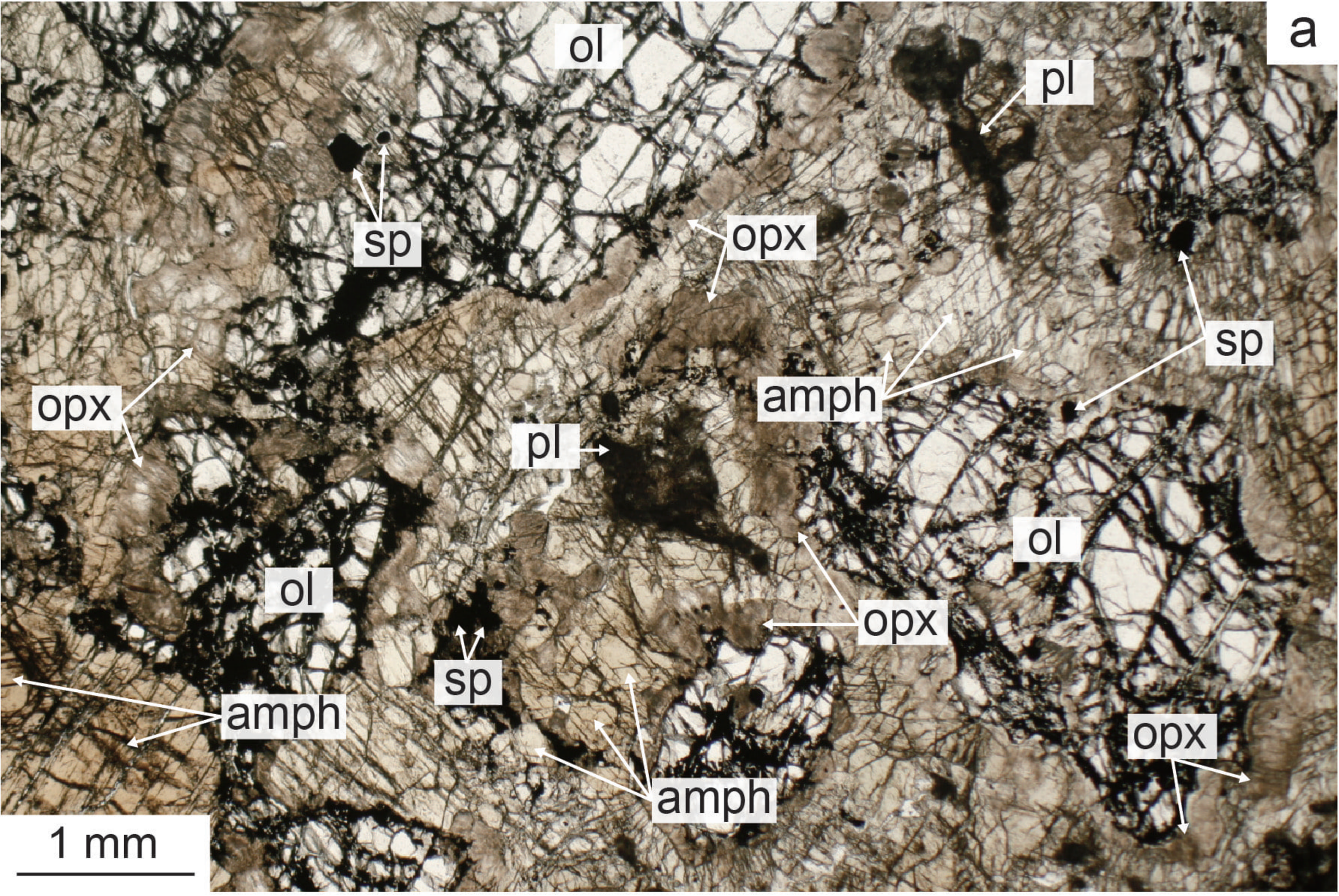
a
ol
pl
sp
opx
amph
sp
opx
pl
ol
opx
ol
sp
amph
opx
amph
1 mm

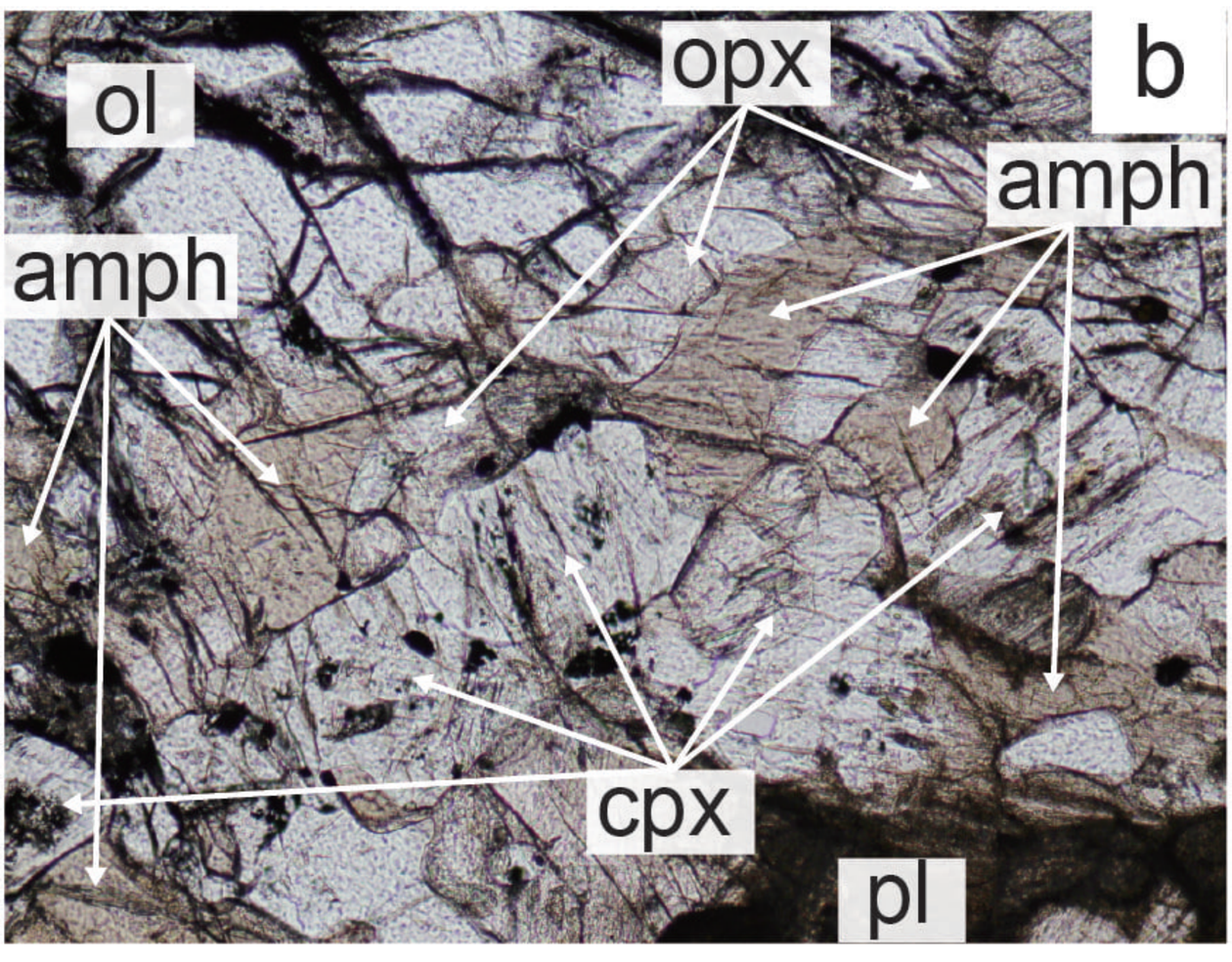
b
opx
ol
amph
amph
cpx
pl

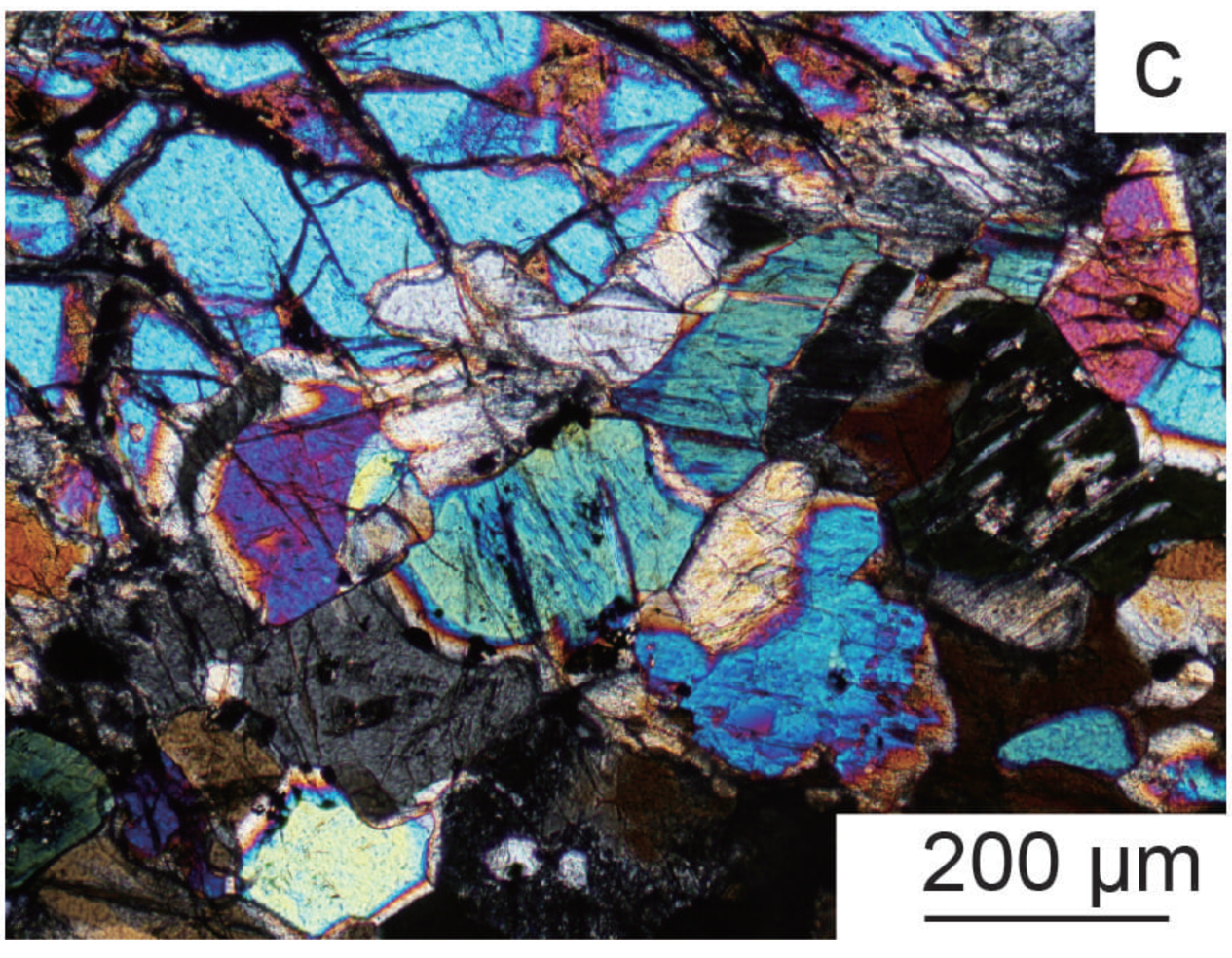
c
200 µm

Fig.3

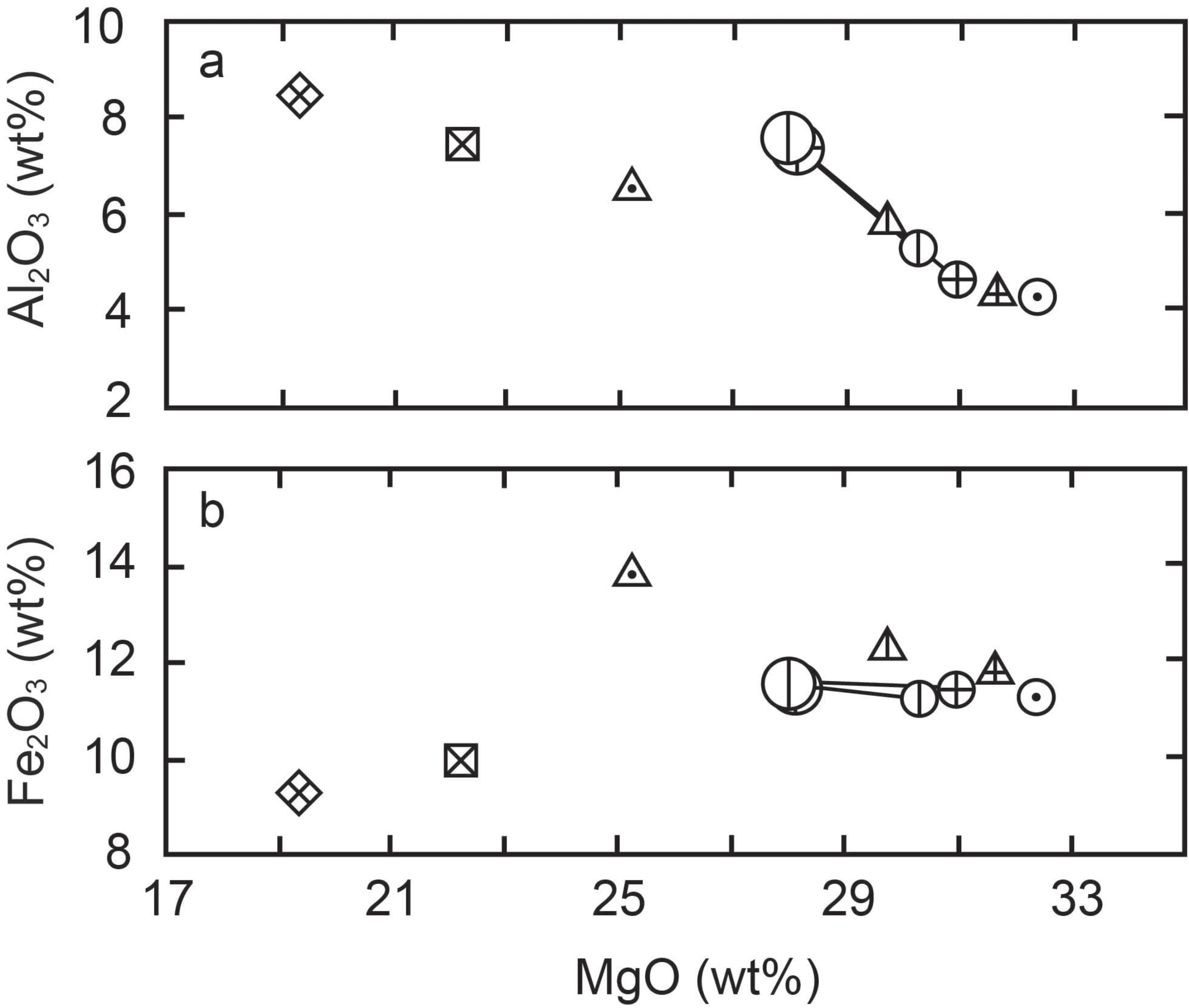
a
b
Al_2O_3 (wt%)
Fe_2O_3 (wt%)
MgO (wt%)
10
8
6
4
2
16
14
12
10
8
17
21
25
29
33
weakly altered
DKSH2
intermediately altered
DKSH1
DKSH2
RYO1
RYO2
position
edge
margin
center
unknown

Fig.4

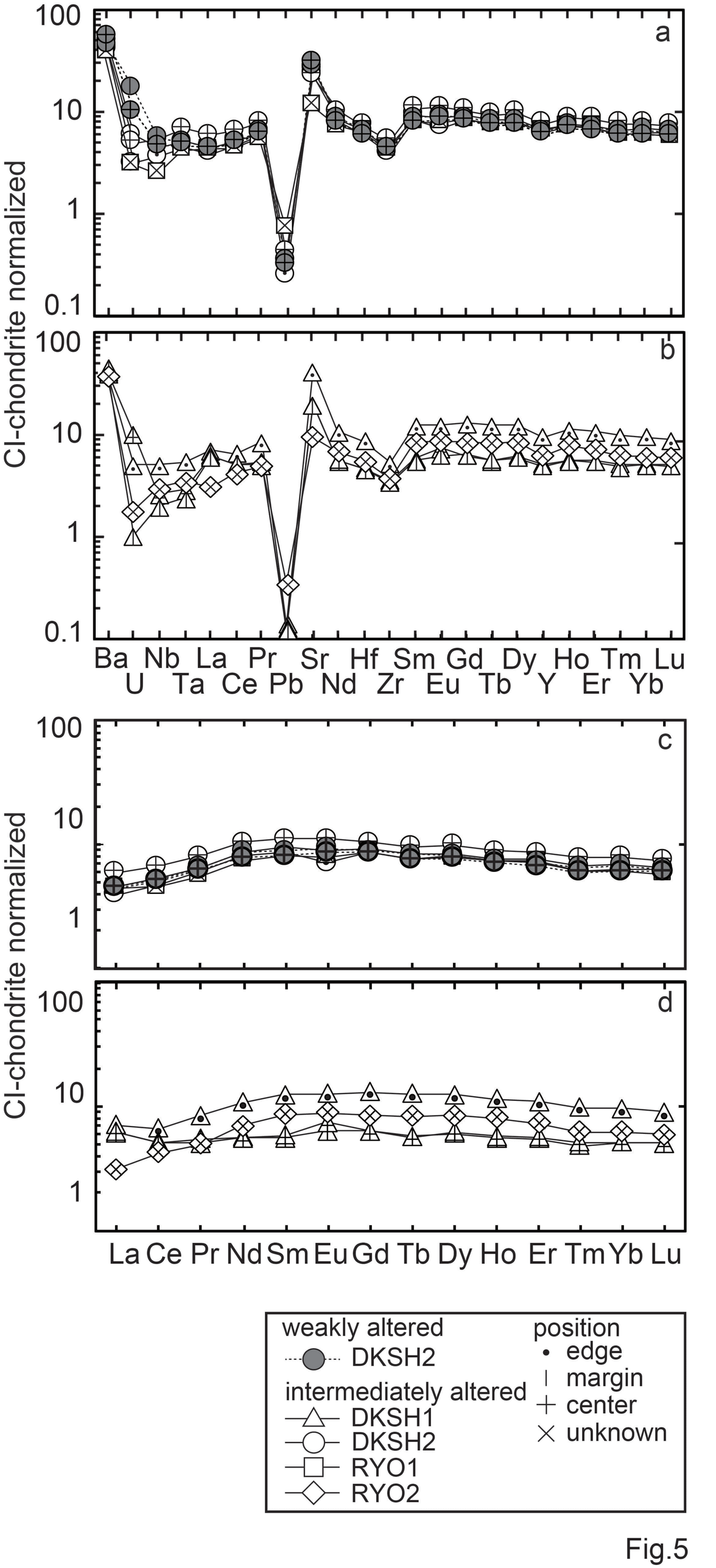
a
b
c
d
100
10
1
0.1
Cl-chondrite normalized
Ba Nb La Pr Sr Hf Sm Gd Dy Ho Tm Lu
U Ta Ce Pb Nd Zr Eu Tb Y Er Yb
La Ce Pr Nd Sm Eu Gd Tb Dy Ho Er Tm Yb Lu
weakly altered
DKSH2
intermediately altered
DKSH1
DKSH2
RYO1
RYO2
position
edge
margin
center
unknown

Fig.5

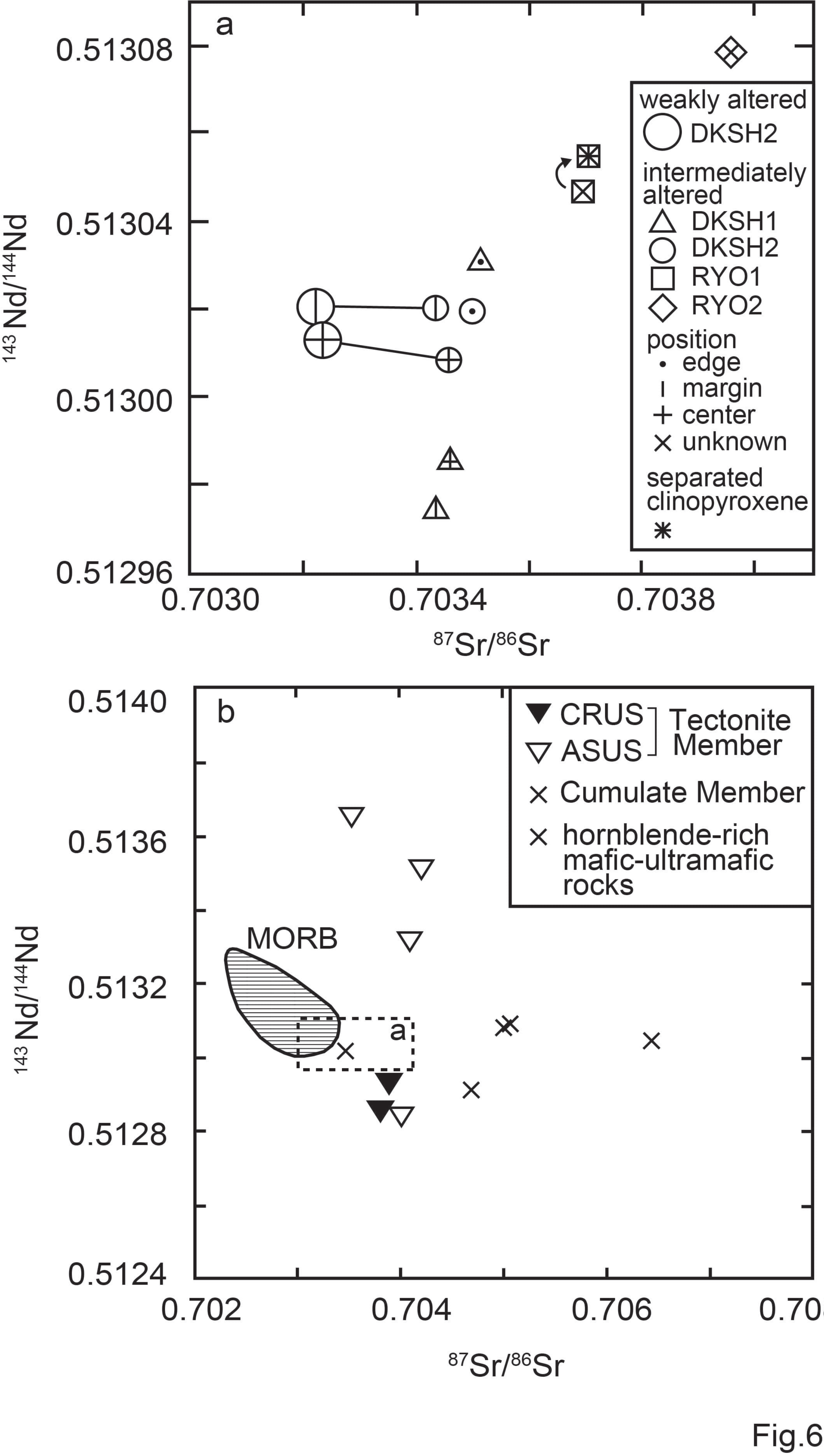
a
0.51308
0.51304
0.51300
0.51296
143Nd/144Nd
0.7030
0.7034
0.7038
87Sr/86Sr
weakly altered
DKSH2
intermediately altered
DKSH1
DKSH2
RYO1
RYO2
position
edge
margin
center
unknown
separated clinopyroxene
b
0.5140
0.5136
0.5132
0.5128
0.5124
CRUS
ASUS
Tectonite Member
Cumulate Member
hornblende-rich mafic-ultramafic rocks
MORB
a
0.702
0.704
0.706
0.708
87Sr/86Sr
143Nd/144Nd

Fig.6

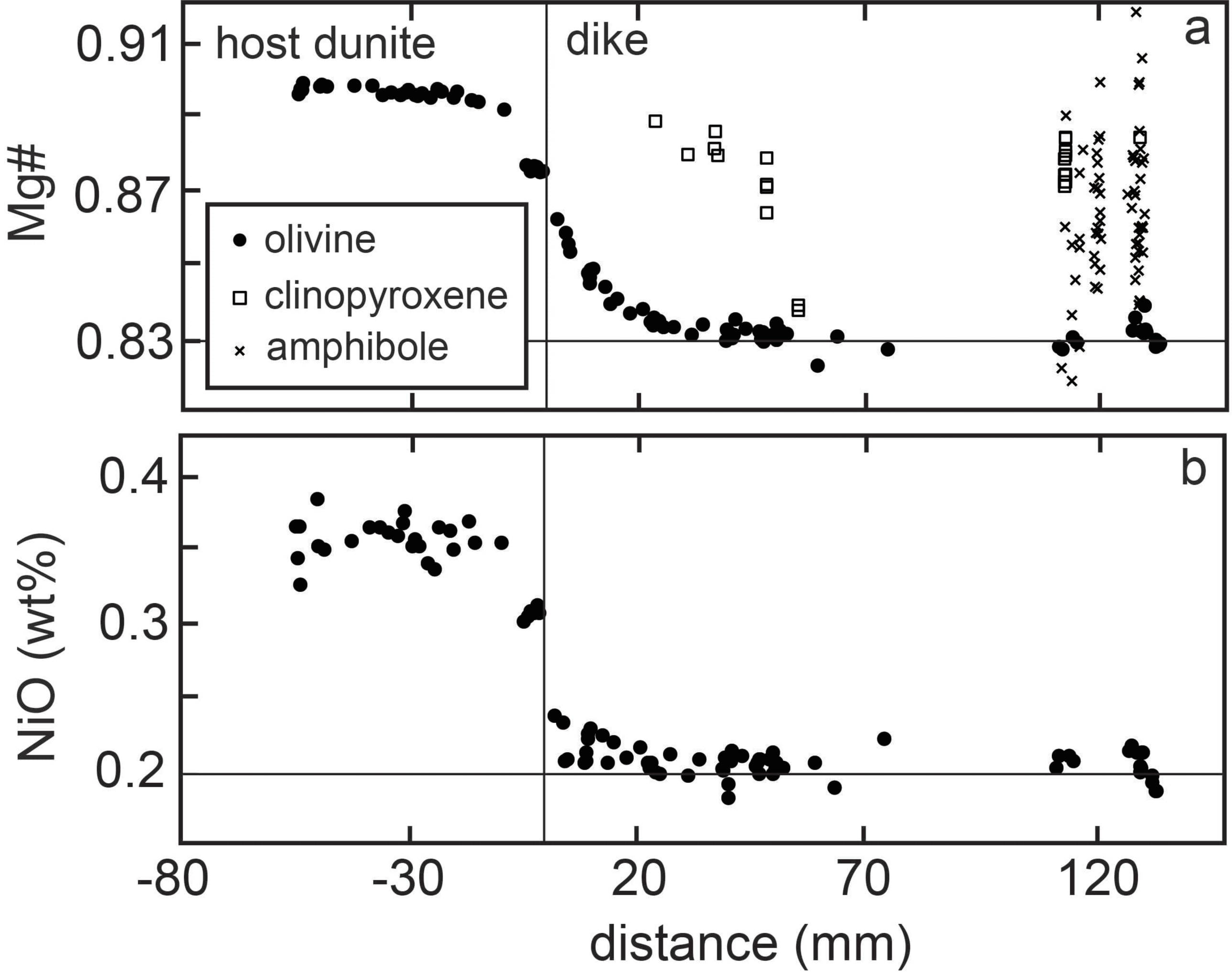
host dunite
dike
a
b
olivine
clinopyroxene
amphibole
Mg#
0.91
0.87
0.83
NiO (wt%)
0.4
0.3
0.2
-80
-30
20
70
120
distance (mm)

Fig. 7

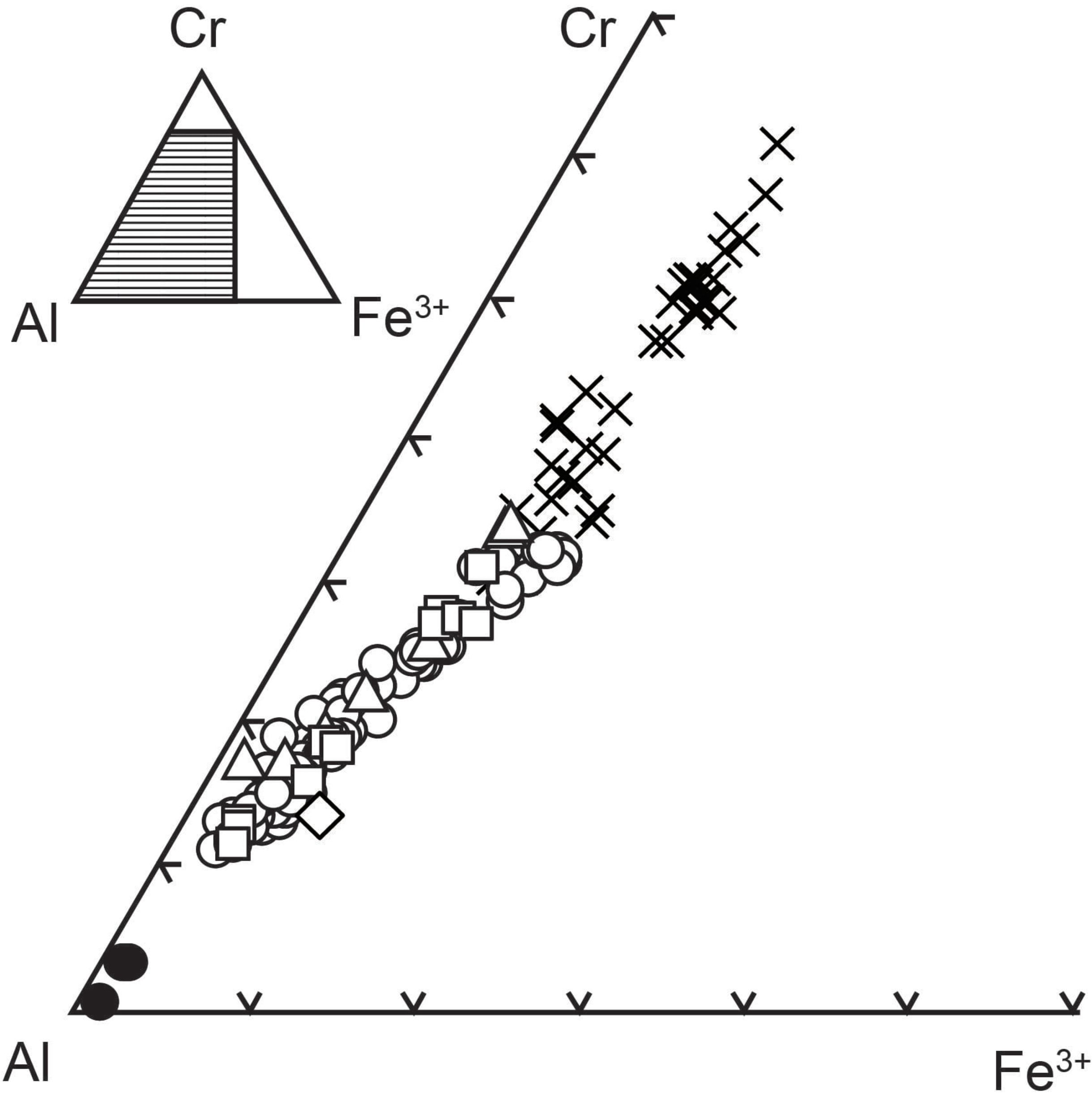

× spinel in the host

ultramafic dike

euhedral-subhedral spinel
inclueded in olivine/amphibole

△ DKSH1 □ RYO1
○ DKSH2 ◇ RYO2

anhedral spinel near plagioclase

● DKSH2

Fig.8

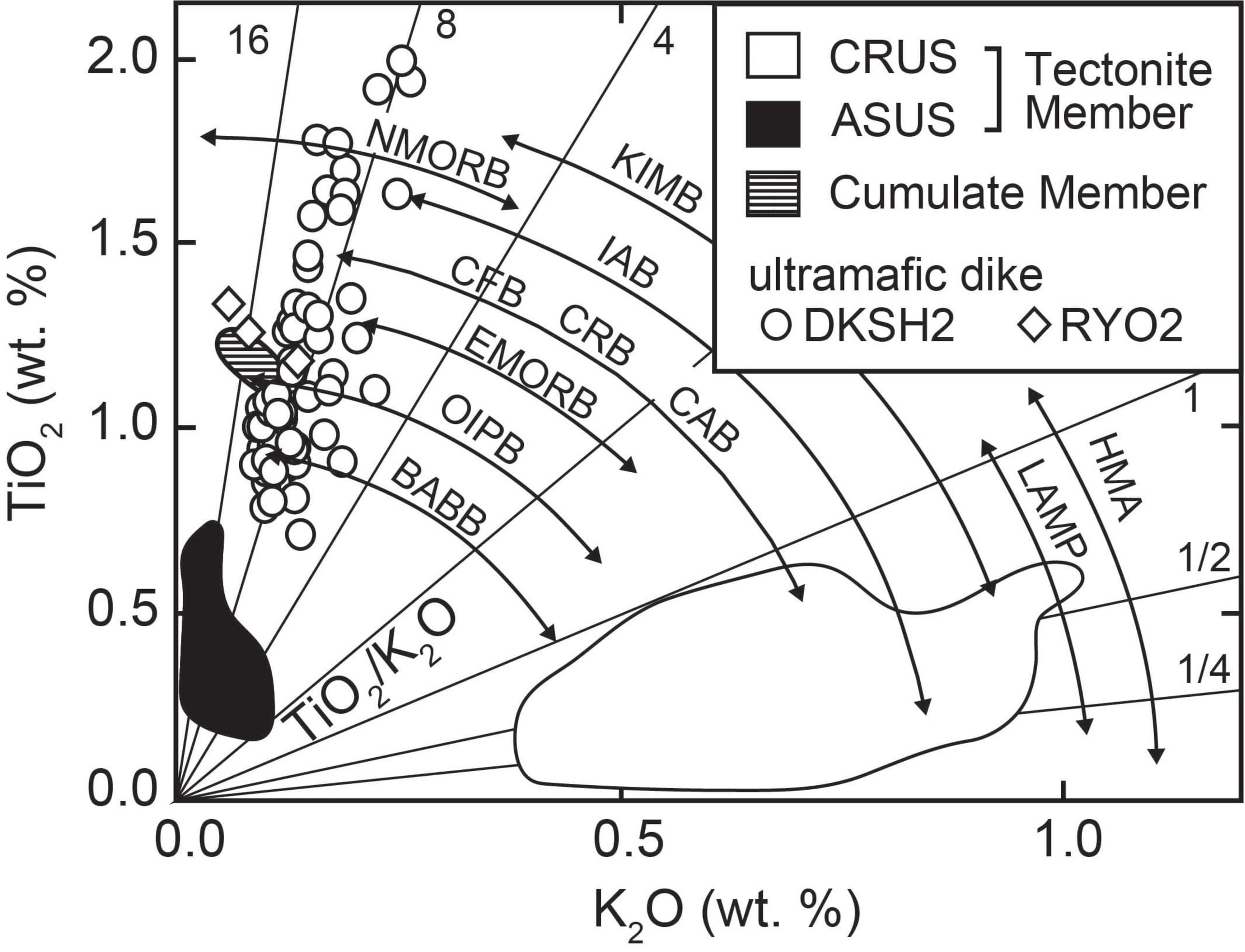
CRUS
ASUS
Tectonite Member
Cumulate Member
ultramafic dike
DKSH2
RYO2
NMORB
KIMB
IAB
CFB
CRB
EMORB
CAB
OIPB
BABB
TiO2/K2O
16
8
4
2
1
1/2
1/4
LAMP
HMA
2.0
1.5
1.0
0.5
0.0
TiO2 (wt. %)
0.0
0.5
1.0
K2O (wt. %)

Fig.9

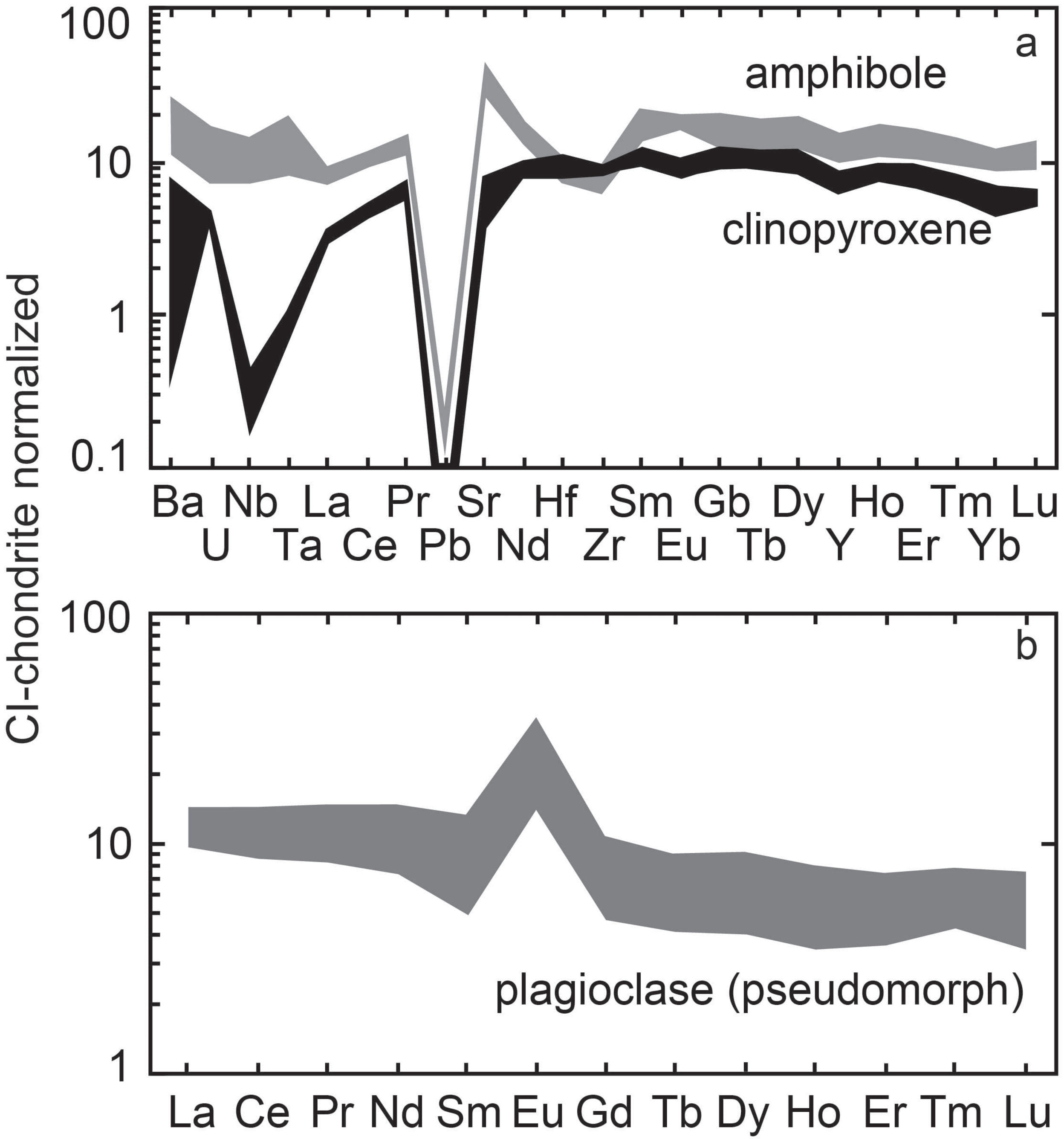
a
amphibole
clinopyroxene
100
10
1
0.1
Cl-chondrite normalized
Ba Nb La Pr Sr Hf Sm Gb Dy Ho Tm Lu
U Ta Ce Pb Nd Zr Eu Tb Y Er Yb
b
plagioclase (pseudomorph)
La Ce Pr Nd Sm Eu Gd Tb Dy Ho Er Tm Lu

Fig.10

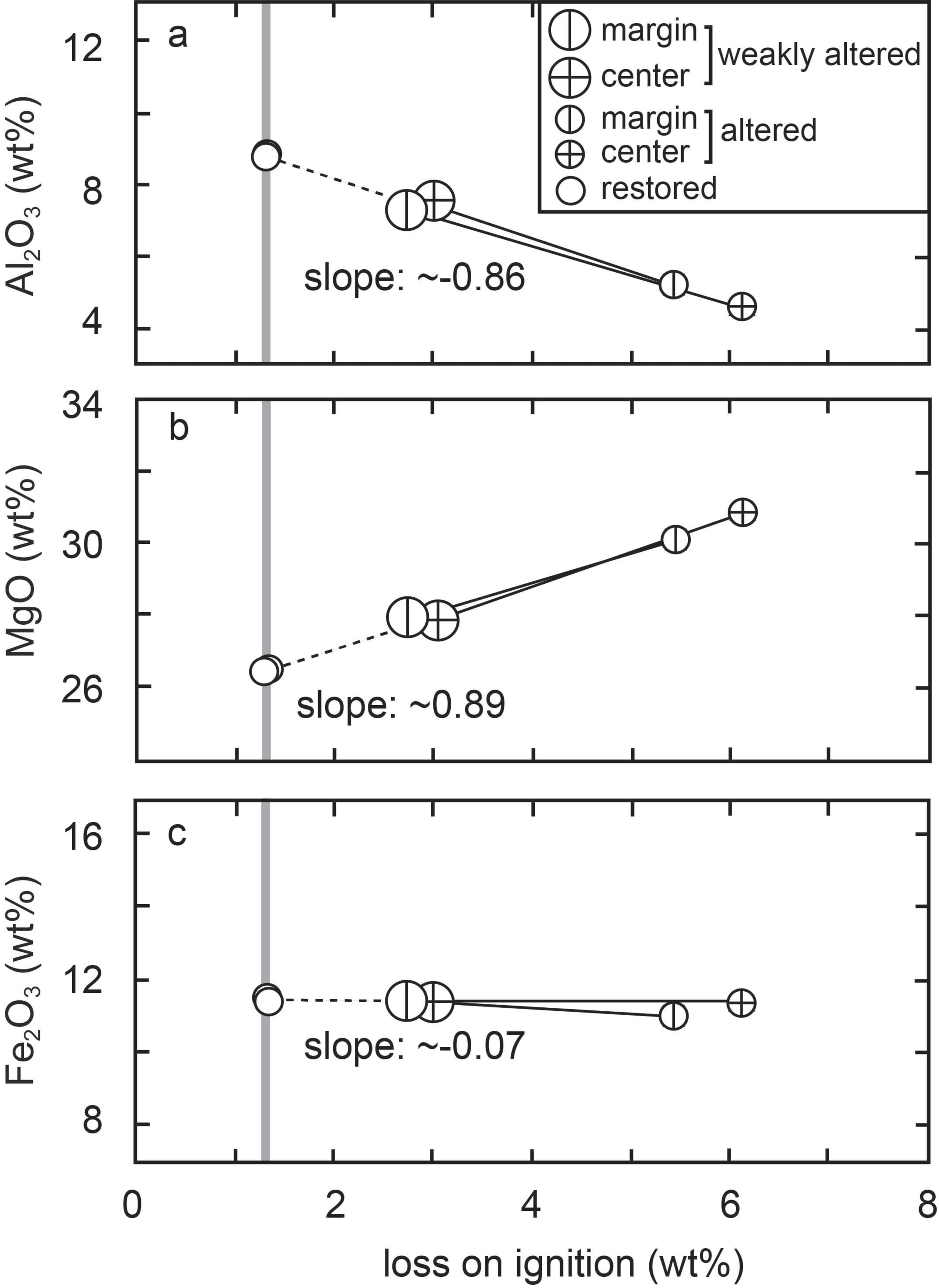
a
b
c
margin
center
weakly altered
margin
center
altered
restored
slope: ~-0.86
slope: ~0.89
slope: ~-0.07
Al2O3 (wt%)
MgO (wt%)
Fe2O3 (wt%)
loss on ignition (wt%)
12
8
4
34
30
26
16
12
8
0
2
4
6
8

Fig. 11

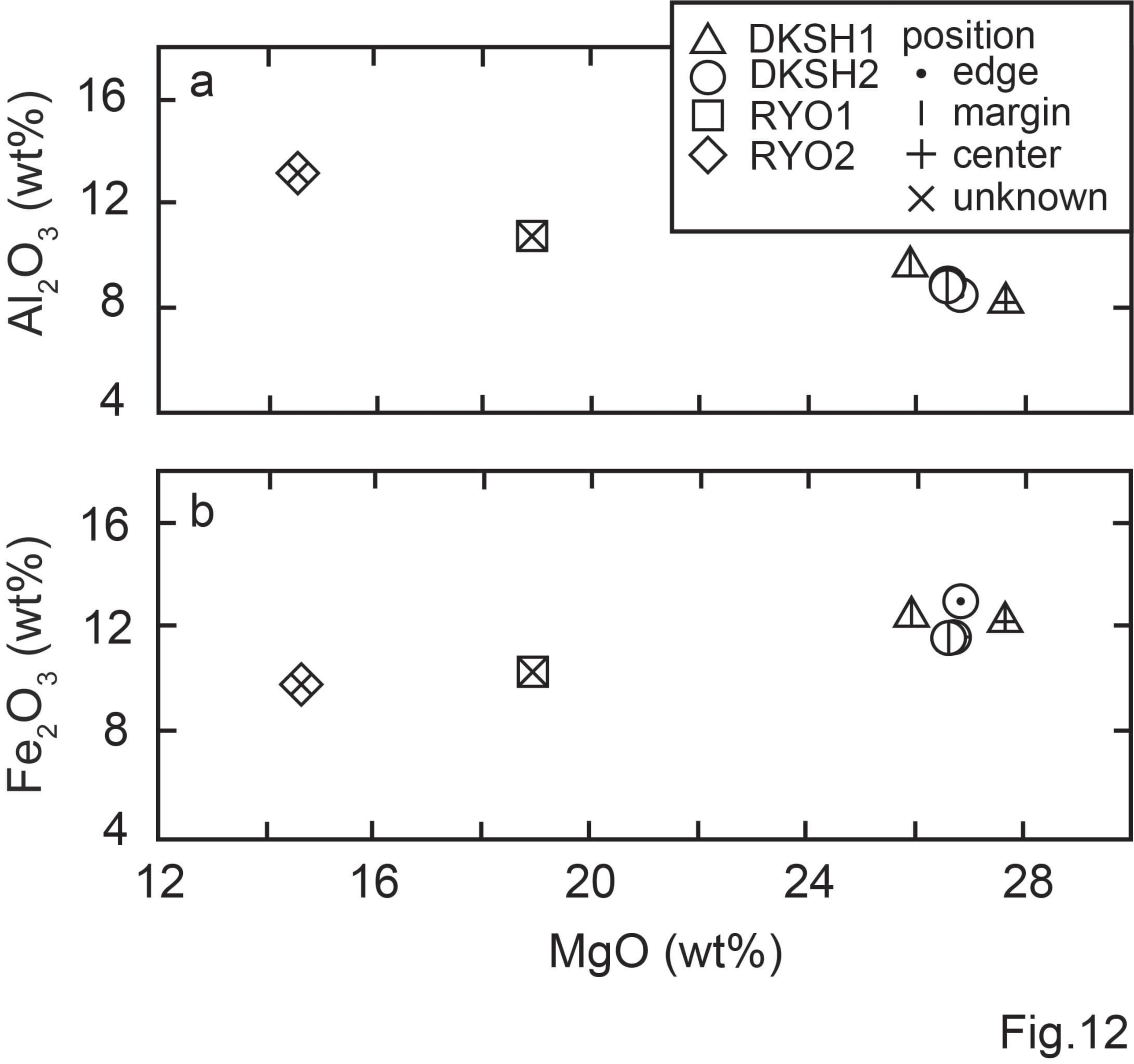
a
b
DKSH1
DKSH2
RYO1
RYO2
position
edge
margin
center
unknown
Al2O3 (wt%)
Fe2O3 (wt%)
MgO (wt%)
4
8
12
16
20
24
28

Fig.12

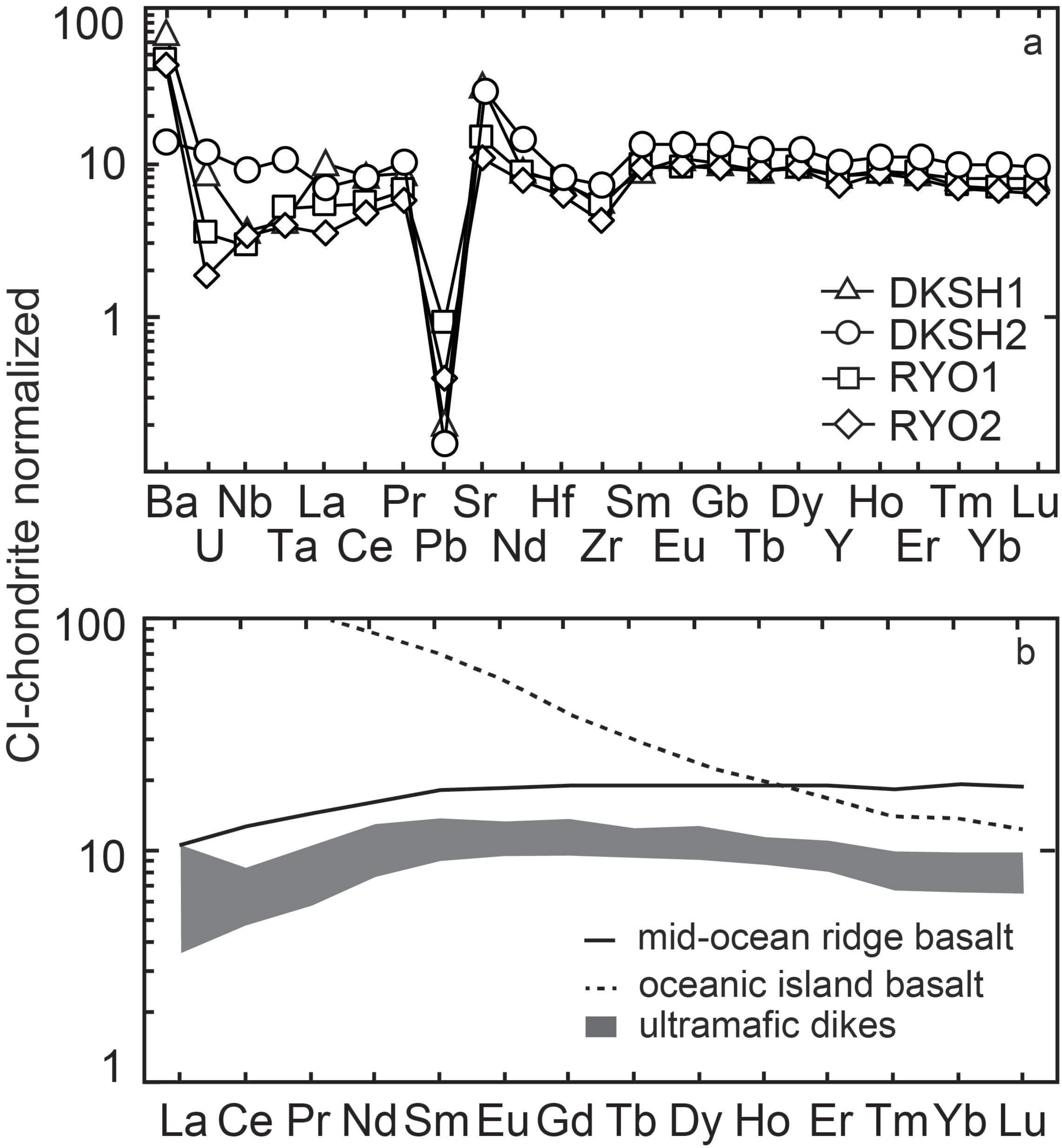
a
100
10
1
Cl-chondrite normalized
DKSH1
DKSH2
RYO1
RYO2
Ba Nb La Pr Sr Hf Sm Gb Dy Ho Tm Lu
U Ta Ce Pb Nd Zr Eu Tb Y Er Yb
b
100
10
1
mid-ocean ridge basalt
oceanic island basalt
ultramafic dikes
La Ce Pr Nd Sm Eu Gd Tb Dy Ho Er Tm Yb Lu

Fig.13

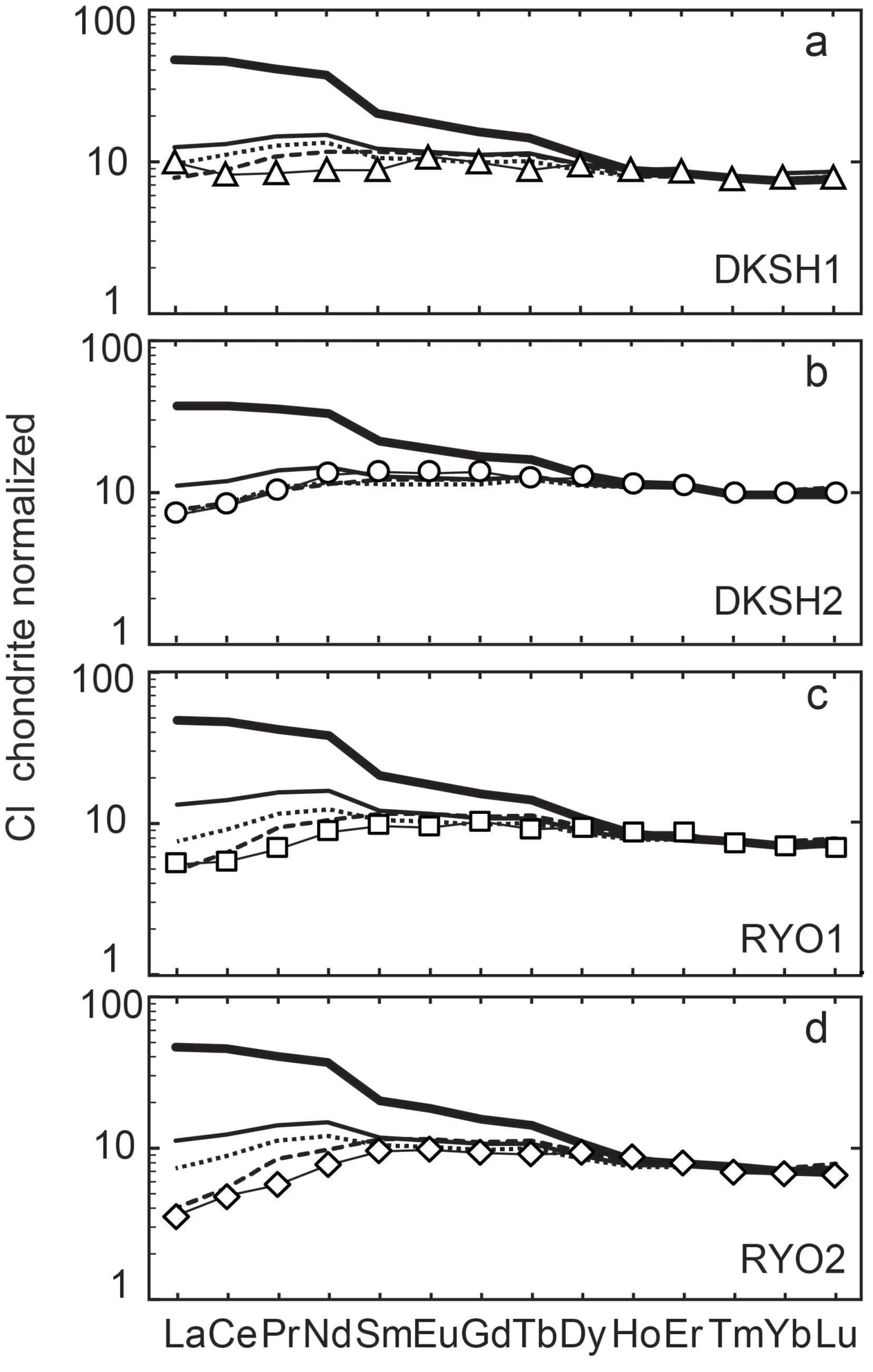
100
10
1
a
DKSH1
b
DKSH2
c
RYO1
d
RYO2
Cl chondrite normalized
LaCePrNdSmEuGdTbDyHoErTmYbLu
accumulated melt
primitive mantle
MORB mantle source
Depleted MORB mantle source
instantaneous melt
MORB mantle source

Fig.14

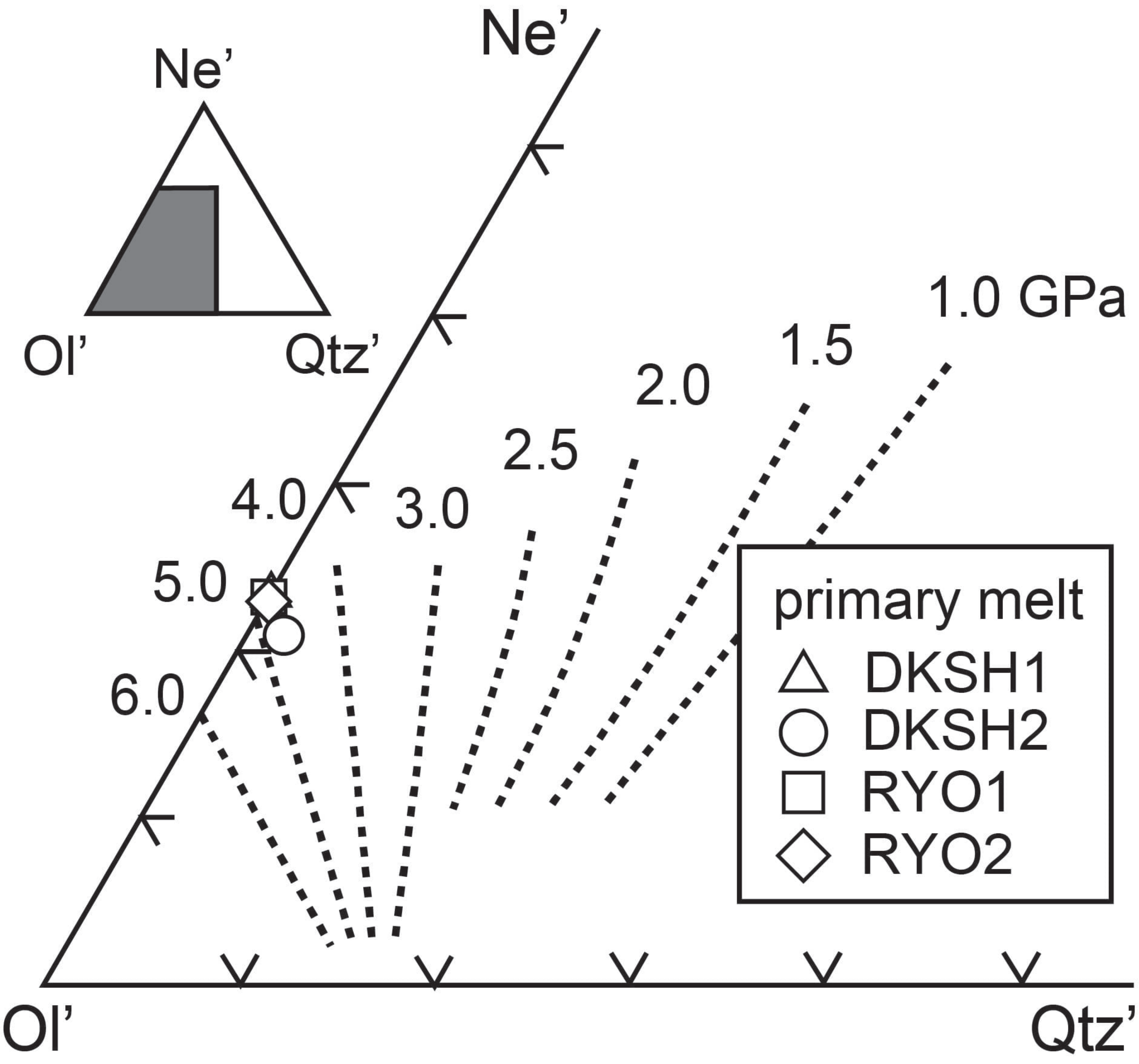
Ne'
Ne'
Ol'
Qtz'
1.0 GPa
1.5
2.0
2.5
3.0
4.0
5.0
6.0
primary melt
DKSH1
DKSH2
RYO1
RYO2
Ol'
Qtz'

Fig.15

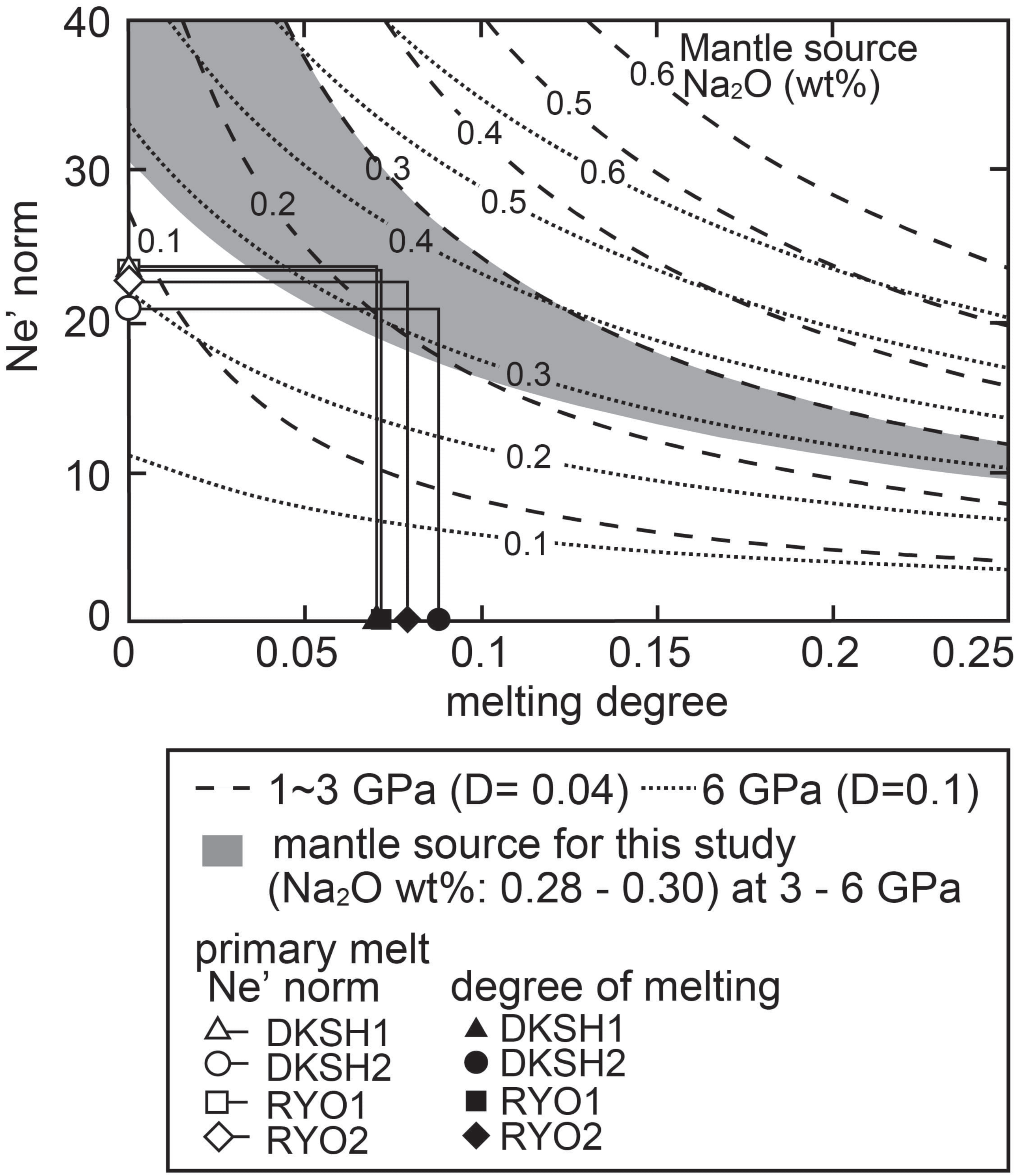
Mantle source
Na_2O (wt%)
0.6
0.5
0.4
0.3
0.2
0.1
Ne' norm
melting degree
0
10
20
30
40
0
0.05
0.1
0.15
0.2
0.25
1~3 GPa (D= 0.04)
6 GPa (D=0.1)
mantle source for this study
(Na_2O wt%: 0.28 - 0.30) at 3 - 6 GPa
primary melt
Ne' norm
degree of melting
DKSH1
DKSH2
RYO1
RYO2
DKSH1
DKSH2
RYO1
RYO2

Fig.16

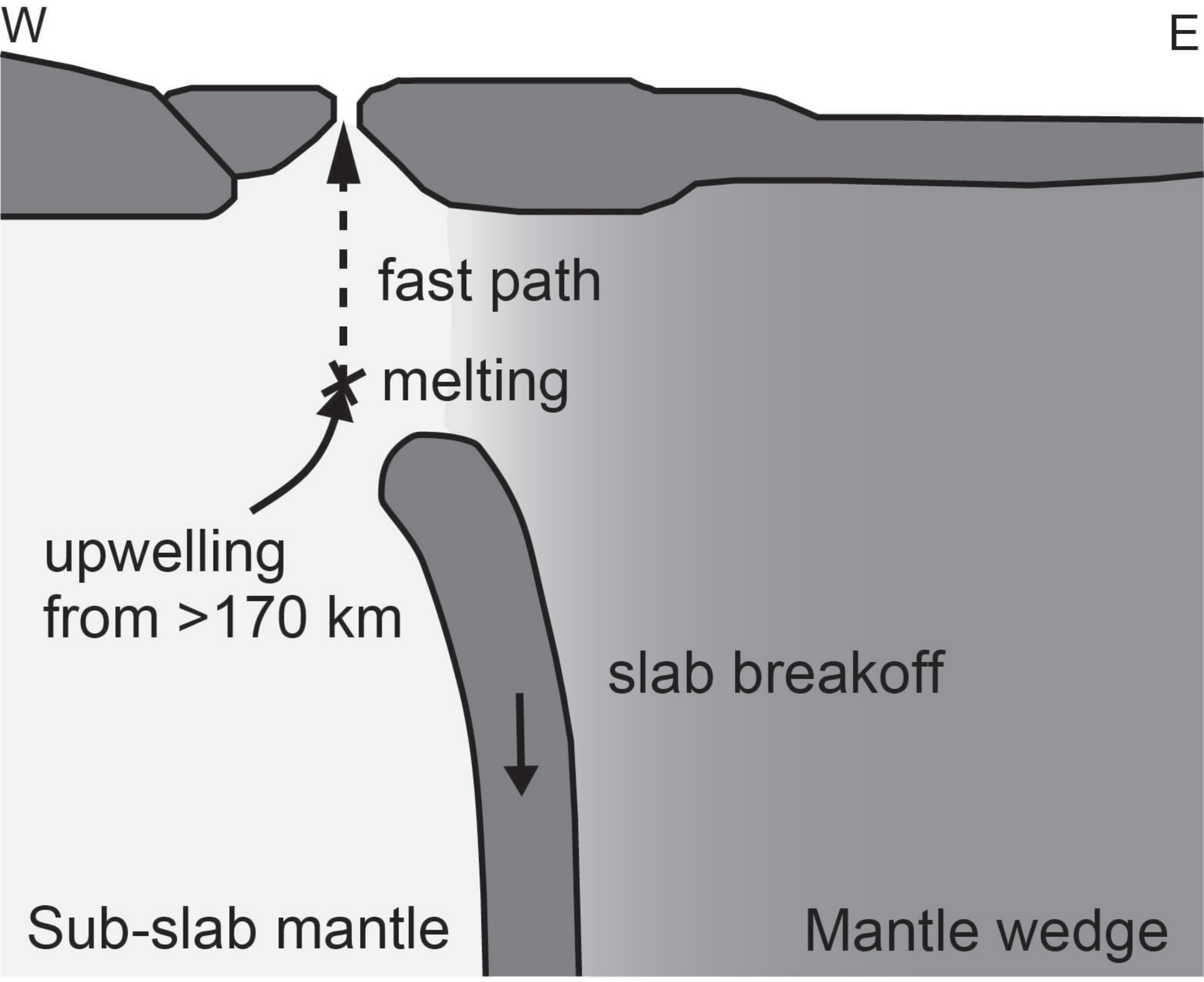
W
E
fast path
melting
upwelling
from >170 km
slab breakoff
Sub-slab mantle
Mantle wedge

Fig.17

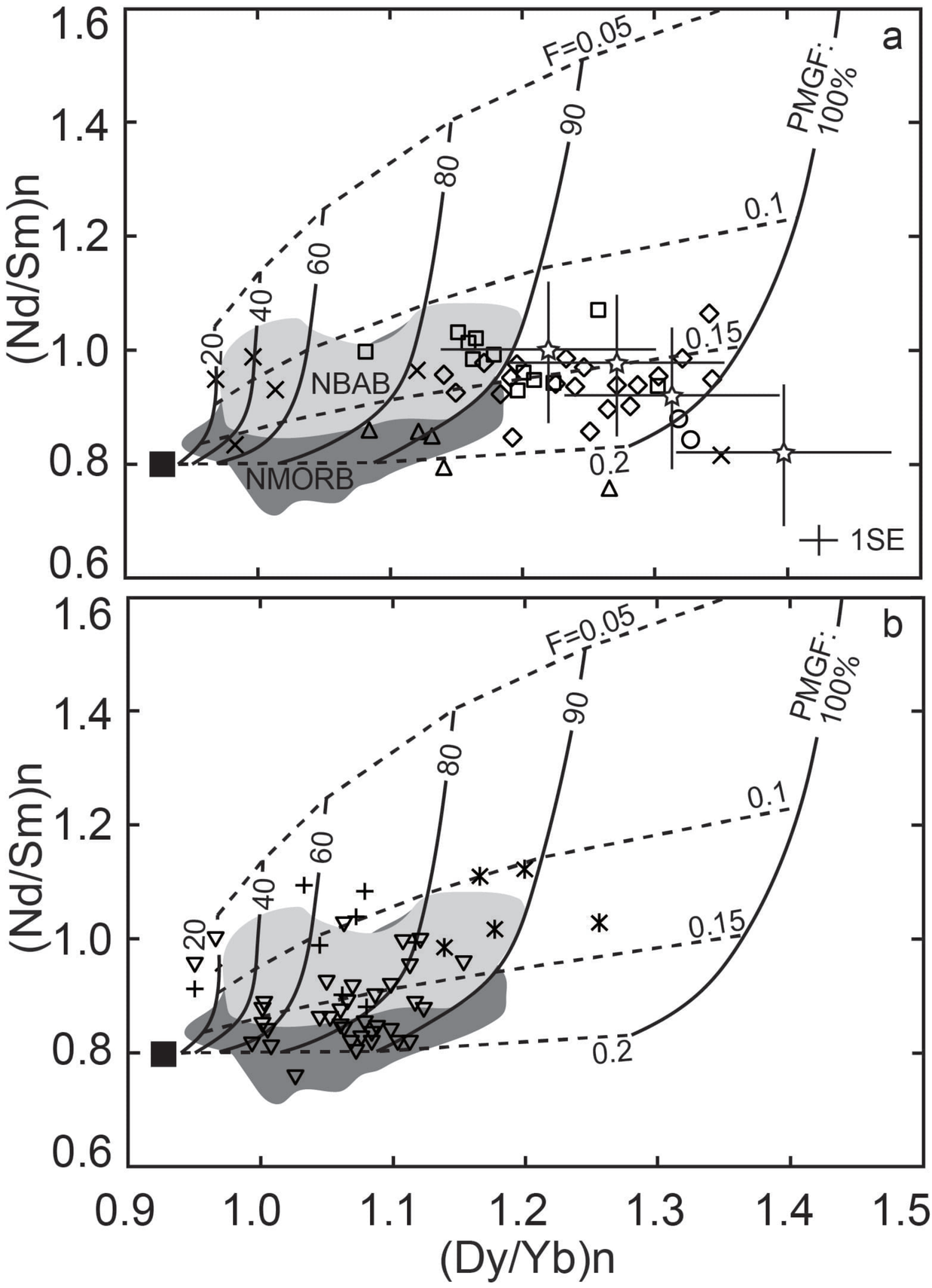

Cambrian-Ordovician arc ophiolites

- ☆ Hayachine-Miyamori (Japan)
- ○ Bymarka (Norway)
- ◇ Solund-Stavfjord (Norway)
- × Kudi (China)
- □ Cabo Ortegal (Spain)
- △ Star Lake (Canada)
- ✳ Bay of Islands (Canada)
- ▽ Annieopsquotch (Canada)
- \+ Jiugequan (China)
- ■ MORB mantle source

Fig.18